12-1-1988

One Dimensional Quantum Transport: Characterization and Device Applications

Roger K. Lake
Purdue University

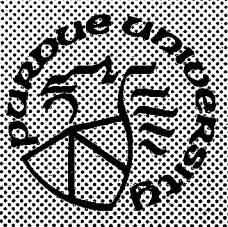

One Dimensional Quantum Transport: Characterization and Device Applications

Roger K. Lake

TR-EE 88-51
December 1988

School of Electrical Engineering
Purdue University
West Lafayette, Indiana 47907

Supported by the Office of Naval Research through Grant No. N00014-87-K-0693

PREFACE

This document is a Master's Thesis resulting from research sponsored by the Office of Naval Research.

ACKNOWLEDGMENTS

I thank my major professor, Mark Lundstrom, and Professor Michael Melloch for offering me the opportunity to work on this interesting project, and I particularly thank Professor Lundstrom for directing this thesis. I thank Professor Supriyo Datta for providing the seminal ideas which inspired this research. I owe much to Michael Young; without his expertise and untiring efforts, there would be no electron beam direct write capability at Purdue. Dr. Gary Bernstein shared much of his knowledge of electron beam lithography with me during visits and phone conversations, but I am especially thankful for his crucial advice to use SAL 601-ER7 which resulted in the solution of one of the three major processing problems. I thank Stewart Price and Shipley, Inc. for kindly donating the resist.

Both Biswajit Das and Dain Miller provided extensive help with low temperature testing, while Professor Ron Reifenberger provided the laboratory facilities. I also thank Dain for sharing a large library of data-crunching software and Michael McLennan for his Mondane software package which was heavily used for manipulating and graphing data. Finally, I thank Phil Neudeck and Qi-de Qian for their initial help with processing and generally helping me find my way around the labs.

The financial support of the Office of Naval Research through Grant No. N00014-87-K-0693 is also acknowledged.

TABLE OF CONTENTS

Page

LIST OF TABLES vii

LIST OF FIGURES viii

ABSTRACT xi

CHAPTER I - INTRODUCTION 1

1.1 Quantum Mechanical Electron Transport 1
1.2 Quantum Device Concepts 3
1.3 Research Objectives 6
1.4 Thesis Organization 6

CHAPTER II - QUANTUM DEVICES AND PHENOMENA 8

2.1 Ballistic Quantum Interference Effect: An Electron Interferometer 8
2.2 Programmable Quantum Resistor Network 14
2.3 Introduction to Quantum Phenomena in the Diffusive Regime 17
2.4 The Diffusive Aharonov Bohm Effect 20
2.5 Localization 22
2.6 Boundary Scattering 26
2.7 Electron - Electron Interaction 28
2.8 Universal Conductance Fluctuations 30
2.9 Shubnikov-deHaas Oscillations 32
2.10 Summary 34

CHAPTER III - ELECTRON BEAM LITHOGRAPHY 36

3.1 Electron Beam Lithography: An Introduction 36
3.2 Electron Optics 36

Page

3.3 Resolution 38
3.4 Primary Electrons 40
3.5 Secondary Electrons 42
3.6 Backscattered Electrons 43
3.7 Beam Size and Shape 45
3.8 Pattern Geometry and Proximity Effect 47
3.9 Electron Beam Resist 47
3.10 Multi-level Resist 51
3.11 Summary 51

CHAPTER IV - FABRICATION 53

4.1 Introduction 53
4.2 Fabrication Overview 53
4.3 Mask Layout 54
4.4 Film 59
4.5 Level 1: Ohmic Contacts and Electron Beam Alignment Marks 59
4.6 Level 2: Mesa Level 61
4.7 Post Exposure Bake 65
4.8 Development 65
4.9 Isolation Etch 65
4.10 Level 3: Schottky Gates 66
4.11 Other Fabrication Methods of Submicron Conducting Channels 67

CHAPTER V - CHARACTERIZATION OF DEVICE AND MATERIAL PARAMETERS 71

5.1 Introduction 71
5.2 Two Dimensional Mobility and Sheet Carrier Concentration 71
5.3 Magneto Resistance Anamoly 73
5.4 One Dimensional Structures 77
5.5 Estimation of Phase Breaking Length, L_ϕ 81
5.6 A Comment on the Low Frequency Component of the Fourier Power Spectrum 88

CHAPTER VI - NOVEL QUANTUM DEVICES 89

6.1 Gated Ring Structures 89

Page

6.2 Quantum Resonators....89
6.3 Summary....94

CHAPTER VII - CONCLUSION AND FUTURE WORK....95

7.1 Summary....95
7.2 Directions for Future Work....96

REFERENCES....97

APPENDICES

Appendix A....102
Appendix B....106
Appendix C....109
Appendix D....111

LIST OF TABLES

Table Page

2.1 Fermi wavelengths for widths containing 1 to 5 full transverse sub-bands. Numerical values are for $n_s = 2 \times 10^{11}$ cm^{-2} 18

3.1 Backscattered energy spread 43

4.1 Exposure doses at 20 KeV 64

5.1 Mobility and carrier concentration from classical Hall measurements. 71

5.2 Mobility and carrier concentration from Shubnikov-deHaas measurements 73

6.1 Fermi wavelengths corresponding to Fourier spectrum 94

LIST OF FIGURES

Figure Page

1.1 Plan view of laterally defined electron interferometer 4

1.2 Cross section of GaAs-$Al_{.3}Ga_{.7}As$ film for a horizontal quantum interference device. 5

1.3 Programmable resistor network....7

2.1 Schematic of electric and magnetic interferometer (after ref. 13)....9

2.2 Ballistic quantum interference device (after ref. 17) 12

2.5 Numerical simulations of a quantum resonator (after ref. 20). (a) Device simulated. (b) Single moded (c) Eight modes....19

2.6 Illustration of different quantum interference phenomena (after ref. 3). A) Aharanov-Bohm oscillations, B) Boundary scattering (large negative $\partial R_{xx}/\partial B$), C) Universal conductance fluctuations, D) Electron-electron interaction (monotonic term), E) Shubnikov-deHaas oscillations. 21

2.7 Energy levels at nonzero temperature from SdH effect. 33

3.1 Electron optics (after ref. 38)....37

3.2 Beam deflection (after ref. 38) a) Prelens deflection. b) Postlens deflection 39

3.3 Elastic scattering model (after ref. 52)....41

3.4 Monte Carlo simulations of primary, secondary, and backscattering electrons (after ref. 38 p. 64 and 53 p. 1392)....44

3.5 Square versus found beam (after ref. 58) 46

Figure Page

3.6 Proximity effect (after ref. 38) 48

3.7 Plots of normalized resist thickness versus log dose 50

4.1 Level 1: Ohmic contacts and alignment dots 55

4.2 Level 2: Mesa level 56

4.3 Submicron mesa level 57

4.4 Developed resist corresponding to submicron mesa level 58

4.5 Schottky gate level 60

4.6 Cross sections: A) Level 1 B) Level 2 C) Level 3. 62

4.7 Spin speed curve for SAL 601-ER7 (after ref. 61) 63

4.8 Al mask, A) Before boiling B) After boiling 68

4.9 SiO_2 mask, 0.3 μm linewidth 69

5.1 Hall bridge used for 2D measurements 72

5.2 Shubnikov-deHaas oscillations from 2D Hall bridge 74

5.3 Landau plot from 2D Hall bridge 75

5.4 Magneto-resistance anomaly 76

5.5 $R_{23,87}$: field reversed and field forward 78

5.6 R_{23}: field reversed and field forward. 79

5.7 R_{xx} versus magnetic field. (A) Negative magneto resistance, (B) Universal conductance fluctuations, (C) SdH 80

5.8 Aharanov Bohm oscillations with fitted polynomial 82

5.9 Aharanov Bohm oscillations with background removed 83

Figure Page

5.10 Fourier power transform of Aharanov Bohm oscillations 84

5.11 SEM micrograph of ring 85

5.12 Nominal ring dimensions 86

6.1 Quantum resonator device tested. Only submicron dimensions are drawn to scale. 90

6.2 Conductance versus gate voltage. T = 4.2K 91

6.3 Conductance fluctuations with background removed 92

6.4 Fourier power spectrum of conductance fluctuations 93

Appendix
Figure

C1 Coordinate systems: (a) Graphics (b) SPD (c) QSYS 110

ABSTRACT

Lake, Roger K. MSEE., Purdue University. December 1988. One Dimensional Quantum Transport: Characterization and Device Applications. Major Professor: Mark S. Lundstrom.

With the maturing of the technologies of molecular beam epitaxy and electron beam direct write, semiconductor crystals can be engineered on the size scale of a de Broglie wavelength in both the vertical and lateral directions. On this scale, the wave nature of the electrons becomes manifest and it becomes possible to conceive of devices that exploit wave properties such as resonance and diffraction. In this work, a complete fabrication process for building sub-micron conducting channels analogous to a waveguide in a high mobility GaAs - AlGaAs heterostructure is developed. The waveguides are characterized with respect to the number of transverse modes and the phase coherence length. A novel device structure analogous to a microwave resonator is fabricated and tested and found to give results in good agreement with theory.

CHAPTER 1
INTRODUCTION

1.1 Quantum Mechanical Electron Transport

The technology of molecular beam epitaxy has matured over the last two decades to the point where semiconductor crystals are routinely engineered on the atomic scale in the vertical direction. The use of heterostructures to separate carriers from donors gives mobilities of up to 100 m^2/Vs at liquid He temperatures, two orders of magnitude larger than that of Silicon inversion layers. At such a mobility, the mean free path is $\sim$ 10 μm. During the same time, the technologies of electron beam and X-ray lithography have developed so that it is possible to engineer semiconductor structures in the lateral direction on a nanometer scale. The combination of the two technologies permits the fabrication of devices in which the wave nature of electrons becomes manifest. Devices and phenomena which can only be explained using the formalism of quantum mechanics are termed quantum devices or quantum phenomena respectively. The well known example is the resonant tunneling diode in which electrons move in the vertical direction through an engineered lattice potential which acts in a manner analogous to a Fabrey-Perot cavity for electrons [72]. Well known examples of quantum phenomena are the Aharanov-Bohm effect, weak localization, universal conductance fluctuations, and Shubnikov-deHass oscillations. The objective of this work is to build structures and devices which exhibit and exploit the wave nature of electrons.

With the ability to engineer potentials both vertically and laterally on the size scale of a deBroglie wavelength, one can consider the possibility of building an electron analogue of a microwave network. However, there is a fundamental difference between electrons and photons. Infinitely many photons can occupy the same quantum state giving rise to a single frequency beam necessary for waveguide applications. In contrast, electrons are spin 1/2 matter particles which obey the Pauli exclusion principle. Disregarding spin degeneracy, no two electrons can occupy the same quantum state. This gives rise to a spread in energies which is equivalent to a spread in frequency. This

problem can be circumvented by testing for electron wave phenomena at very cold, liquid helium, temperatures. Then, only electrons within K_BT of the Fermi sphere contribute to the current.

A second difference is the difficulty in achieving a collimated beam. Quantization in the vertical direction by molecular beam epitaxy is a well established, reliable procedure. It is easy to engineer a heterostructure with a potential in the vertical direction which will confine the vertical wave vector to a single mode. The confining boundary can be made atomically smooth, giving exceptionally long mean free paths in the two dimensional electron gas. Such a structure is shown in figure 2.3. However, it is very difficult to build a lateral potential which confines the transverse wave vector to a single mode. It has not yet been accomplished. The best that has been achieved is three to four modes in the transverse direction [1, 2]. The technology available for quantization in the horizontal direction is less suitable. High resolution lithography is used followed by a wet etch, reactive ion etch, ion beam etch, or ion beam assisted etch [3, 4, 5, 6, 7, 8, 9]. Also, split Schottky gates have been used in fundamental research to provide transverse confinement for a resistor [23], and there has been one ingenious use of a Schottky gate to define a ring structure [15]. In all processes, the confining boundary is not atomically smooth and in all reported data, the mobility and conductivity are decreased in one dimensional structures compared to their two dimensional value.

To achieve single modedness in the transverse direction, the conducting channels must be very narrow. For example, with a sheet carrier concentration of 2.0×10^{11} cm^{-2}, assuming a particle-in-a-box potential, the channel width would have to be less than 40 nm to obtain a single transverse mode. This size scale is well within the limits of current technology, however, a 4 nm deviation in the width is a 10% deviation in the width of the waveguide. Although gold lines of 10 nm width have been fabricated by electron beam lithography and lift-off, variations in the width cannot be controlled to within 10% accuracy. If even greater line width control is needed, more fundamental limitations may be reached. A variation of 1.0 % corresponds to 4 Å which is smaller than the cubic lattice constant of GaAs. On this scale, the metal may be deformed by the crystal potential.

On the positive side, the electrical linewidth is generally much smaller than the physical linewidth due to edge depletion. Thus a line with a physical width of 1/2 μm may have an electrical width of 100 nm. Such a line will have 4 to 5 transverse modes occupied.

A third difference between an optical waveguide and a semiconductor electron waveguide is the occurrence of scattering events in electron transport. There are two types of scattering, elastic and inelastic. If only elastic scattering occurs, electron wave interference phenomena such as universal conductance fluctuations and the Aharanov-Bohm effect can still be observed, although the magnitude of the fluctuations is greatly reduced. Inelastic scattering, however, destroys the phase coherence necessary for interference effects. The way to avoid scattering is to have the length of the device less than the elastic or inelastic scattering length. To maximize the scattering lengths, a high mobility low carrier concentration AlGaAs-GaAs heterostructure is used and electrical testing is performed at liquid He temperatures. At such temperatures, phonon scattering is suppressed and the mobility is increased by a factor of 100 from room temperature. The low carrier concentration reduces the rate of electron-electron scattering thus maximizing the inelastic scattering length. For a mobility of 60 m^2/Vs and a velocity of 10^7 cm/s, the elastic mean free path is $\sim$ 2.5 μm. The inelastic mean free path is longer, $\sim$ 10μm. It has been observed that when the conducting channel is made very narrow, the resistivity increases decreasing the scattering lengths [1, 3, 10, 11]. This is attributed to boundary scattering. For this reason, the rule-of-thumb followed in this work when designing quantum devices is to keep relevant length scales as short as possible. The technology developed here sets this limit at $\sim$ 1.0 μm.

1.2 Quantum Device Concepts

Two different quantum device concepts based on a waveguide analogue are experimentally investigated in this work. One is the equivalent of a Mach-Zehnder interferometer for electrons. The electron channels are defined horizontally in the two dimensional electron gas (2DEG) of a high mobility GaAs-AlGaAs heterostructure by electron beam lithography followed by a wet etch. For a plan view of the device and a cross section of the GaAs-AlGaAs heterostructure see Figs. 1.1 and 1.2. This implementation will be investigated in this work.

The other quantum device investigated is a gate controlled resistor whose operation is an analogue of a multiport microwave resonator (see Fig. 1.3 for an illustration). Referring to Fig. 1.3, the gate can be used to change the phase of the standing wave. The resistance seen between two probes will depend on whether the probes rest at a null or peak of the wave. The film and fabrication process are identical to the horizontal implementation of the

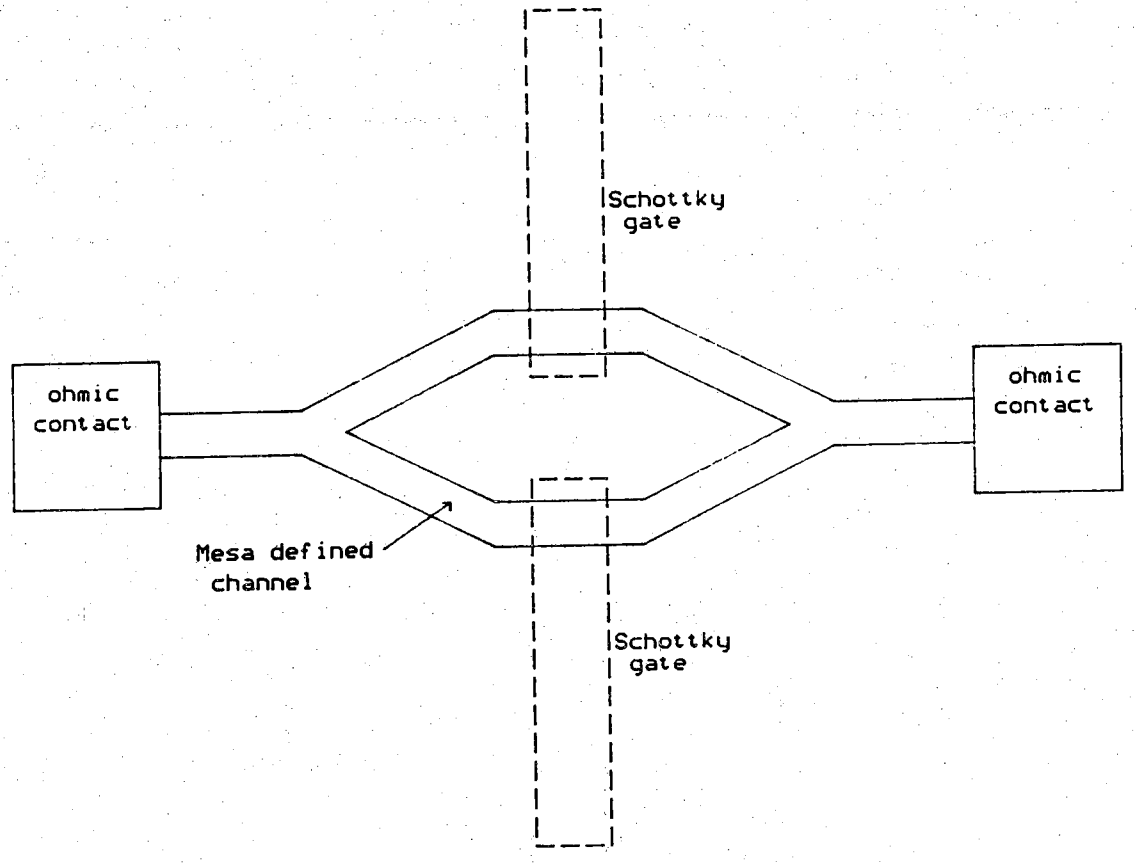

Figure 1.1 Plan view of laterally defined electron interferometer

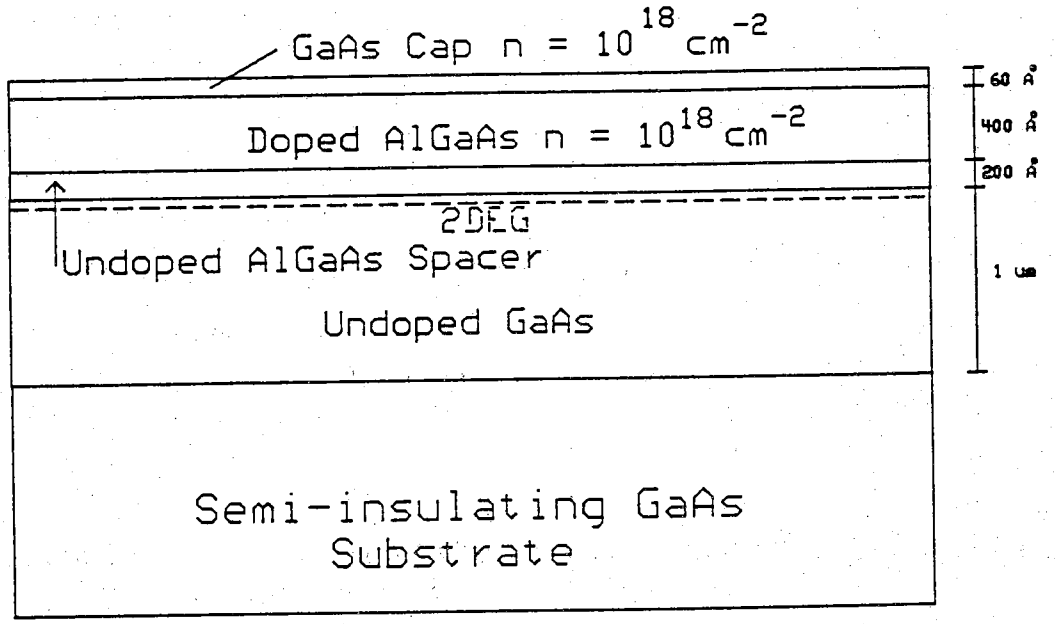

Figure 1.2 Cross section of GaAs-$Al_{.3}Ga_{.7}As$ film for a horizontal quantum interference device.

electron interferometer.

1.3 Research Objectives

The four objectives of this work are:

(1) Develop electron-beam direct write capability to define sub-micron features and provide level-to-level alignment with an error of less than 1/4 micron.

(2) Develop a complete fabrication process for building quantum devices.

(3) Develop test procedures to electrically characterize key device and material properties such as the electrical linewidth, the elastic and inelastic scattering lengths, the mobility and the sheet carrier concentration.

(4) Use the above acquired capabilities to physically realize and test novel quantum device concepts.

1.4 Thesis Organization

A more in-depth description of the novel devices introduced above is given in chapter 2. The second part of the chapter describes quantum phenomena useful for characterizing material and device parameters. Chapter 3 provides an introduction to electron beam lithography with an emphasis on explaining the parameters that affect resolution. A detailed description of the mask-layout and fabrication process used to build a gated quantum device is given in chapter 4. In chapter 5 the methods used and results obtained in characterizing key parameters of one-dimensional structures are reported. Chapter 6 describes the results obtained from testing a quantum resonator.

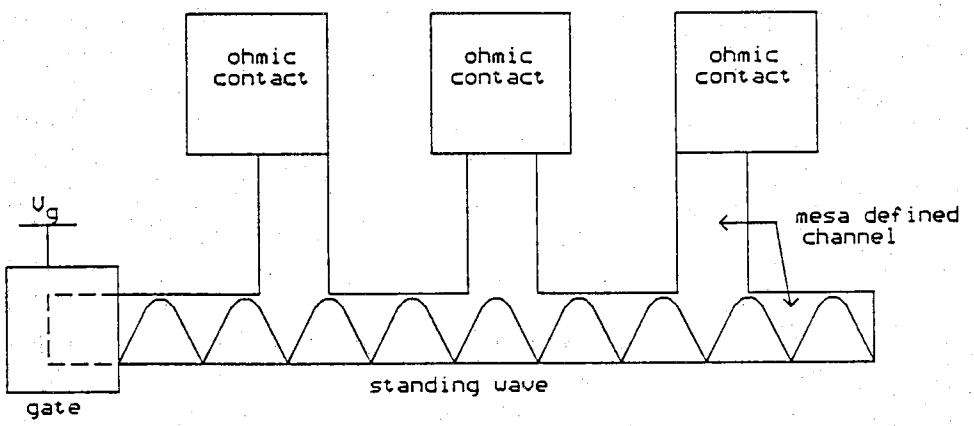

Figure 1.3 Programmable resistor network

CHAPTER II
QUANTUM DEVICES AND PHENOMENA

2.1 Ballistic Quantum Interference Effect: An Electron Interferometer

In the first section of this chapter, the operation of the two quantum devices described in the introduction are analyzed in some detail. In the second part of the chapter, six quantum phenomena which can be used to characterize key material and device parameters are described.

The first device proposed, historically, whose operation is based on a waveguide analogue is a quantum interference device [12]. Its operation is based on the phenomenon which, in the solid state literature, is referred to as the Aharonov-Bohm effect.

Consider the effect of an electric or magnetic field on an electron. If, without the presence of a field, the Hamiltonian is H_o and the solution is Ψ_o, then in the presence of an electric field the Hamiltonian becomes H_o - eV(t) and the solution becomes

$$\Psi = \Psi_o e^{i\frac{e}{\hbar}\int V(t)dt} .$$

In the presence of a static magnetic field the Hamiltonian becomes

$$\frac{1}{2m}(\vec{P} + e\vec{A})^2 + U_o$$

where U_o is the potential corresponding to H_o and the eigenstate becomes

$$\Psi = \Psi_o e^{-i\frac{e}{\hbar}\int \vec{A}\cdot d\vec{x}} .$$

The symbols V and $\vec{A}$ are the electric and magnetic potentials, e is the electron charge, and $\hbar$ is the reduced Planck's constant. Thus the field changes the phase of an electron. This effect can be used to build the electron equivalent of the Mach-Zehnder interferometer shown in Fig. 2.1.

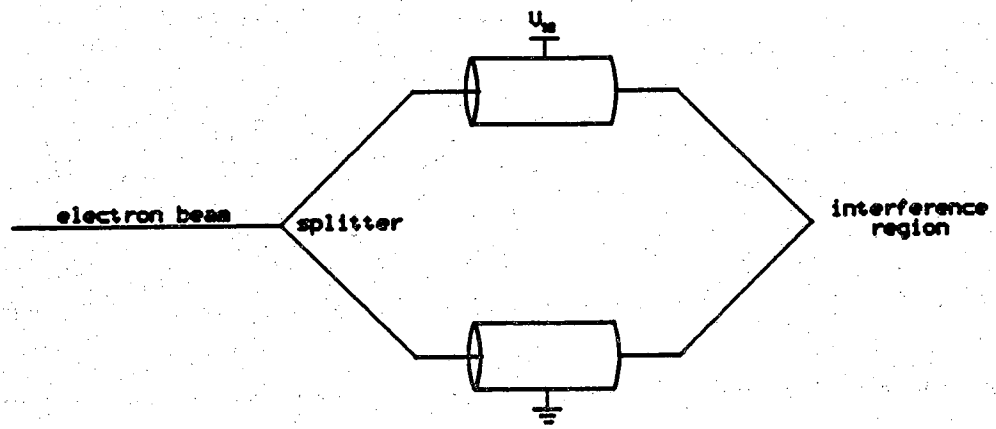

Electric Interference Effect

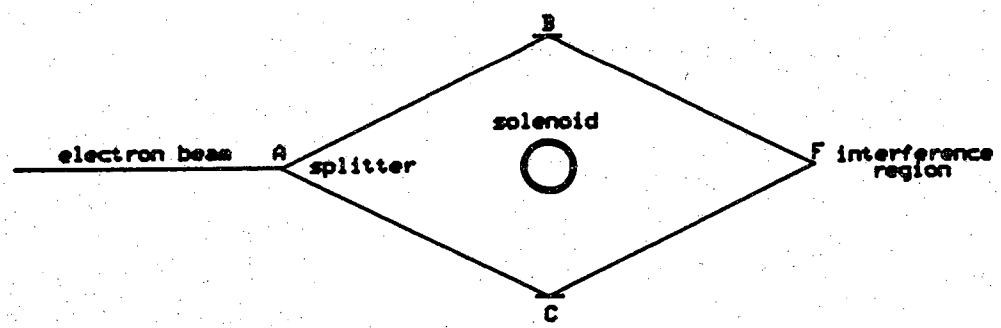

Magnetic Interference Effect

Figure 2.1 Schematic of electric and magnetic interferometer (after ref. 13)

For the electric case a monoenergetic, collimated beam is split into two paths each at a different potential. The electrons initially in phase at the splitter have their phases shifted by $\frac{e}{\hbar}Vt$ for constant V, where t is the transit time. The electrons are recombined and experience constructive or destructive interference depending on their phase difference, $\sim e/\hbar V_{12}<t>$, where V_{12} is the potential difference between the two arms and $<t> = (t_1+t_2)/2$. If V_{12} is ramped, the interference will be periodic in V_{12} with period $h/(e<t>)$.

For the magnetic effect, the phase difference, $\Delta\theta$, is

$$\Delta\theta = -\frac{e}{\hbar}\left\{\int_{ACF}\vec{A}\cdot d\vec{x} - \int_{ABF}\vec{A}\cdot d\vec{x}\right\}$$

which is identical to

$$\Delta\theta = -\frac{e}{\hbar}\oint\vec{A}\cdot d\vec{x}$$

which by Stoke's Theorem gives

$$\Delta\theta = -\frac{e}{\hbar}\int\int\vec{B}\cdot d\vec{s}$$

Thus

$$\Delta\theta = -\frac{e}{\hbar}\Phi$$

where Φ is the magnetic flux enclosed by the arms. If the magnetic field is slowly ramped, the interference will be periodic in B, with period $\frac{h}{eA}$ where A is the area enclosed.

Only the presence of the potential is actually necessary for the above effects since only the potential enters into the Hamiltonian. The fundamental nature of the potential in quantum mechanics as opposed to the field was first proposed by Aharonov and Bohm in [13]. Figure 2.1 illustrated the proposition with a thought experiment in which the electron beams were carefully shielded from any field while still experiencing a potential.

In metals and semiconductors, the term Aharonov-Bohm effect is used loosely to describe quantum interference phenomenon in electron transport through non-simply connected regions. In metals, the non-simply connected region is usually a ring of submicron dimensions. For a complete review of

work in metals see [14]. In semiconductors, the Aharonov-Bohm effect has only been seen in III-V heterostructures, generally with a high mobility two dimensional electron gas confined at a GaAs-AlGaAs interface [1,2,3,6,15,16]. Two types of non-simply connected regions have been investigated; ring structures defined laterally by dry or wet etching and vertical double channel structures where the channels are defined by molecular beam epitaxy (MBE) growth [12]. In solid state experiments, no attempt is made to shield the electrons from the magnetic or electric fields associated with the potentials; thus, the "looseness" of the term "Aharonov-Bohm effect."

What is of interest is the quantum interference phenomenon. To achieve large conduction modulation from electron interference, an electron interferometer must operate in the ballistic regime. The distance between the splitter and analyzer must be short, on the order of 1.0 μm at liquid helium temperatures. The device should be symmetric between the two channels. An illustration of an ideal implementation is shown in Fig. 2.2. For an ideal device that is single moded in both the y and z directions, the conductance oscillations can theoretically become very large, up to 100% for both the electrostatic and magnetic Aharonov-Bohm effect. For a complete review of both experiment and theory, see [17]. In this regime, two terminal conductance oscillations of 10% with amplitude $70e^2/h$ have been seen in the magnetic Aharonov- Bohm effect [17].

In reference 17, a schematic of the device shown in Fig. (2.2) is analyzed for the ballistic, electrostatic, Aharonov-Bohm effect. The device is assumed to be extended in the y direction with width W_y. Initially three assumptions are made: the transport is ballistic, the device is perfectly symmetric about $z = 0$, and only the lowest eigenstate in the z direction is occupied in both the arms and the leads. Under the above assumptions, the following results are obtained for the zero temperature limit. The conductance, G, is given by the two terminal, single channel conductance formula [14],

$$G = \frac{2e^2}{h} \sum_{k_y} |T(E_f,k_y)|^2 \tag{2.1}$$

where $T(E_f,k_y)$ is the transmission coefficient of wavevector k_y at the Fermi level. The transmission coefficient is shown to follow the proportionality,

$$|T|^2 \propto 1 + \cos\left\{2\pi \frac{2m^*}{\hbar (k_{x1} + k_{x2})} L \frac{e}{h} V_{12}\right\} \tag{2.2}$$

where L is the length of the arms, e is the electron charge, k_{xi} is the $\hat{x}$-directed

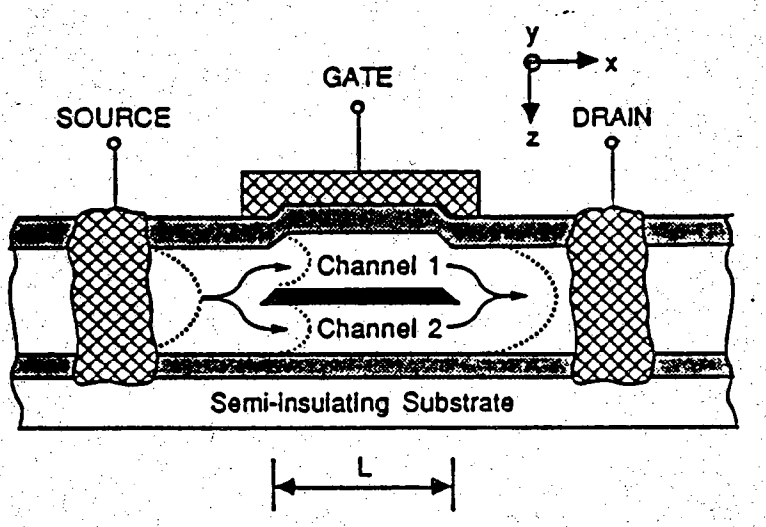

Figure 2.2 Ballistic quantum interference device (after ref. 17)

wavenumber in the ith channel at the Fermi level, and V_{12} is the difference in average potential in each arm. The periodicity in applied voltage is the same as for free electrons,

$$\tau = \frac{h}{e<t>}$$

where $<t>$ is the average transit time through the arms. The cutoff voltage difference difference, V_{12}, at the first half period is $\tau/2$. Assuming $v_x = 10^7$ cm/s and L=1μm, $V_{12} = 0.21$ mV. V_{12} is the potential difference between the arms at the GaAs - AlGaAs interface. To calculate the gate voltage, assume that all of the voltage is applied to one arm and use the approximation

$$\delta\Phi_{gate} = e^2 \frac{t}{\epsilon} \frac{m^*}{\pi\hbar^2} \delta\Phi_s \tag{2.3}$$

where Φ_s is the surface potential at the heterojunction, t is the thickness and ϵ is the dielectric constant of the GaAs cap and AlGaAs. Assuming that the thickness is 650 Å, $\epsilon = 13\epsilon_o$, and $m^* = 0.68m_e$, then $\delta\Phi_{gate} = 26\delta\Phi_s$. Therefore, the gate voltage necessary to achieve the first off state is $\sim$ 5.46 mV. In an ordinary FET, it is necessary to deplete carriers from the channel to switch from an on state to an off state. With a quantum interference device, it is only necessary to change the carrier's phase. Another interesting property is that by increasing the gate voltage further, the transconductance changes from negative to positive which raises the possibility of complementary logic.

There are a number of factors that can degrade the performance of the device. $|T|^2$ must be summed over all k_y; for each k_y, the transit time, $<t>$ will be different giving a different period, τ, which will reduce the overall change in conductance due to an applied field. Unless the device is single moded in both the y and z directions G cannot be reduced to zero. However, reducing the number of transverse modes reduces the overall conductance of the device. When multiple reflections are taken into account, resonances occur in plots of $|T|$ versus k_y due to the Fabrey-Perot effect. The transit time must be multiplied by some integer for each multiply reflected path giving a different period. Also, the probability of a scattering event is increased. If the device is multimoded in the z direction, then the sum in (2.1) must be over k_y and all pairs of k_z. The discussion of the effect of summing over k_y also applies to k_z. Furthermore, the proportionality in (2.2) switches

back and forth from $(1+\cos\theta)$ to $(1-\cos\theta)$ for even and odd pairs of k_z subbands respectively. The amplitude of conductance modulation decreases quickly as the number of k_z modes increases. Fluctuations in width, W, act as a built in potential offsetting the θ=0 point. If the fluctuations are large enough, boundary scattering will occur and one will be back in the diffusive regime. Recent calculations show that just a few scattering events greatly reduce the conductance modulation [18]. Thermal smearing of the Fermi level will also increase the spread in transit times and therefore reduce the magnitude of the modulation.

To fabricate a device in which electron transport is in the ballistic regime and conductance modulation is achieved by modulating the electrons' phase is a non-trivial task. Two types of implementation are possible, vertical and horizontal. In the vertical structure, the conducting channels are defined by MBE. The structure shown in Fig. 2.2. seems an ideal structure. The width, W, determined by MBE growth can easily be made such that k_z is single moded. However, the fabrication requires interrupted growth, processing, and re-growth. The quality of the re-growth crystal is poor and surface states are created along the top of the barrier and in the middle of the leads on the order of $10^{11} - 10^{12}$ cm^{-2}. The states can be filled by delta doping, but then one has ionized impurities in the channel reducing the mobility.

The horizontal structure is built on a high mobility low carrier concentration MODFET type film, (see Fig. 1.2). Fabrication requires high resolution electron beam lithography. It is single moded in k_y and generally has 3 - 5 modes in k_z. Thus one can only expect a small percent modulation in conduction. The maximum percent modulation observed to date in high mobility ring structures is $\sim$ 10% at 150mK [1]. The device is defined by electron beam lithography and etching, either wet or dry. The electrical line width is less than the physical line width due to depletion from the sides. The boundaries are not atomically smooth, and in devices with width less than 1000 Å, boundary scattering becomes large. Thus, one may need to compromise between multimodedness and mobility.

2.2 Programmable Quantum Resistor Network

A second proposed device, is a programmable resistor, or more generally, resistor network [19]. The device is the analogue of a multiport microwave network and will be referred to as a quantum resonator. The resistance between any two ports is affected by the load on a third port. Thus, a gate at

the end of a electron transmission line stub can be used to adjust the load between any two taps on the line, (see Fig. 1.3). This structure can be built on the film shown in Fig. 1.3. The heterojunction automatically provides a wavefunction that is single - moded in the z direction. Transverse confinement should be as narrow as possible to keep the number of filled transverse bands to a minimum. Multiple transverse modes will reduce the modulation effect. All ports must lie within an elastic scattering length of each other for large effects although if the ports are within a phase breaking length (explained in the next section) of each other a small conductance modulation can still be expected, on the order of e^2/h.

There are two possible modes of operation of the quantum resonator. In the first mode, the carriers are not depleted under the gate. An applied potential changes the carrier concentration and thus the wave vector under the gate. This is similar to changing the impedance at the end of a transmission line. One can make a rough calculation of the change in potential at the 2DEG necessary to change the phase of the wave function under the gate by a factor of π. This corresponds to changing the resistance between two nodes from a maximum to a minimum or vice-versa. The energy of the electron can be written as

$$E = \frac{\hbar^2 k^2}{2m^*} + V_s$$

where V_s is the potential at the 2DEG. Taking differentials while enforcing energy conservation gives

$$0 = \frac{\hbar^2 k}{m^*}\delta k + \delta V_s$$

or disregarding the minus sign,

$$\delta V_s = \frac{\hbar^2 k}{m^*}\delta k \tag{2.4}$$

Denoting the length of the mesa under the gate as L and assuming a wave function of the form sin(kx) under the gate, then a phase change of π occurs when $\delta kL = \pi$ or when $\delta k = \pi/L$. Substituting this into (2.4) gives

$$\delta V_s = \frac{\hbar^2 k}{m^*}\frac{\pi}{L}$$

Using the two dimensional density of states to relate k to n_s gives

$$\delta V_s = \frac{\pi \hbar^2 \sqrt{2\pi n_s}}{m^* L}$$

For $L = 1/2\ \mu m$ and $n_s = 2 \times 10^{11}\ cm^{-2}$, $\delta V_s = 0.79$ meV. Relating the gate potential to the interface potential by (2.3) gives $\delta \Phi_{gate} = 20.8$ mV. If one slowly ramps the voltage, one would expect to see oscillations in conductance with some degree of periodicity with the period found as above.

The other mode of operation occurs after the channel under the gate is depleted of electrons and the depletion region begins to move into the channel with the effect of physically moving the channel boundary. In this regime, the channel length is a function of gate voltage. To analyze this regime, a slightly more simplified device will be used than shown in Fig. 1.3. The simplification is that the end of the channel opposite the gate is open to a large two dimensional reservoir. By increasing the gate voltage, the boundary at the gate end of the channel pushes the standing wave to the right. As the peaks and troughs of the wave move past the probes, the conductance will oscillate. To predict the period of the oscillation, the relationship between gate voltage and depletion width must be known and the electron wavelength is needed.

There are two difficulties in predicting the relationship of the depletion width to the gate voltage. The lateral depletion width is the result of fringing fields. Thus the problem is two dimensional. Secondly, the heterostructure is grown on a semi-insulating substrate so the boundary conditions are not well defined. What is done in practice is to observe at what gate voltage the resistance at the probe nearest the gate begins to dramatically increase. At this voltage, V_t, it is assumed that the depletion region has reached the probe. Then, assuming the depletion width moves linearly with gate voltage, the relationship between gate voltage and depletion width is $W = Vd/V_t$ where d is the gate probe spacing.

To calculate the Fermi wavelength, the two dimensional density of states provides an excellent first approximation. The two dimensional Fermi wavelength is within 8%, 5.5 nm, of the Fermi wavelengths of the first and second subbands of any channel with three of more filled bands. In two dimensions, $k_f = \sqrt{2\pi n_s}$ and $\lambda_f = \sqrt{2\pi / n_s}$. Table 2.1 gives values of λ_f for widths ranging from 1 to 5 fully occupied subbands. The values are calculated by assuming that $|k_f|$ is equal to the magnitude of the first unoccupied transverse band. With this assumption, one can write

$$n_s = \frac{2}{W}\sum_{i=1}^{m-1}\sqrt{m^2 - i^2}$$

where m is the number of the first unoccupied transverse sub-band. Assuming m and knowing n_s, one solves W. Then the Fermi wavevector in the ith band, k_{xf_i}, is given by

$$k_{xf_i} = \frac{\pi}{W}\sqrt{m^2 - i^2} \quad .$$

With a single mode, the voltage period will be $\Delta V = \lambda_f V_t/2d$. With multiple modes, there will be multiple frequencies. The lowest transverse mode may not correspond to the dominant frequency in the power spectral density of the oscillations. The higher transverse modes have a higher transmission coefficient into the perpendicular probes which may result in a greater influence on the resistance measured. Numerical simulations have been done on a similar device. The device and results of the simulations are shown in Fig. 2.3. For a single transverse mode, 100% conductance modulation is achieved. For eight transverse modes, the percent modulation is less than 50% and there are multiple frequencies involved.

The implications for device fabrication are clear. To maximize both the percent modulation and periodicity of the oscillations, the electrical conducting width of the channels should be as narrow as possible.

2.3 Introduction to Quantum Phenomena in the Diffusive Regime

After fabricating a quantum wire, one is interested in determining the electrical width and the carrier density. These two parameters determine the number of transverse modes which is a vital parameter for the two ballistic devices described. Given the width and carrier concentration, one can quickly find the mobility and thus the mean free path. Another parameter, especially important for interpreting data from the diffusive transport regime, is the phase breaking length. The low field carrier concentration can be obtained approximately from the classical Hall effect. For one dimensional structures, the conductivity changes from the two dimensional value; therefore, the electrical width cannot be obtained by scaling a four point probe resistance measurement. Also, the electrical linewidth is not the same as the physical linewidth due to edge depletion. To determine the electrical linewidth and therefore the elastic scattering length, one must interpret data arising from quantum phenomena in the diffusive regime. In a typical sweep of resistance

Table 2.1. Fermi wavelengths for widths containing 1 to 5 full transverse sub-bands. Numerical values are for $n_s = 2 \times 10^{11}$ cm^{-2}.

FULL BANDS	Width(nm)	Band	λ_f(nm)
1	$1.861/\sqrt{n_s} = 41.6$	1	$2.149/\sqrt{n_s} = 48.0$
2	$3.183/\sqrt{n_s} = 71.2$	2	$2.847/\sqrt{n_s} = 63.7$
		1	$2.250/\sqrt{n_s} = 50.3$
3	$4.468/\sqrt{n_s} = 99.9$	3	$3.378/\sqrt{n_s} = 75.5$
		2	$2.580/\sqrt{n_s} = 57.7$
		1	$2.307/\sqrt{n_s} = 51.6$
4	$5.741/\sqrt{n_s} = 128$	4	$3.828/\sqrt{n_s} = 85.6$
		3	$2.871/\sqrt{n_s} = 64.2$
		2	$2.506/\sqrt{n_s} = 56.0$
		1	$2.344/\sqrt{n_s} = 52.4$
5	$7.008/\sqrt{n_s} = 157$	5	$4.226/\sqrt{n_s} = 94.5$
		4	$3.134/\sqrt{n_s} = 70.1$
		3	$2.698/\sqrt{n_s} = 60.3$
		2	$2.478/\sqrt{n_s} = 55.4$
		1	$2.369/\sqrt{n_s} = 53.0$
2-Dimensions			$2.507/\sqrt{n_s} = 56.0$

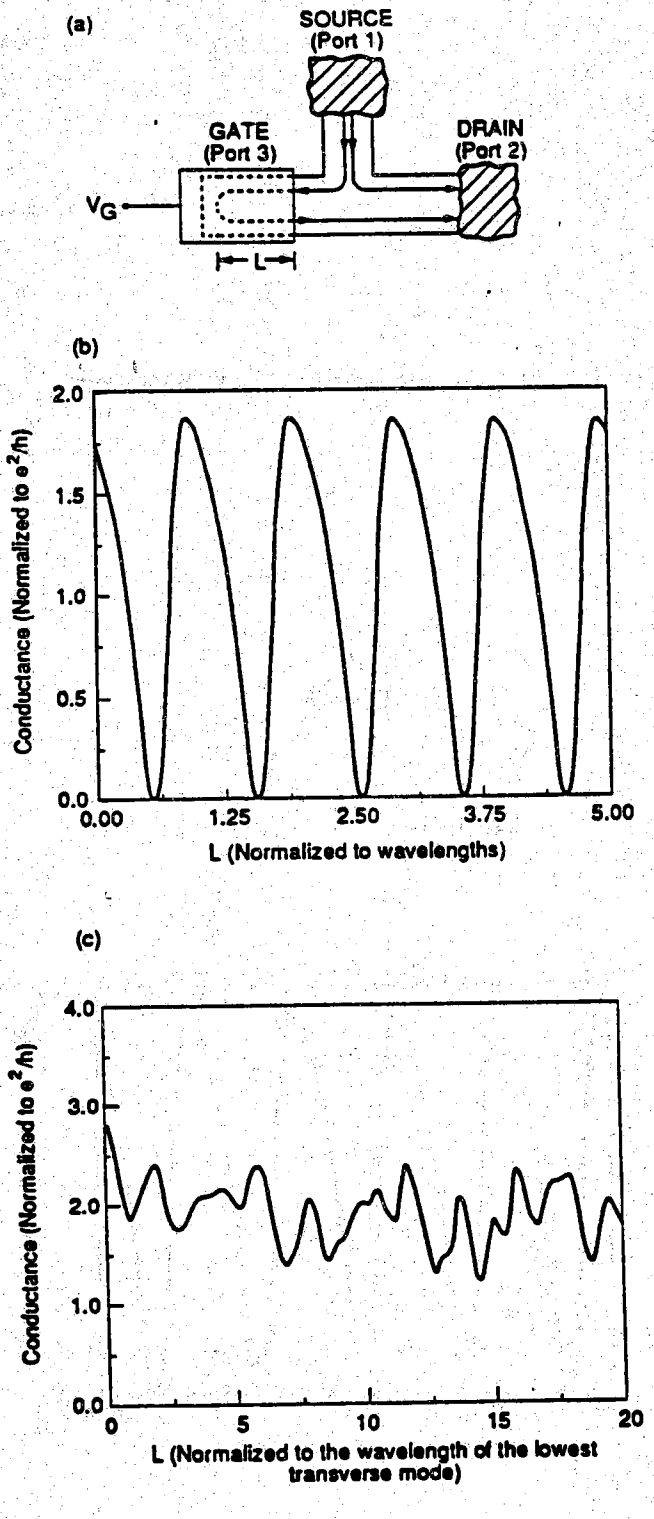

Figure 2.5 Numerical simulations of a quantum resonator (after ref. 20). (a) Device simulated. (b) Single moded (c) Eight modes

versus magnetic field, one can observe all of the quantum mechanical phenomena that will be described, (see Fig. 2.4).

In the following sections, quantum phenomena in the diffusive regime are described from the point of view of a process engineer wishing to use the phenomena as a diagnostic tool. The emphasis is on effects pertaining to and peculiarities of one dimensional confinement. The phenomena described are the diffusive Aharonov-Bohm effect, localization, electron-electron interaction, boundary scattering, universal conductance fluctuations, and Shubnikov de Haas oscillations.

2.4 The Diffusive Aharonov Bohm Effect

A lateral ring structure exhibiting the diffusive Aharanov-Bohm effect is the best test device for characterizing one dimensional wires. Both the electrical linewidth and an approximation for the inelastic scattering length can be extracted from a Fourier analysis of the conductance oscillations.

Before the first successful metal ring experiment [21], there was theoretical disagreement as to whether quantum interference could occur in a metal since electron transport is diffusive; the electrons follow a random walk type path. Experiments, however, show that interference does occur. Oscillations of conductance versus magnetic field with a period corresponding to the fundamental flux $\frac{h}{e}$ are observed. Two length scales are important to understand this phenomenon: the elastic scattering length, L_e, or the mean free path and the phase breaking length, L_ϕ, which is approximately the inelastic scattering length. In between elastic scattering events, an electron maintains a coherent momentum eigenstate and between inelastic scattering events an electron maintains a coherent energy eigenstate. The elastic scattering events do not destroy phase coherence. All of the electrons that traverse a particular path shorter than L_ϕ, arrive in phase. Extension of the theory of universal conductance fluctuations to the case of rings gives a predicted rms conductance fluctuation amplitude, ΔG, of $\sim 0.4e^2/h$ assuming that the arms of the ring are shorter than L_ϕ [14]. For armlengths greater than L_ϕ, the magnitude of Aharonov-Bohm conductance oscillations falls off exponentially. Data for an antimony ring fit the following relationship well [14]

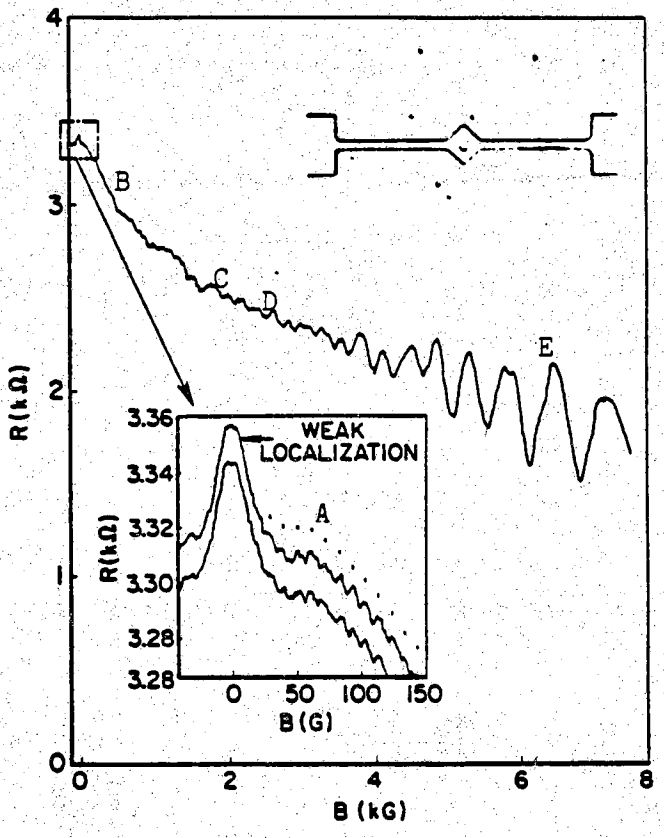

Figure 2.6 Illustration of different quantum interference phenomena (after ref. 3). A) Aharanov-Bohm oscillations, B) Boundary scattering (large negative $\partial R_{xx}/\partial B$), C) Universal conductance fluctuations, D) Electron-electron interaction (monotonic term), E) Shubnikov-deHaas oscillations.

$$\Delta G = \frac{e^2}{h}\left(\frac{2\pi hD}{L_\phi{}^2 K_B T}\right)^{\frac{1}{2}} e^{\frac{-\pi r}{L_\phi}} \tag{2.5}$$

where D is the diffusion coefficient, K_B is Boltzmann's constant, and r is the radius of the ring. The strong length dependence is because the number of coherent electrons arriving at the end of the loop decreases exponentially once the armlengths are greater than L_ϕ. This is quite different from the weak power law dependence for the universal conductance fluctuations which will be described later. To maximize the inelastic scattering length, all quantum interference experiments are performed at liquid He temperatures. L_ϕ is then on the order of 1 - 10 μm.

Since the first demonstration of the Aharonov Bohm effect in a semiconductor ring structure [1], the ring has become widely used as a test device for determining the electrical line width [1,2,4]. The reason for the use is its simplicity. Magnetic Aharonov-Bohm oscillations are Fourier analyzed and the width of the fundamental frequency corresponding to the flux h/e is determined. This width is considered to correspond to the areas determined by the inside and outside diameters of the ring. Thus, the upper and lower bounds of the fundamental frequency would correspond to $\frac{e}{h}\pi r_o{}^2$ and $\frac{e}{h}\pi r_i{}^2$ where r_o and r_i are the outer and inner radius, respectively.

The relative amplitude of the harmonics allow one to estimate L_ϕ according to (2.5). The square root of the power spectral density amplitudes of the fundamental and harmonics corresponding to the flux h/e, h/2e, h/3e, etc. should decay as $\exp(-L/L_\phi)$ where $L = \pi r, 2\pi r, 3\pi r$ respectively. This ignores coupling to the leads which reduces the transmission coefficient of the harmonics. Therefore, if A_1 and A_2 are the respective amplitudes of the fundamental and first harmonic, then $L_\phi = 2\pi r/\log(A_1/A_2)$.

The conductance oscillations due to the Aharanov- Bohm effect are found to be suppressed when the cyclotron radius is approximately one half of the linewidth, that is when $\sqrt{\hbar}/eB = W/2$ [1].

2.5 Localization

Localization falls into two regimes, strong and weak. The strong localization regime is not particularly relevant for the present discussion, but it will be described briefly for completeness. In the strong localization regime, the electron states are localized in space with exponentially decaying

envelopes. An electron moves from state to state via tunneling and thermionic emission, a process that is termed "variable range hopping" [22]. In two dimensions, the conductivity σ, follows the relation [22]

$$\sigma \propto \exp - \left[\frac{3\alpha^2}{N(E_f)K_B} \left(\frac{1}{T} \right) \right]^{\frac{1}{3}}$$

where $N(E_f)$ is the density of states at the Fermi level, K_B is Boltzmann's constant, T is temperature, and α is approximately the inverse half width of the localized wave function. Strong localization is the condition of an insulator and will only be seen in this work when a conducting channel is almost completely pinched off.

Weak localization is a more interesting effect for low dimensional, low temperature, semiconductor measurements. Under the conditions that the elastic scattering length is much less than the linewidth, the asymptotic formula derived by Altshuler and Aranov, (2.6), can be used to find both the linewidth and the phase breaking length. Although one sees the use of (2.6) on high mobility narrow wires [2,23], its validity in such instances is questionable [24]. The results obtained, however, are not unreasonable. Weak localization is a quantum interference phenomenon that gives rise to a small negative correction to the conductance predicted by the Boltzmann Transport Equation (BTE). The correction is on the order of e^2/h. The same two time and length scales that govern the diffusive Aharonov-Bohm effect also govern weak localization. They are the elastic and inelastic scattering times, τ_e and τ_ϕ and the corresponding elastic and inelastic scattering lengths, L_e and L_ϕ. The lengths are related to the times in the usual way by the diffusion coefficient, D.

$$L_e = \sqrt{D\tau_e}$$

and

$$L_\phi = \sqrt{D\tau_\phi}$$

The diffusion coefficient given by the Einstein relation in the degenerate, zero temperature limit is

$$D = \frac{n\mu}{e} \frac{1}{N(E_f)}$$

where $N(E_f)$ is the density of states at the Fermi level, n is the carrier concentration, and μ is the mobility. This can be re-written as

$$D = \frac{1}{d} v_f^2 \tau_e$$

where d is the dimensionality (1, 2, or 3) and v_f is the Fermi velocity. At liquid Helium temperatures in metals L_ϕ becomes much greater than L_e and an electron can scatter many times before it loses its phase coherence. Within a box of length L_ϕ, electrons can interfere coherently, but the phases of different electrons are very different so that an ensemble average gives no net result. However, there is one exception, electrons that interfere with themselves by following a circular trajectory. Such a trajectory can be formally associated with a time reversed pair of electrons that traverse the path in opposite directions and are mutually coherent. Thus, their interference does not average out but gives rise to a slightly larger backscattered wave than would otherwise be expected. The increased probability of reflection results in a small negative correction to conductance. The theoretically predicted corrections to the conductivity are [25]

$$\sigma_{3D} = \sigma_o - \frac{e^2}{\hbar \pi^3}\left[\frac{1}{L_e} - \frac{1}{L_\phi}\right]$$

$$\sigma_{2D} = \sigma_o - \frac{e^2}{\hbar \pi^2} \ln\left[\frac{L_\phi}{L_e}\right]$$

$$\sigma_{1D} = \sigma_o - \frac{e^2}{\hbar \pi}\left[L_\phi - L_e\right]$$

where σ_o is the Boltzmann conductivity, and σ_{id} is the actual conductivity for i dimensions.

Using the model of time reversed states on a circular trajectory, it is clear that a perpendicular magnetic field will affect the interference and therefore conductance. The weak localization effect is completely suppressed when the cyclotron radius of the time reversed pair becomes less than the minimum of L_e or W where W is the width of the channel [23,26]. In formula form, suppression occurs when $(\hbar/2eB)^{1/2} < L_e$ or when $B > \frac{\hbar}{2eL_e^2}$. In two dimensions, due to the simple relationship between the Fermi energy and the sheet carrier concentration, the above criterion for the field, B_c, at which suppression occurs can be written as

$$B_c = \frac{e}{h}\frac{1}{\mu^2 n_s}$$

or

$$B_c = \frac{e^3}{h} n_s R_s^2$$

where μ is mobility, n_s is sheet carrier concentration, and R_s is sheet resistance. For a mobility of 60 m^2/Vs and a carrier concentration of 2 x $10^{15} m^{-2}$ which are typical values from the samples used in this work, the critical field is 0.336 Gauss.

Generally, test equipment, and in particular, the test equipment used in this work is not capable of resolving a conductance versus magnetic field curve in one third Gauss. In other words, the effect will be suppressed before it can be seen. However, the critical field is inversely proportional to the mobility squared so B_c increases rapidly for lower mobility samples. For mobilities of less than $\sim$ 10 m^2/Vs, or line widths less than 1/2 micron, the relationship due to weak localization between between conductance and magnetic field provides a tool for determining the two critical parameters in one dimensional transport, line width, W, and L_ϕ.

The dependence of the change in conductance on magnetic field is derived by Altshuler and Aharonov [27]. For a wire with width and height small compared to L_ϕ and length large compared to L_ϕ, the change in conductance, δG is

$$\delta G = -\frac{1}{L}\frac{e^2}{\pi\hbar}\left[\frac{1}{L_\phi^2} + \frac{e^2B^2W^2}{3\hbar^2}\right]^{-1/2}$$

Using $\delta G = -\frac{\delta R}{R^2}$ gives

$$\frac{\delta R}{R} = \frac{R}{L}\frac{e^2}{\pi\hbar}\left[\frac{1}{L_\phi^2} + \frac{e^2B^2W^2}{3\hbar^2}\right]^{-1/2} \qquad (2.6)$$

where L is the length of the wire and W is the width. Choi and Tsui use this equation to determine W and L_ϕ in low mobility ($2.7 m^2/Vs$) AlGaAs-GaAs heterostructure [28]. Magnetoresistance is measured, then the data is fitted to the above equation using L_ϕ and W as the fitting parameters. The uncertainty is estimated to be within $\pm$20%. Thornton, Pepper, Ahmed, et.al. perform a similar experiment on a high mobility ($20 m^2/Vs$), narrow (45 nm) AlGaAs-

GaAs resistor [23]. Magnetoresistance is measured and fitted to (1.3) for temperatures ranging from 0.41K to 1.0K. The inelastic scattering length is found to fit the following relation.

$$L_\phi = 0.16\ T^{-1/3}$$

The theoretical relation is [23]

$$L_\phi = \left[\frac{DGL\hbar^2}{2e^2K_BT}\right]^{1/3} \tag{2.7}$$

where G and D are the Boltzmann values of the conductance and the diffusion coefficient. For the values of σ and D appropriate to the test samples, (1.4) predicts that $L_\phi = 0.56\ T^{-1/3}$ μm. The $T^{-1/3}$ dependence indicates that the dominant scattering mechanism is a low energy process arising from electromagnetic fluctuations. As the width of the resistor is reduced further by a transverse electric field, the $T^{-1/3}$ dependence changes to a T^2 dependence. With even more confinement, an exponential dependence is found indicating strong localization.

For two dimensions, the change in conductance due to magnetic field is [29]

$$\delta\sigma = \alpha\frac{se^2}{\pi\hbar}\left\{\Psi\left[\frac{\hbar}{4eBL_\phi^{\,2}}+\frac{1}{2}\right] - \Psi\left[\frac{\hbar}{4eBL_e^{\,2}}+\frac{1}{2}\right] + \ln\left[\frac{L_\phi}{L_e}\right]\right\}$$

where α is a constant of order unity, s is the product of the spin and orbital degeneracies and for GaAs-AlGaAs s=2, and $\Psi(\cdot)$ is the digamma function. The parameters α and L_ϕ can be found from a least squares fit of the data.

In summary, for a one dimensional wire, one can find L_ϕ and W, under the conditions that $L_e \ll$ W, by fitting the low field section of the R_{xx} versus B curve to (2.6) using W and L_ϕ as fitting parameters.

2.6 Boundary Scattering

For one dimensional devices, there is often a sharp negative magnetoresistance as shown in section B of Fig. (2.6) [1,2,3,26,30]. This is something of a signature of one dimensional transport. The effect is investigated theoretically in an ad-hoc way by reformulating the weak localization correction for the case when $W < L_e$ [24]. The effect has been observed and commented upon by a number of experimentalists and their

observations will be discussed. In [26], the effect is investigated experimentally by Choi, Tsui, and Palmateer who find the following. The magnetoresistance is almost temperature independent in a range between $\sim$ 0 and 10 Kelvin which contradicts 1D and 2D interaction theory. The effect is suppressed when the cyclotron diameter is equal to the channel width. That is when $B \approx \frac{4\hbar}{eW^2}$. The total percent change in R, $|\delta R/R|$, is larger for smaller W. Shubnikov de Haas oscillations are observed to begin at higher fields in narrower channels.

The hypothesis to explain the observed phenomena is as follows. At zero magnetic field, the boundary scattering is specular and does not affect the conductivity. With high mobility samples, say 60 m^2/Vs, transport approaches the high field limit, $B\mu \sim 1$, at the relatively low field of 170 Gauss. In the high field limit, scattering sites are needed for current transport. They are provided by the boundaries thus reducing resistivity. The effect saturates when the electrons are able to make complete orbits between the boundaries.

The hypothesis provides the following explanation for the observed phenomena. The decrease in resistance is proportional to the scattering rate which is inversely proportional to the width thus explaining the $|\delta R/R|$, W relationship. The boundary scattering decreases the effective τ in the relationship $\omega_c \tau \sim 1$ which must be satisfied for the onset of Shubnikov de Haas oscillations. Thus the onset is delayed.

A slightly different result and hypothesis is presented by Simmons, Tsui, and Weimann in reference 3. Here the 1D resistivity of a 0.8 μm channel at B=0 is 5.7 times the 2D resistivity. The inelastic scattering length, derived from the magnitude of universal conductance fluctuations and also from weak localization measurements, is 2 μm in the range $B < 0.5$ kG and 12 μm in the range $4 < B < 5$ kG. This is to be expected from the relationship between L_ϕ and σ in (1.4) or from the simple argument that $L_\phi = \sqrt{D\tau_\phi}$ which is the same as $L_\phi = v_f\sqrt{\tau_e \tau_\phi}$.

The hypothesis is that the boundary scattering is diffusive thus reducing the elastic scattering time. As the cyclotron orbit becomes smaller than the channel width, the scattering is suppressed and the conductance returns to its 2D value. However, the experimental results are not in good quantitative agreement. The 2D resistance value occurs at 7 kG, a value for B much greater than the value at which the cyclotron radius equals W/2. Some of this

effect is due to decreased carrier concentration from the two dimensional value as will be discussed under the section Shubnikov-deHaas Oscillations. Since $\rho = (e\mu n)^{-1}$, a decreased carrier concentration will increase resistance. A decrease in carrier concentration by approximately a factor of two from the two dimensional value has been seen in our labs and elsewhere [1,3,10,11]. Furthermore, for weak interaction, $L_\phi \propto (\mu n)^{2/3}/N(E)^{1/3}$ from (1.4). Thus, a reduction in n would also reduce L_ϕ. This is all qualitative, but it is an effect that has not been previously mentioned.

This hypothesis is also consistent with the results of the experiment mentioned earlier of Thornton, Pepper, Ahmed, et al. [23]. For a high mobility (20 m^2/Vs) GaAs-AlGaAs resistor of width 45 nm, the measured values for L_ϕ range between 0.22 and 0.15 μm in the temperature range between $\sim$ 0.5 and 1.0 K. In a two dimensional resistor, the expected value for L_ϕ is on the order of 10 μm.

The apparent reduction in the elastic and inelastic scattering lengths in highly quantized one dimensional wires is an obstacle in the way of fabricating one dimensional devices in which one can observe the ballistic regime.

2.7 Electron - Electron Interaction

Electron-electron interaction phenomena enable one to determine the electrical linewidth by a temperature dependent study of conductance. In low mobility samples, weak localization and electron - electron interaction effects are mixed. However, in high mobility samples, weak localization effects are quenched within a few tens of Gauss and interaction effects predominate. In the metallic regime, $E_f\tau_e \gg \hbar$, electron - electron interaction gives the following corrections to the Boltzmann conductivity for two, one, and zero dimensions [26, 30].

$$\delta\sigma_{2D} = -\frac{1}{2\pi^2}\frac{e^2}{\hbar}g_{2D}\left\{\Psi\left[\frac{1}{2}+\frac{\hbar}{K_B T\tau_e}\right] - \Psi\left[\frac{1}{2}\right]\right\}$$

$$\delta\sigma_{1D} = -g_{1D}\frac{e^2 L_T}{\sqrt{2}\pi^2\hbar\, W}$$

$$\delta\sigma_{0D} = -s\frac{e^2}{\sqrt{2}\pi^2\hbar\, W}L$$

The variables g_{2D}, g_{1D}, and s are interaction parameters described in reference 26. $\Psi(\cdot)$ is the digamma function. τ_e is the elastic scattering time. W and L are the channel width and length respectively. L_T is the thermal diffusion length, in this case defined as follows.

$$L_T \equiv \pi\left[\frac{\hbar D}{K_B T}\right]^{1/2}$$

One sees several definitions in the literature differing by $\sqrt{\pi/2}$. When W is less than the thermal diffusion length, L_T, the interactions become one dimensional. If the length, L, is also less than L_T, then the interactions are zero dimensional. Note however, that all $\delta\sigma$'s have the units of $\delta\sigma_{2D}$ which has the units of conductance.

Although $\delta\sigma$ is not a function of magnetic field, after inverting the conductivity tensor, one finds that $\delta\rho$ follows a square law relationship given by

$$\delta\rho(B) = \left[\frac{e\tau_e}{m^*\sigma_o}\right]^2 B^2\delta\sigma_i \tag{2.8}$$

where $\delta\sigma_i$ is the $\delta\sigma$ of the appropriate dimension and σ_o is the Boltzmann conductivity. Equation (2.8) describes the monotonic component of the resistance versus magnetic field curve after boundary scattering effects have been suppressed. It can be used to differentiate the regions associated with interaction effects and boundary scattering effects and to estimate a value, $\delta R/R$, due to boundary scattering. For example, see Fig. 3 of reference 26.

One method described for finding W from the interaction phenomenon is the following [31]. The one dimensional conductivity correction due to interaction, rewritten in a more straightfoward form is

$$\delta\sigma = -g_{1D}\frac{e^2}{\pi\hbar}\left[\frac{\hbar D}{2K_B T}\right]^{1/2}$$

where the 1D interaction parameter has a value of 1.33. A perpendicular magnetic field is applied sufficient to suppress localization. The conductance, $G = \sigma/L$, (where L is the channel length) is measured as a function of temperature and plotted versus $T^{-1/2}$. The diffusion coefficient D is determined

by the best straight line fit and the extrapolated $T^{-1/2}$ intercept gives the value for the Boltzmann conductance given by the Einstein relation

$$G_B = N(E_f)De^2\frac{W}{L} \quad . \tag{2.9}$$

For 4 or more occupied transverse subbands, the two dimensional density of states is a good approximation. Thus everything is known in (2.9) except W which allows W to be determined.

2.8 Universal Conductance Fluctuations

From universal conductance fluctuations, one can determine both L_ϕ and W. The universal conductance fluctuation phenomenon results from the quantum interference of electrons due to a random array of elastic scattering sites within a box of side L_ϕ. This gives rise to reproducible, sample specific, aperiodic fluctuations in plots of resistance versus magnetic field or chemical potential. For lengths $L > L_\phi \approx L_e$, the rms amplitude of the fluctuations is on the order of e^2/h [11]. The magnitude of the fluctuations and their correlation in magnetic field gives information about both the width and phase breaking length.

Two length scales are of importance, L_ϕ and L_T where [32]

$$L_T = \left[\frac{hD}{K_BT}\right]^{1/2} \tag{2.10}$$

Re-writing (2.10) in the form of the Heisenberg uncertainty principle gives

$$\left[K_BT\right]\left[\frac{L_T^2}{D}\right] = h$$

One can view L_T as the length corresponding to the time corresponding to the thermal smearing of K_BT. After traveling a length $L_T < L_\phi$, diffusing waves at different energies get out of step. In general for semiconductor work, L_ϕ is less than L_T so L_ϕ becomes the limiting length scale.

The rms amplitude of the conductance fluctuations is

$$\delta G_{rms} = \sqrt{<\delta G^2> - <\delta G>^2}$$

where

$$\delta G = G(E_f,B) - <G(E_f,B)> \quad .$$

For a quasi one dimensional wire, where $W < L_T, L_\phi$, δG_{rms} is given by [33]

$$\delta G_{rms} = a\frac{e^2}{h}\left[\frac{L_T}{L}\right]\left[\frac{L_\phi}{L}\right]^{1/2} \qquad L_T \ll L_\phi < L \tag{2.11a}$$

$$\delta G_{rms} = a\frac{e^2}{h}\left[\frac{L_\phi}{L}\right]^{3/2} \qquad L_\phi \ll L_T < L \tag{2.11b}$$

where L is the wire length. For $W << L_\phi$, $a = 0.729$.

In the two dimensional case, for $L_\phi < L_T$, the sample can be regarded as a number of phase coherent units in series and parallel. One divides up the sample into squares of length L_ϕ forming a dimensionless length, $N = L/L_\phi$, and width, $M = W/L_\phi$. Then δG_{rms} is given by [34]

$$\delta G_{rms} = M^{-1/2}N^{-3/2}\frac{e^2}{h}$$

The correlation function, $F(B,\Delta B)$, is defined by

$$F(B,\Delta B) = <\delta G(B)\delta G(B+\Delta B)> - <\delta G(B)>^2$$

The magnetic correlation length is defined as the magnetic field, B_c, where $F(B,B_c) = 1/2\ F(B,0)$. The correlation field is the field at which one or two flux quanta, h/e, are contained in a phase coherent square thus reducing the phase correlation of the random fluctuations. For a quasi one dimensional sample, the relationships are [33]

$$B_c = 1.2\frac{h}{e}/WL_\phi \qquad L_\phi < L \tag{2.12a}$$

$$B_c = 1.2\frac{h}{e}/WL \qquad L < L_\phi \tag{2.12b}$$

Using (2.11) and (2.12), one can obtain both the electrical line width and phase breaking length by the following procedure.

1) Plot the conductance versus magnetic field.
2) Subtract off the background.
3) Calculate the correlation function, $F(B,\Delta B)$.
4) Use (2.11) and solve for L_ϕ
5) Determine the cutoff field B_c, where $F(B,B_c) = 1/2\ F(B,0)$.
6) Solve for W using (2.12).
7) With W known, calculate D using the Einstein relation, (2.9). For channel widths such that 4 or more subbands are occupied, the two dimensional density of states is a good estimate for $N(E_f)$.

8) Calculate L_T and check that the appropriate equations, a or b, of (2.11) and (2.12) were used.

For devices of lengths less than the elastic scattering length, none of the above is correct. Fluctuations in resistance of 100% have been seen giving values for δG of $5e^2/h$ [11].

2.9 Shubnikov-deHaas Oscillations

Shubnikov-deHaas oscillations allow one to determine the high field carrier concentration. When a perpendicular magnetic field is applied to a two dimensional electron gas, the electrons undergo cyclotron motion with frequency $\omega_c = eB/m^*$. The Hamiltonian can be cast in the form of a harmonic oscillator giving quantized energy levels $E = (i + 1/2)\hbar\omega_c$ where $i = 0,1,2,....$ Discrete energy levels will only become apparent when an electron can make a complete revolution before being scattered. In other words, when $\omega_c \approx 2\pi/\tau$ or when $\mu B \approx 2\pi$ where μ is the mobility. Also, the spacing between energy levels, $\hbar\omega_c$, must be larger than the thermal smearing, K_BT. Due to finite temperature, the energy levels will appear as in Fig. 2.5. When a level is half full, the system is in a metallic state and the diagnol conductivity, σ_{xx}, is large. When the last level is completely full, the system is in an insulating state, and σ_{xx} approaches zero. Thus conductivity and resistivity oscillate as a function of magnetic field. The number of electrons per unit area that can fit in any state is

$$N(E)\Delta E = \frac{m}{\pi\hbar^2}\hbar\omega_c = 2e\frac{B}{h} \quad .$$

For a full last level, $n_s = i\ 2eB/h$, or $1/B = i\ 2e/hn_s$ where i is some integer. Therefore, the conductivity and resistivity are periodic in inverse magnetic field with a periodicity, $\Delta(1/B)$, given by

$$\Delta(1/B) = \frac{2e}{hn_s} \quad . \tag{2.13}$$

Equation (2.13) gives the relation for determining the high field carrier concentration, n_s.

One dimensional structures show several anamolies in the Shubnikov-deHaas effect that have not yet been rigorously explained. The following results are all from high mobility, $\mu > 10\ m^2/Vs$, GaAs-AlGaAs heterostructures. In reference 36, a Hall bridge of width 8.9 μm is compared to one of width 380 μm. The shape of the SdH oscillations change from being

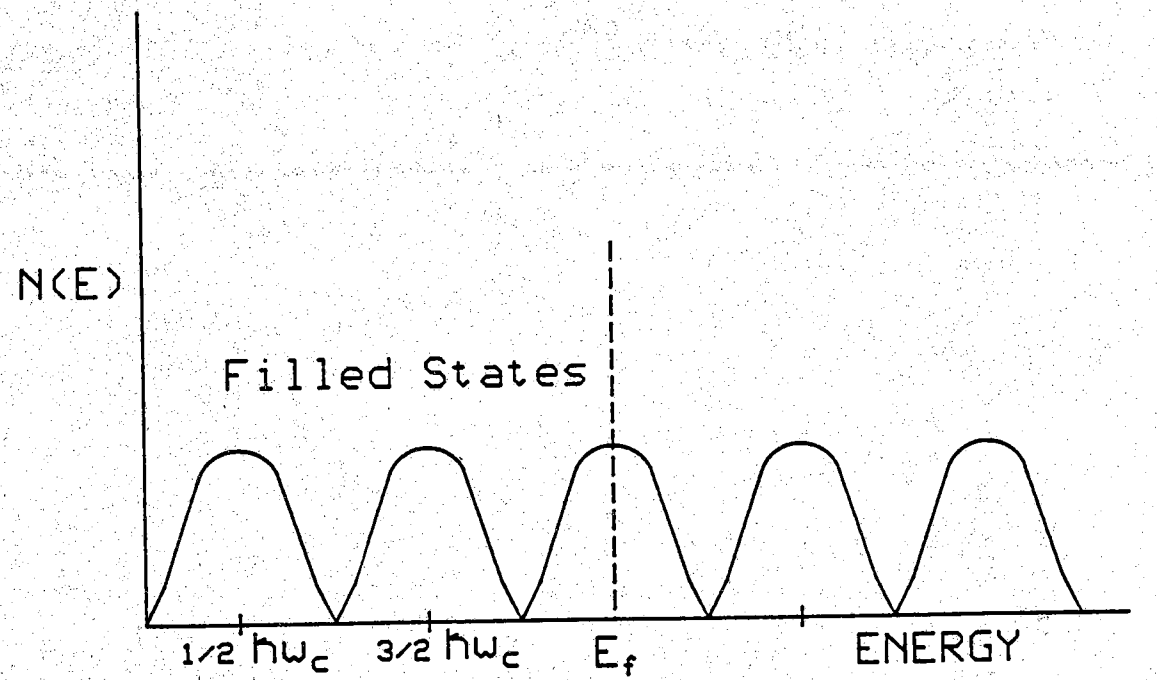

Figure 2.7 **Energy levels at nonzero temperature from SdH effect.**

fairly symmetric in the two dimensional regime to noticably saw toothed in the one dimensional regime. The magnitude of the peaks in ρ_{xx} are approximately four times smaller for the one dimensional bridge than for the corresponding peaks of the two dimensional bridge. Furthermore, this size effect does not saturate until the width of the bridge is approximately 400 μm. In reference 31, a pronounced departure from the 1/B periodicity occurs especially at low B for channels of width less than 250 nm. It is suggested that the effect is due to one dimensional subbands being forced through the Fermi level by an increasing perpendicular magnetic field giving rise to increased transverse magnetic confinement.

The "high field" distinction is made for carrier concentration because in one dimensional devices, the high field concentration is generally found to be different from the low field concentration determined by the classical Hall effect and both are found to be different from values obtained from large two dimensional devices [1,3,10,11]. The low field, one dimensional value is found to be the smallest. This could be due to edge depletion. The next highest is the high field one dimensional value. This is thought to be due to increased transverse confinement from the magnetic potential [11,35]. The largest value is from the two dimensional device. Typical values in ascending order are (in cm^{-2}) 2.0×10^{11}, 2.6×10^{11}, and 3.9×10^{11} [11].

2.10 Summary

The easiest method for determining the electrical linewidth and obtaining an estimate of the phase breaking length, L_ϕ, is to build a ring structure, measure R_{xx} and R_{xy} versus B, plot G_{xx} ($= R_{xx}/(R_{xx}^2+R_{xy}^2 L/W)$) versus B. Compute the power Fourier transform. The lower, center, and upper bounds of the peak corresponding to the fundamental frequency are equal to $\pi r_i^2 e/h$, $\pi r_c^2 e/h$, and $\pi r_o^2 \frac{e}{h}$ respectively. This gives the inside, center, and outside radius of the ring. An estimate for L_ϕ can be obtained from the relative magnitudes of the peaks corresponding to the fundamental frequency and harmonics using (2.5).

On a low mobility sample, weak localization can be used to determine the electrical linewidth and the phase breaking length. The phenomenon occurs between 0 and several hundred Gauss. Thus one can make the approximation that $\delta G_{xx}=\delta R_{xx}/R_{xx}^2$ so that only R_{xx} versus B need be measured. This data can be fit to (2.6) using W and L_ϕ as fitting parameters.

Boundary scattering is a signature of 1D transport. The effect should be suppressed when the cyclotron radius is less than half the linewidth. Work has recently been done to incorporate the effect into the formula (2.6) for weak localization [24].

From electron-electron interaction, the width W can be obtained from a temperature dependent study of G_{xx}. G_{xx} is plotted versus $T^{-1/2}$. The slope gives the diffusion constant and the extrapolated G_{xx} intercept gives the Boltzmann conductance. Knowing n_s from classical Hall measurements or SdH oscillations, W can be determined by the Einstein relation, (2.9).

Using a Hall bridge with lengths between probes greater than L_ϕ universal conductance fluctuations allow one to calculate both W and L_ϕ. Both R_{xx} and R_{xy} versus B need be measured to calculate G_{xx}. The correlation function of the fluctuations is calculated giving a cutoff field, B_c, and rms magnitude of the fluctuations. From these two numbers, L_ϕ and W can be calculated following steps 1 - 8 at the end of section 2.8.

Shubnikov-deHaas oscillations provide a high field value of the sheet carrier concentration calculated from (2.13). The value is always intermediate between the low field 1D concentration and the 2D concentration. The increase from the low field value is due to increased confinement from the parabolic magnetic potential. In narrow, high mobility wires, Landau plots are non-linear at low fields due to magnetic depopulation of one dimensional sub-bands [20,31,35,37].

In chapter five, Aharanov-Bohm oscillations and Shubnikov-deHaas oscillations are used to determine the phase coherence length, electrical linewidth, and carrier concentration.

CHAPTER III
ELECTRON BEAM LITHOGRAPHY

3.1 Electron Beam Lithography: An Introduction

Electron Beam lithography is a system containing a focused electron beam and a stage on which to mount a workpiece. By a combination of beam deflection, beam blanking and stage movement, an appropriate pattern is exposed. The core of the system is the electron optical column. The necessary supporting equipment are vacuum pumps to maintain vacuum in the column and work chamber and a computer to control the pattern generation.

A great deal of effort in this work went into developing electron beam direct write. Since this was the first use of direct write at Purdue, an introduction to the subject will be given emphasizing the parameters that affect resolution. Much has been written on the subject, a number of books and reams of articles. Several books devoted in part or in whole to the subject are [38,39,40,41,22]. The conference proceedings of the International Symposium on Electron, Ion, and Photon Beams for the years 1983 - 1987 in [42 - 46] address all areas of the subject. For an introduction to the Cambridge EBMF2 and a description of its optics, see [47,48].

3.2 Electron Optics

Several types of beam shapes are used in electron beam lithography equipment. The most common, and the one corresponding to the Cambridge EBMF2 used in this work, is the Gaussian round beam. The source of the beam is a tungsten filament bent into a sharp point or single crystal lanthanum hexaboride emitter ground into a sharp point. The initial beam emitted from the filament is several hundred microns in diameter. The electron optics demagnify the beam several orders of magnitude. A schematic of the electron optics is shown in figure 3.1. These are the basic optics adopted from SEMs. The spray apertures limit the width of the beam by collecting

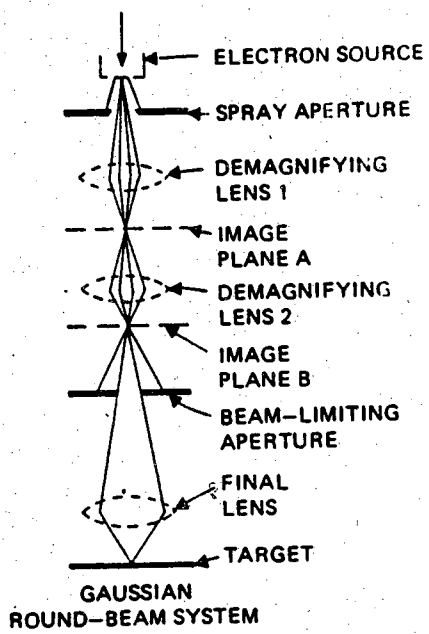

Figure 3.1. Electron optics (after ref. 38)

fringing electrons. The demagnifying lenses are magnetic lenses which demagnify the beam. The equation for magnification is m = o/i where o is the object distance, i is the image distance and m is the magnification.

Beam deflection is accomplished in several ways. The typical SEM method of beam deflection, shown in figure 3.2a, allows the workpiece to be close to the lens allowing a minimum image distance which gives maximum demagnification providing a minimum beam size. The drawback is that the deflection is limited. The method used by the Cambridge EBMF2 is shown in figure 3.2b. This method increases the image distance thus increasing the beam size and distortion, but large deflection is possible. Beam blanking is accomplished by two parallel plates centered at a beam crossover position. When blanking is desired, a potential is placed across the plates and the beam is shifted over and collected on a spray aperture.

The writing is accomplished by stage movement and beam deflection. Stage movement is used to move from one exposure field to the next and beam deflection is used to expose the field. A field is a set of $2^n \times 2^n$ address points where n is determined by the hardware of the system. For the Cambridge EBMF2, n = 15. The oldest method of exposure is the raster scan. The beam is scanned back and forth across the entire field covering every point and is only turned on when it comes to a feature. A more sophisticated method used by the Cambridge EBMF2 is the vector scan. The beam only scans over the features to be exposed and jumps from one feature to the next.

3.3 Resolution

Much work during the last decade has gone into determining the ultimate resolution of electron beam lithography. Since resolution is the parameter to maximize, it must be understood, but it does not have a clear mathematical definition like sensitivity and contrast which will be discussed later. Resolution only makes sense with respect to a particular type of feature whose size one is trying to minimize. For example given two patterns, one a grid of metal dots and the other a grating of metal lines both of which have similar dimensions, one cannot immediately say which pattern requires the highest resolution lithography. However, given two lines, one 20 nm wide and the other 50 nm wide, it is intuitively clear that the 20 nm line requires greater lithographic resolution. The pattern used to determine resolution is a grating, a set of periodically spaced lines [49,50,51]. The center to center distance of the lines is the pitch. There are two parameters of interest, linewidth and line spacing.

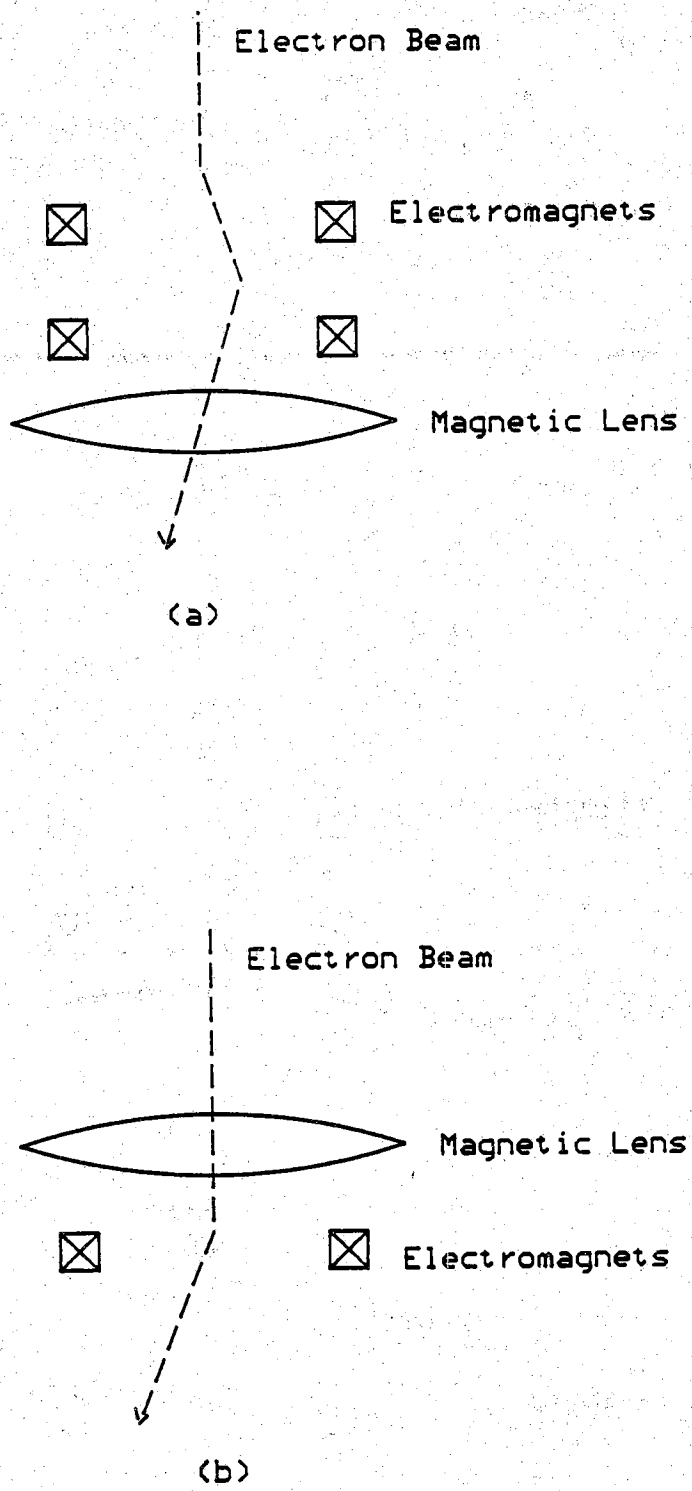

Figure 3.2. Beam deflection (after ref. 38) a) Prelens deflection. b) Postlens deflection

The two parameters are affected by every element of a lithographic process from sample preparation through development. A process can minimize one parameter at the expense of the other. An example is the use of bilayer resists which allow smaller linewidths to be delineated but require increased separation between the lines due to undercut of the bottom layer of resist [51]. In comparing two processes to determine which one gives the best resolution the judgement must be based on which process most closely satisfies one's fabrication needs. Finally, one can say that the process which achieves the ultimate resolution will give both the smallest linewidths and minimum line spacing.

The factors that affect resolution are the following: acceleration voltage, beam size and shape, pattern geometry, resist type, resist thickness, resist contrast, substrate atomic number, substrate thickness, developer, and pre-bake and post-bake temperatures and times. Once one understands what happens when an electron beam strikes an electron beam resist lying on a substrate, then one will understand the effect of the first nine factors. Three scattering processes occur. The incident beam scatters elastically which broadens the beam; the beam scatters inelastically generating low energy secondary electrons, and the beam backscatters from the substrate. The scattering processes give rise to the fundamental limits of resolution in electron beam lithography. The interaction of the electron beam, the electron beam resist, and the substrate will be described in the following section.

3.4 Primary Electrons

When the electron beam strikes the electron beam resist, it begins to scatter both elastically and inelastically. The elastic scattering can be modeled as Rutherford scattering using a screened coulomb potential. Elastic scattering dominates the electron direction and favors small angles [40 p. 98]. An analytical formula for electron beam spreading has been developed [52 p. 101]. The physical model is the following (see figure 2.3). A beam with a spatial delta function distribution enters the resist and undergoes one scattering event at a point mid-way through the resist. The formula for beam spreading is

$$b = 625 \frac{Z}{E_o} \frac{\rho^{1/2}}{A} t^{3/2} \tag{3.1}$$

where b (cm) is the region in which 90% of the electron trajectories lie, Z is

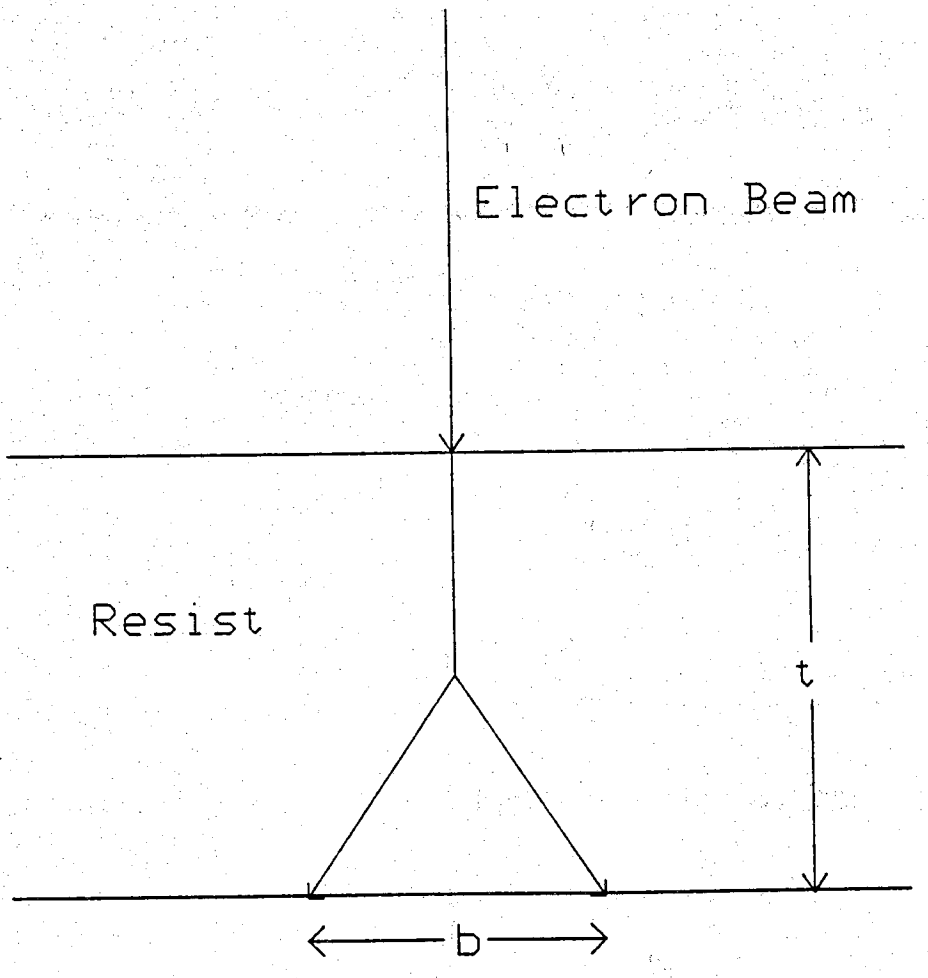

Figure 3.3. Elastic scattering model (after ref. 52)

the atomic number, A is the atomic weight, E_o (KV) is the electron energy, ρ (g/cm^3) is the density of the resist and t (cm) is the resist thickness. Since electron beam resist is composed of molecules, the average atomic number and atomic weight should be used. The predictions of equation 3.1 were compared to Monte Carlo simulations of electron beam spreading in thin films of Carbon, Aluminum, Copper, and Gold with thicknesses ranging from 100 Å to 0.5 μm and were found to agree within 40% [52 p. 103].

The analytical expression gives useful insight into the parameters affecting beam spreading. The two easiest parameters that one can modify to reduce beam spreading are E_o, the incident beam energy, and t, the resist thickness. The beam spreading is inversely proportional to the beam energy and proportional to the resist thickness raised to the three halves power. For minimum spreading, one should use maximum energy and minimum resist thickness.

3.5 Secondary Electrons

Elastic collisions only broaden the beam, but, by definition, impart no energy to the resist. For molecular scission or crosslinking to occur, energy must be imparted from the beam to the resist by inelastic collisions. The inelastic collisions create secondary electrons most of which have small energies and short path lengths; however, some have energy of up to one half the energy of the primary electrons and an initial trajectory parallel to the plane of the film [53,49]. The energy distribution of the secondary electrons is not a strong function of the energy of the primary electrons for primary electron energies greater than 100 eV; that is all useful energies for lithography [54]. Furthermore, the secondary electrons are largely responsible for the exposure of the resist. The rate of energy loss along a path, s, can be described by the Bethe continuous slowing down approximation,

$$\frac{dE}{ds} = -\frac{2\pi e^4 n_e}{E(s)} \ln\left[\frac{1.166E(s)}{I}\right] \tag{3.2}$$

where E is the electron energy, s is the path length, n_e is the electron density of the resist, e is the electron charge, and I is a mean ionization energy for atoms in the resist. The 1/E dependence in equation 3.2 is dominant. Therefore, the lower energy secondary electrons are more efficient at transferring energy to the resist. Monte Carlo simulations of 50 and 100 KeV electron beams passing through 0.1 μm of PMMA show that both the lateral

spread and the number of secondary electrons decreases with increasing beam energy [55]. This suggests that to minimize the broadening effect due to secondary electrons, the highest energy beam available should be used.

3.6 Backscattered Electrons

When the primary electrons pass through the resist and strike the substrate, some of the electrons are scattered back into the resist (see figure 3.4). Again, a first order model is Rutherford scattering. The atomic number, Z, of the substrate is much larger than the average atomic number of the resist. For PMMA, Z_{avg} is 3.6. For silicon and gallium arsenide, Z is 14 and 32, respectively. The probability of a scattering event is proportional to Z^2. By multiple scattering events, electron trajectories can pass through large angles, greater than 90° and thus be backscattered into the resist.

The energy density distribution of the backscattered electrons from a line scan can be modeled as Gaussian,

$$E(x) = \frac{D\eta_e}{\sqrt{\pi}\beta} e^{-\frac{x^2}{\beta^2}}$$

where η_e is the fraction backscattered of the total incident dose, D [38 p. 75, 30]. The parameters β and η_e have been measured for various incident beam energies, E, and the results are shown in table 3.1 [55].

Table 3.1. Backscattered energy spread

E (KeV)	β (μm)	η
20	2.0	.78
40	6.2	.70
60	13.1	.70
120	43.0	.76

The first thing to note is the relatively large values of β. Referring back to figure 3.2, for a 20 KeV beam, the spread of primary electrons is on the order of 0.1 - 0.2 μm. The spread of secondary electrons is on the order of 10 - 20

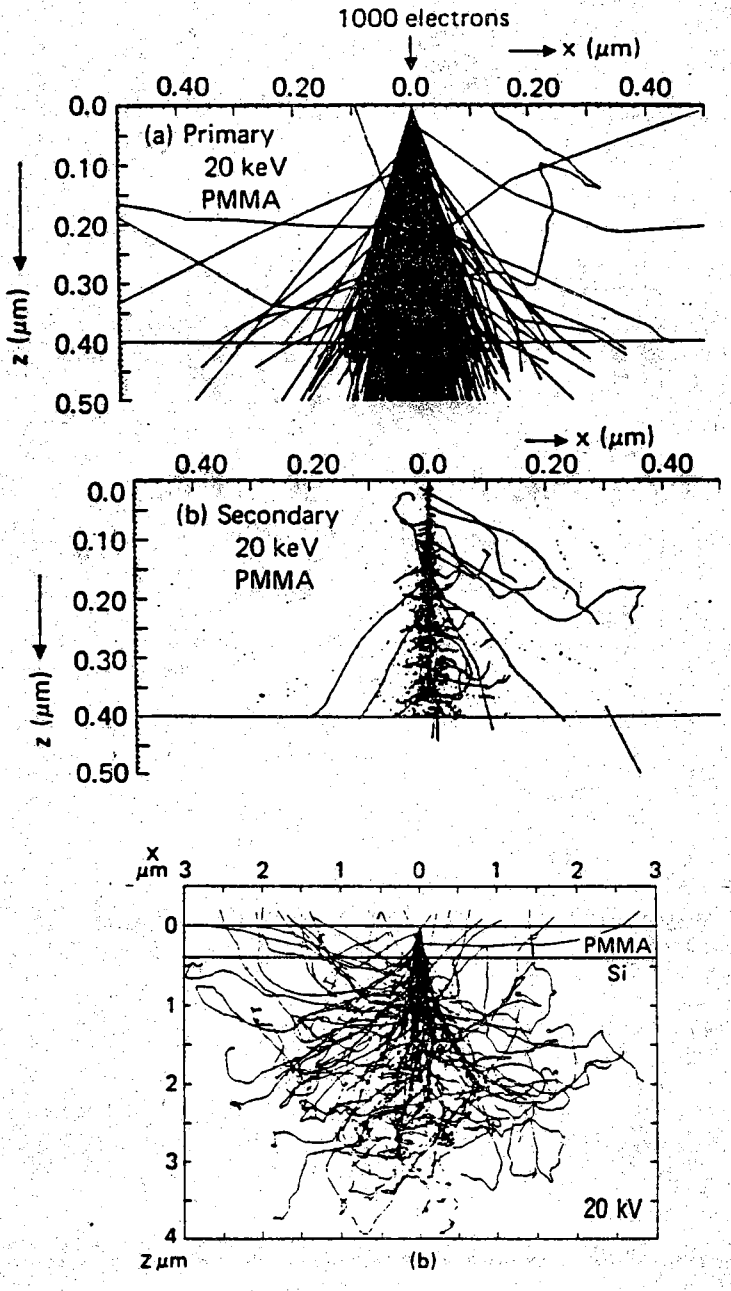

Figure 3.4. Monte Carlo simulations of primary, secondary and backscattering electrons (after ref. 38 p. 64 and 53 p. 1392)

nm. But the spread of backscattered electrons is 2 μm. Also, β increases with increasing energy and in fact is proportional to $E^{1.7}$ where E is the beam energy [55]. The second thing to notice is that η_e is almost constant, independent of energy. The effect of higher beam energy is to spread out backscattered electrons over a large area thereby reducing the energy density imparted to the resist. At high energies, greater than 50 KeV, the backscattered electrons can be thought of as providing a uniform background dose.

The effects of backscattering can be reduced by using a lower atomic number substrate, using a thin film substrate [56,57], using a high energy beam [58], and using multi-level resists [51,52]. The motivation behind the first three methods should be clear. Multi- level resists will be discussed later under the section Electron Beam Resists.

3.7 Beam Size and Shape

The effect of beam size is obvious. The minimum feature size cannot be much smaller than the minimum beam size. Therefore, for highest resolution, the beam size should be as small as possible. The minimum beam size is a feature of the equipment used. For SEMs, and STEMs converted for lithography, the minimum beam size ranges from 10 nm to 1/2 nm. For commercial electron beam lithography equipment, the minimum beam size is generally larger, up to 0.1 μm. This is the price paid for the greater deflection capability of commercial equipment. The working distance between the final lens and the work piece is larger, approximately 50mm for the Cambridge EBMF2, as opposed to approximately 3mm for an SEM.

The other two factors that affect beam size are column cleanliness and beam energy. The higher the beam energy, the more tightly the beam can be focused.

The effect of beam shape is more subtle. Figure 3.5 provides a good visual explanation. The solid lines represent the dose of an isolated feature for two different shape beams, one a square beam, and the other a Gaussian round beam. The linewidth will be determined by the width of the distribution at the necessary dose at the level of the arrows. When other features are exposed nearby, the backscattered electrons add a background dose to the distributions and the new line widths are determined by the width of the raised distributions at the level of the arrows. The advantage of a sharply

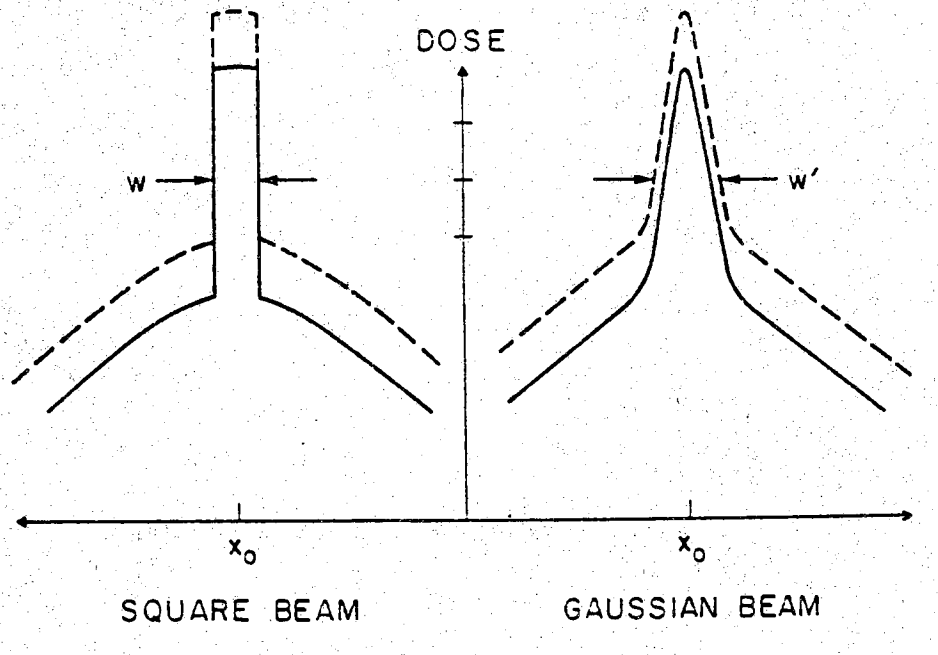

Figure 3.5. Square versus round beam (after ref. 58)

defined beam is clear. However, most commercial equipment, including the Cambridge EBMF2, and most custom built equipment have Gaussian beams.

3.8 Pattern Geometry and Proximity Effect

The total dose absorbed by a differential area of resist is a function not only of the dose given by direct exposure but also of the dose given to all areas surrounding the differential area from 2 to several tens of microns away depending on the beam energy. The proximity effect is due to backscattered electrons. There are two types of proximity effects, intra-feature and inter-feature. Figure 3.6 illustrates the two phenomena [38 p. 88]. When parts of two different features are close together, the total dose received in those areas will be larger than that received by the rest of the two features. The areas close together will be over exposed resulting in too wide linewidths or bulging boundaries. This result is the inter-feature proximity effect.

When a dose is sized to correctly expose the middle of a large feature, the corners of the feature and small features will be underexposed. The center of the large feature receives backscattered electrons from a large area in a full surrounding circle of several microns radius. The area contributing backscattered electrons to the corner of the feature is only 1/4 as large giving 1/4 the backscattered dose. An element of a fine line receives only a small fraction of the backscattered dose received by the element of a large feature. This phenomena is the intra-feature proximity effect. For correct exposure, small features, less than 1/2 μm wide, must be given doses from slightly larger to 20 times larger than those for large features [49].

3.9 Electron Beam Resist

Electron beam resists, like optical resists, can be divided into the two broad categories of positive and negative resists. All commercial resists and all resists used in this work are organic polymers. The electron beam causes scission of polymers in positive resist and crosslinking of polymers in negative resists. During development, the exposed areas of the positive resist and the unexposed areas of the negative resist dissolve.

The two parameters by which resists are characterized are contrast and sensitivity. Contrast is the important parameter for sub-micron experimental work since contrast determines resolution. Sensitivity is of concern to those in

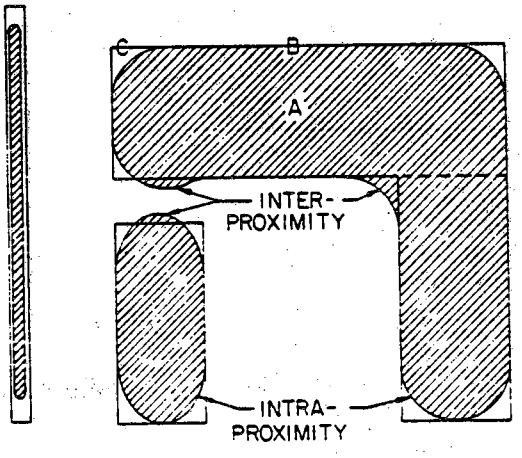

Figure 3.6. Proximity effect (after ref. 38)

commercial production since sensitivity determines throughput. The two parameters are defined and described below.

For a given set of development parameters such as a specific developer solution, a specific temperature, and a specific method of developing such as spray or immersion; a plot can be made for resists of normalized resist thickness after development versus exposed dose. See figure 3.7. The plots are always made with a log scale for dose and a linear scale for normalized thickness. Q_i is the dose at which scission or crosslinking begins and Q_o is the dose for complete exposure. Contrast is defined as the absolute value of the slope of the linear part of the graph. Contrast is generally signified by the variable γ. Mathematically,

$$\gamma = [\log_{10}(Q_o/Q_i)]^{-1}$$

An ideal resist would have a step response curve. For a positive resist, no resist would develop until a critical dose Q_i is reached, and then at that dose, all the resist would develop. This is ideal for the following reason. The energy absorbed by a resist as a function of the distance away from a single pass line scan can be modeled as two gaussian functions added together. Similar to the figure for the Gaussian beam in figure 2.5. The center distribution with the narrow variance is due to primary and secondary electrons and the distribution with the wide variance is due to the backscattered electrons. It is clear that the higher the contrast of the resist, the less it will be affected by backscattered electrons for a well chosen dose. Therefore, smaller linewidths are possible.

Sensitivity is determined by the lithographically useful dose. Often it is taken to be the dose at which half of the initial resist thickness is left after development. As the required dose decreases, the more sensitive is the resist considered to be. For a low dose, a high clock speed can be used thus decreasing the total exposure time and increasing throughput.

Poly methylmethacrylate (PMMA) has been the resist of choice for high resolution research work ever since its properties as an electron beam resist were discovered in 1968 [59]. It has the highest contrast, $\gamma \approx 3.8$, of all organic resists. PMMA is most often used in conjunction with a metal evaporation and lift-off process. Due to backscattering, the resist profile tends to be naturally undercut so no surface treatment is necessary as with optical resists. Metal gratings of 10 nm linewidth on 50 nm centers have been fabricated on bulk substrates (GaAs and Si) using 500 Å of PMMA and a 120 KeV square beam [58]. The 10 nm linewidth is thought to be the theoretical

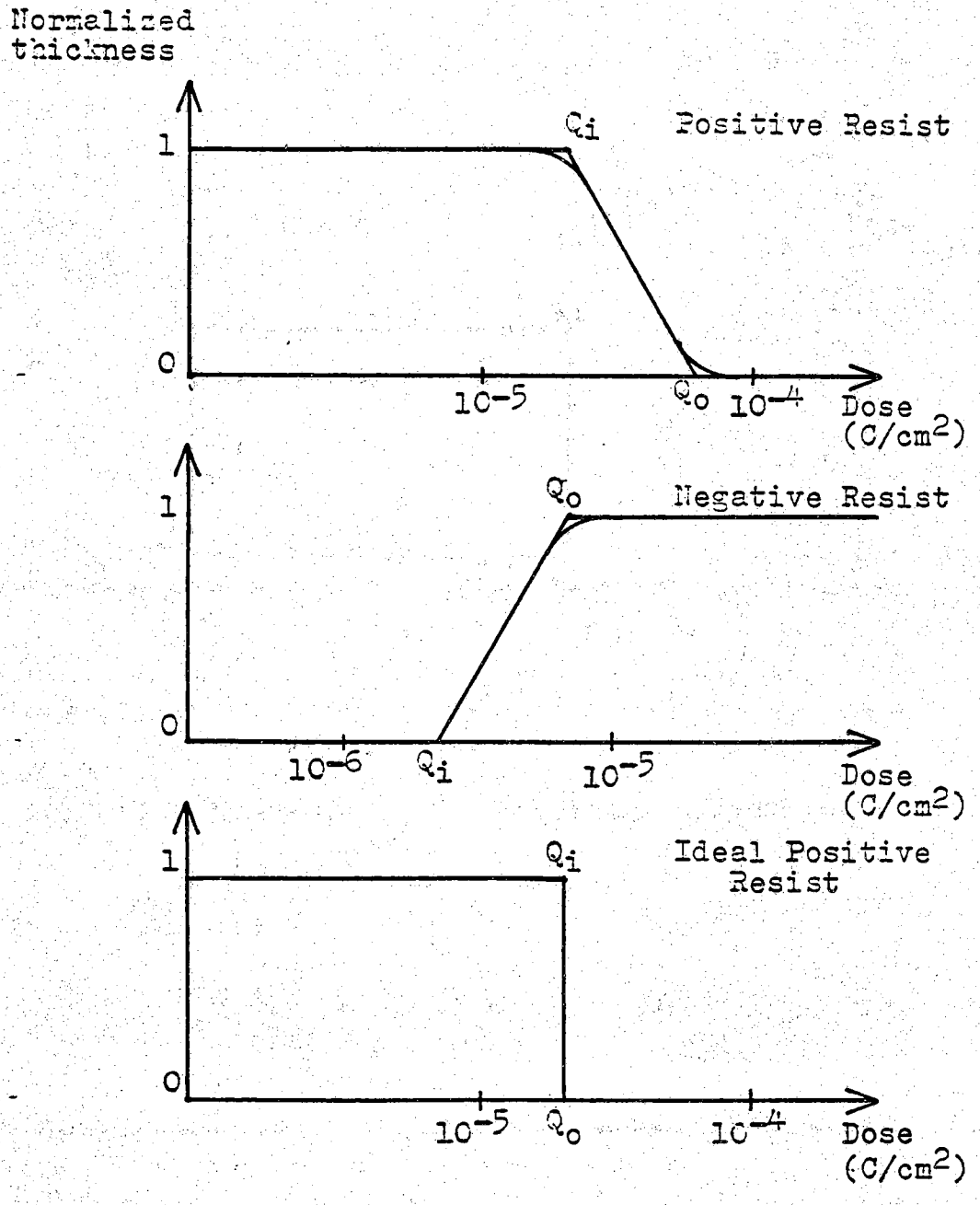

Figure 3.7. Plots of normalized resist thickness versus log dose

limit in PMMA imposed by secondary electron scattering.

Until 1987, there were no high contrast negative resists capable of submicron work. In 1987 the development of a novalak based high contrast, high sensitivity negative electron beam resist was announced [60]. The resist is distributed by Shipley under the name SAL 601-ER7. The novalak polymer is the base resin for most common optical positive resists such as AZ1350. In fact, developers for AZ1350 will also develop SAL 601-ER7. The contrast is between 3.44 and 3.77 [61]. The lithographically useful dose for a 30 KeV beam is between 12 and 20 $\mu C/cm^2$. Sub 100 nm lines have been defined in this resist [62], and ring structures of 0.3 μm linewidth have been defined easily and repeatably in this work.

3.10 Multi-level Resist

Multi-level resist schemes have been used to obtain enhanced resolution for the metal evaporation and liftoff process [49,63,50,51]. In general, a thin layer of PMMA is spun on top of a thicker layer of either more sensitive PMMA or non electron-sensitive polymer. The multi-level system increases resolution in two ways. The thick bottom layer acts as a low atomic weight substrate thus reducing backscattering to the upper layer and the upper layer, being thin, minimizes forward scattering.

An example of a bilayer system is 950K PMMA on 450K PMMA. The lower molecular weight resist is more sensitive than the higher weight resist and, upon development, provides an enhanced undercut.

Tri-level resists have also been used [50]. The 280 nm thick bottom layer is a copolymer, 90.8% methylmethacrylate : 9.2 % methacrylic acid dissolved in acetic acid. The abbreviation for the copolymer is P(MMA/MAA). 25 nm of Ge are then evaporated, and 100 nm of 950K PMMA is spun on top. Upon development, the image is formed only in the top layer of PMMA. The image is transferred to the Ge by a fluorine based reactive ion etch and then transferred to the P(MMA/MAA) by an oxygen reactive ion etch which also removes the top layer of PMMA. The oxygen etch attacks the copolymer with some degree of isotropy and thus provides an undercut necessary for liftoff.

3.11 Summary

The equipment used at Purdue is the Cambridge EBMF2. The electron optics are a typical commercial compromise between high resolution necessary

for submicron direct write applications and large deflection capability desirable for mask writing. The beam shape is Gaussian. On a similar machine, the minimum beam size measured by the manufacturer is 65 nm . The minimum linewidth reported by any of the users of Cambridge EBMF2s is 85 nm [62]. The minimum linewidth obtained here to date is 100 nm.

Both positive resist, PMMA, and negative resist, SAL 601-ER7, are used in submicron work. Multi-level resists have not been explored. In experiments to determine maximum resolution, a thin layer, 1000 - 2000 Å of high molecular weight, 950K, low concentration, 3%, PMMA is used. The contrast of SAL 601-ER7 is less than that of PMMA. This makes the proximity effect especially noticable when using SAL 601-ER7 to delineate intricate submicron features. Procedures used to compensate for the proximity effect will be explained in the next chapter. Details concerning graphics file preparation for the Cambridge EBMF2 and the driving software QSYS are contained in the appendices B, C, and D.

CHAPTER IV
FABRICATION

4.1 Introduction

A number of different devices were built: quantum resonators of different geometries, gated and ungated ring structures, and submicron Hall bridges. The fabrication process for all of the 1D novel devices and test structures is identical. The device that involves the most intricate submicron geometries is the the gated ring structure. It requires the highest resolution from the negative resist, SAL 601-ER7. For this reason, the gated ring structure will be used as an example and its fabrication will be described in detail. For a top view of the layout and cross section of the structure see figures 4.3, 4.4, and 4.6.

4.2 Fabrication Overview

The gated ring structure is fabricated in three levels on a high mobility, low carrier density GaAs-AlGaAs heterostructure, see figure 1.3. Level one contains the ohmic contacts and alignment marks for the following direct write levels. Masking is done optically with positive AZ1350-J resist. Ni-Au-Ge is evaporated from elemental sources in an electron-beam evaporator. The metal is patterned by lift-off and then annealed.

Device geometry is defined in the second level by a mesa etch. Masking is done by electron beam direct write. Negative electron beam resist is used, Shipley's SAL 601-ER7. A shallow wet etch, approximately 100 Å, defines the mesas and is sufficient for isolation.

The Schottky gates are defined in the third level. Masking is done by electron beam direct write. Positive resist is used, PMMA. Ti-Au is evaporated and patterned by lift-off.

4.3 Mask Layout

Mask layout can be very different for electron beam lithography as opposed to optical lithography. The difference is due to the proximity effect. Instead of a general discussion, the mask layout for this work will be described in detail.

The gated ring structure consists of three levels: ohmic contacts, mesas, and Schottky gates. The ohmic contact level contains no fine features. Therefore it is made into an optical mask. Both the mesa and gate levels contain submicron features and are therefore written with electron beam lithography. Furthermore, alignment with a tolerance of ± 0.2 μm is needed between the two levels. Metal, preferably gold, alignment marks are needed to align the last two levels with each other and with the ohmic contacts.

The alignment marks for electron beam lithography are round dots 6 μm in diameter placed on the ohmic contact level. Since metal alignment and focusing dots need to be on the wafer before any direct writing, the optical contact level is level 1, see figure 4.1. One alignment mark needs to be placed in each corner of the die. On this die, three are in each corner for redundancy in case of bad liftoff. The exact coordinates of the alignment marks must be recorded, preferably noted directly on the mask, for later use with QSYS, the Cambridge EBMF2 software.

The next level is the mesa level. It is directly written with SAL 601-ER7 negative electron beam resist. The features on this level range from large 200 x 200 μm squares to cover the contact pads during etching, to the smaller $\sim$ 5 μm wide connecting mesas, to the submicron width device. Due to the intra-feature proximity effect, the dose needed for the largest features can be 1/3 the dose for the smallest 0.3 μm features. Therefore, even though the entire mesa level is exposed in one writing session, the mesa level is divided into three different levels, levels 2 - 4, on the graphics file corresponding to the three different size groups, see figure 4.2.

For the submicron level, which consists of the test device, such as a ring, special precautions must be taken at all intersections to avoid flaring out due to the inter-feature proximity effect, see figure 3.3. At all intersections, the linewidth is reduced from the true linewidth, and a small section has been cut out of the ring at the ring - lead intersection. This is to counter balance the increased dose in those areas. A picture of the exposed resist after development is shown in figure 4.4. The ring is identical to the one shown in the graphics file. Notice the flare out at the lead - probe intersection. The

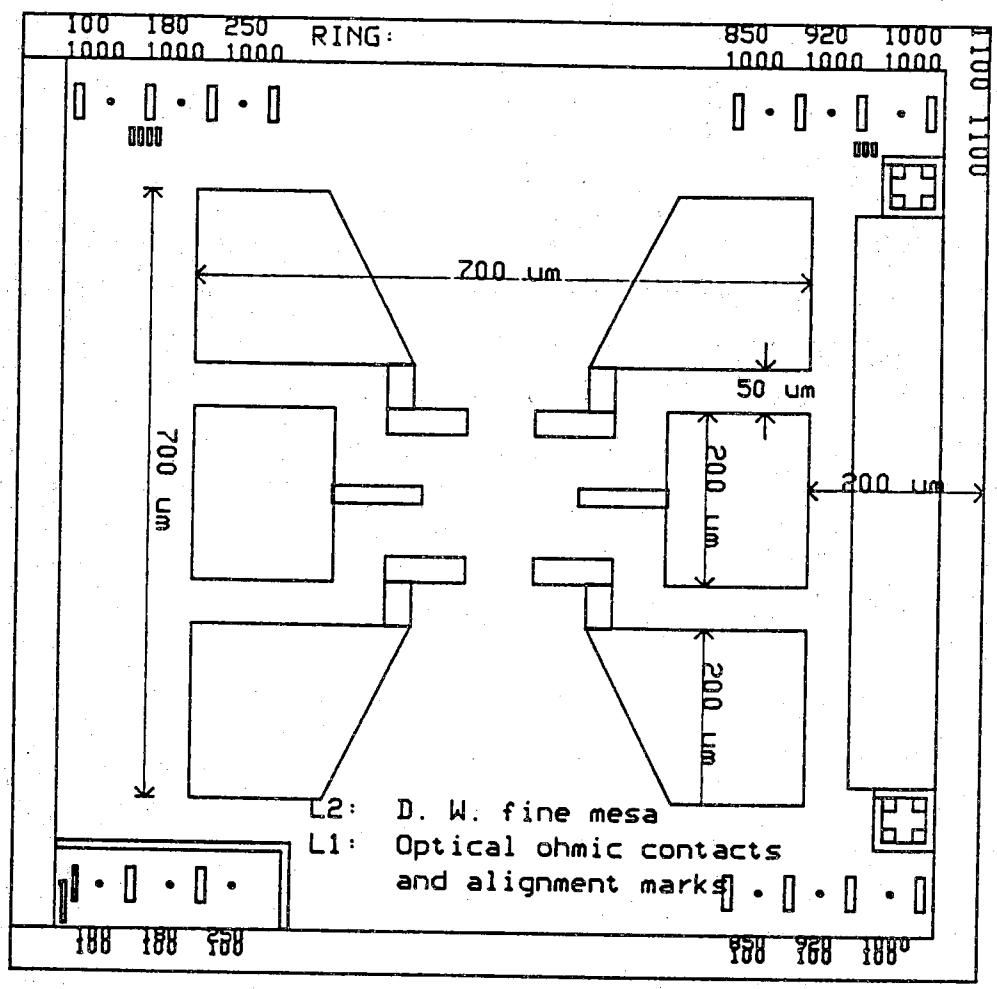

Figure 4.1. Level 1: Ohmic contacts and alignment dots

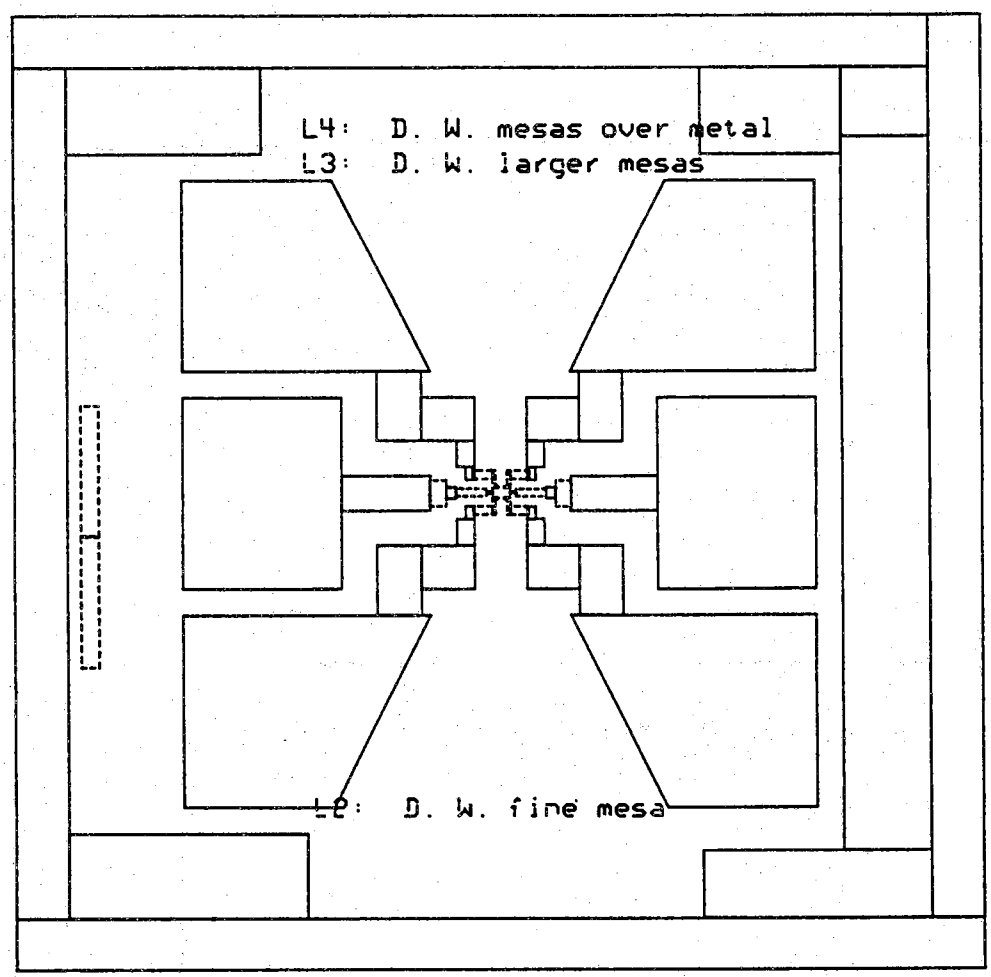

Figure 4.2. Level 2: Mesa level

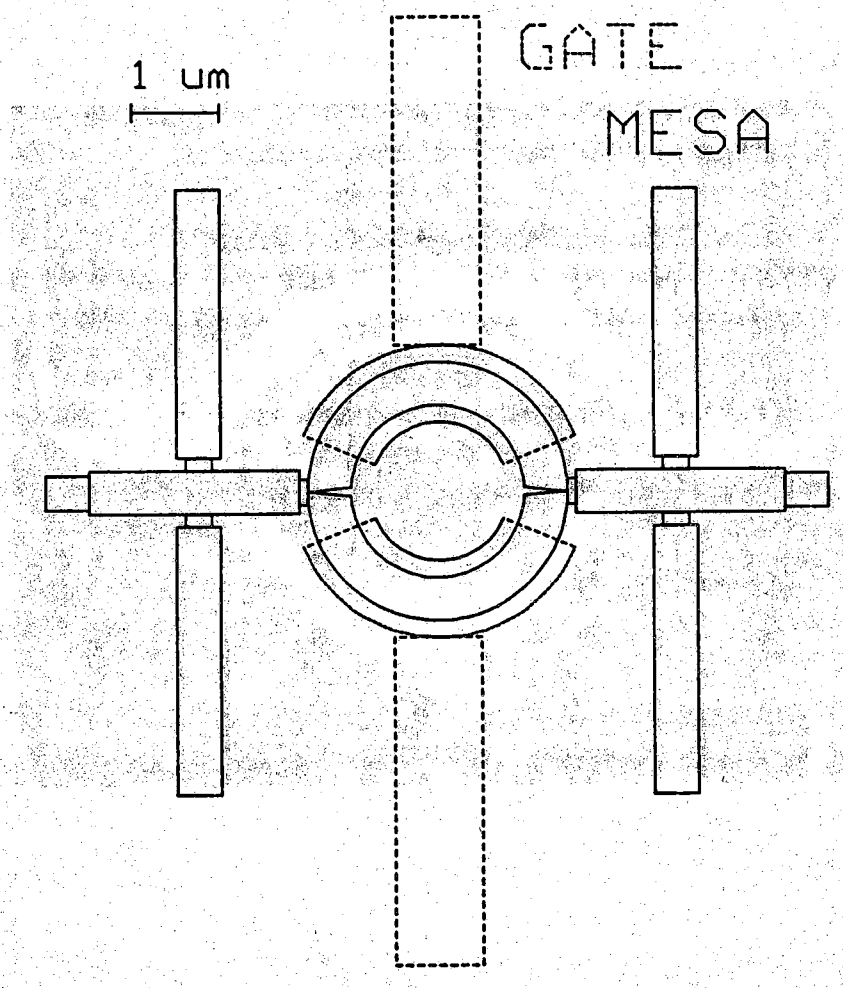

Figure 4.3. Submicron mesa level

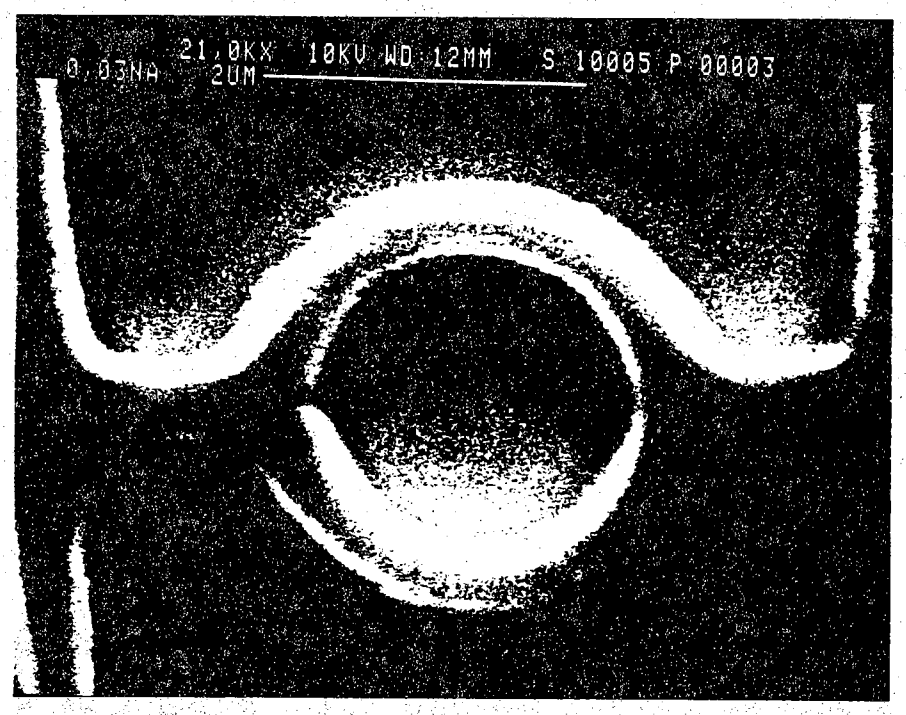

Figure 4.4. Developed resist corresponding to submicron mesa level

cutout in the graphics file has not completely compensated the overexposure due to the proximity effect. Also notice in figure 4.3 the sloppy intersection of the vertical and curved section of the gate. This is intentional to avoid overexposing and enlarging the intersecting area. However, the problem is much reduced when using PMMA since it is a higher contrast resist.

There is a temptation to widen current and voltage probe leads as quickly as possible to reduce series resistance and to reduce the possibility of an open circuit. One should not widen leads until at the very least 1 - 1 1/2 μm away from features of critical dimensions and then widen moderately for several more microns. Be aware of the level on which the widened lead will be exposed. If the 2 μm lead is exposed on the same level as the 0.3 μm device, it will receive a high relative dose and thus turn out larger than in the graphics pattern. In this work, the border linewidth between level 2 and level 3 is 1 1/2 to 2 μm.

The Schottky gate level is laid out in two levels on the graphics file. Level 6 contains the large bonding pads and level 5 contains the submicron gate and intermediate width connecting metal (see figure 4.5). Because of the high contrast of PMMA, there is little proximity effect. If the linewidth of the smallest metal features is $\geqq$ 1 μm, then they can be treated as large features and the gate level can be drawn on one level.

4.4 Film

The film is an Al_3Ga_7As - GaAs heterostructure with a cross section as shown in figure 1.3. The mobility should be as high as possible to maximize the mean free path. The carrier concentration should be as low as possible to keep phase-breaking electron electron scattering to a minimum and also ensure a single mode in the vertical direction. The structure used in this work has a mobility of $\sim$ 65 m^2/Vs at liquid helium temperatures and a carrier concentration of 2 - 3 x 10^{11} cm^{-2} depending on whether a 1D or 2D structure is measured.

4.5 Level 1: Ohmic Contacts and Electron Beam Alignment Marks

Level one is an optical level in which Ni-Au-Ge is evaporated in an electron beam evaporator from elemental sources and patterned by liftoff. After a dehydration bake, AZ1350 is spun at 4400 rpm for 40 seconds and then baked at 70° C for 10 minutes. The wafer is exposed in the Kasper contact aligner for two minutes and 20 seconds. The wafer is then soaked in

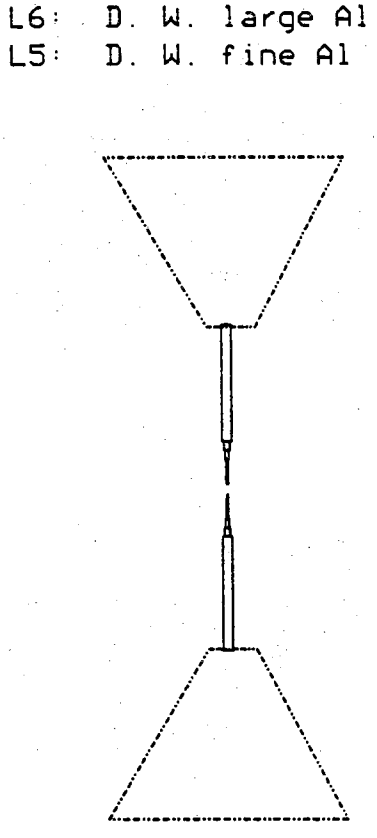

Figure 4.5. Schottky gate level

xylene for 3 - 5 minutes, dried with N_2 and developed in a 1:1 mixture of AZ developer and DI water. The development time is 30 seconds. Development should never be allowed to exceed 30 seconds or the hardened surface lip will begin to erode and lift off will be difficult. A 45 second DI rinse and N_2 dry finishes the development. Before evaporation, an oxide etch is performed by immersion in a mixture of 1 NH_4OH : 40 DI for 30 seconds followed by a DI rinse and N_2 dry. The sample is placed in the Varian electron beam evaporator and the pressure is pumped down to $\sim 10^{-7}$ torr. The metal layers are then evaporated in the following order and thickness: 50 Å Ni, 1500 Å Ge, 3000 Å Au, and 850 Å Ni. The ratio of Ge to Au is an eutectic mix. The total thickness is sufficient after annealing for ultra-sonic bonding. After evaporation, the system is allowed to cool for 10 minutes before pressurizing to avoid oxidation.

The next step is lift off. The wafer is placed in a beaker of acetone and allowed to soak for 30 minutes. The beaker is then agitated by hand. If the lithography is very good, the unwanted metal will lift off by this gentle agitation. The next more violent approach is to squirt acetone at the wafer submerged under about one centimeter of acetone. If there is still unwanted metal, squirt directly at the wafer. When all else fails, place the sample in acetone in a glass beaker in the ultrasonic cleaner for one to two minutes. Plastic beakers absorb much of the vibration and will not do the job if the unwanted metal is very obstinate. The lift off is finished with a DI rinse and N_2 dry.

Immediately after lift-off, the contacts are annealed in the Marshall oven for 5 minutes at 450° C. After annealing, the contacts should appear rough and brownish although an occasional contact becomes silvery. The contact resistance remains linear at liquid He temperatures. No attempt has been made to measure the specific contact resistance. For a cross section of levels 1 - 3, see figure 4.6.

4.6 Level 2: Mesa Level

Device Geometry is defined in level 2 by an isolation etch. Masking proceeds as follows. After a dehydration bake, negative electron beam resist, SAL 601-ER7, is spun at 6000 rpm for 40 seconds followed by a softbake at 85° C for 30 minutes. For a spin speed curve, see figure 4.7. Contrast is not a strong function of the time and temperature of the softbake. They are not critical parameters.

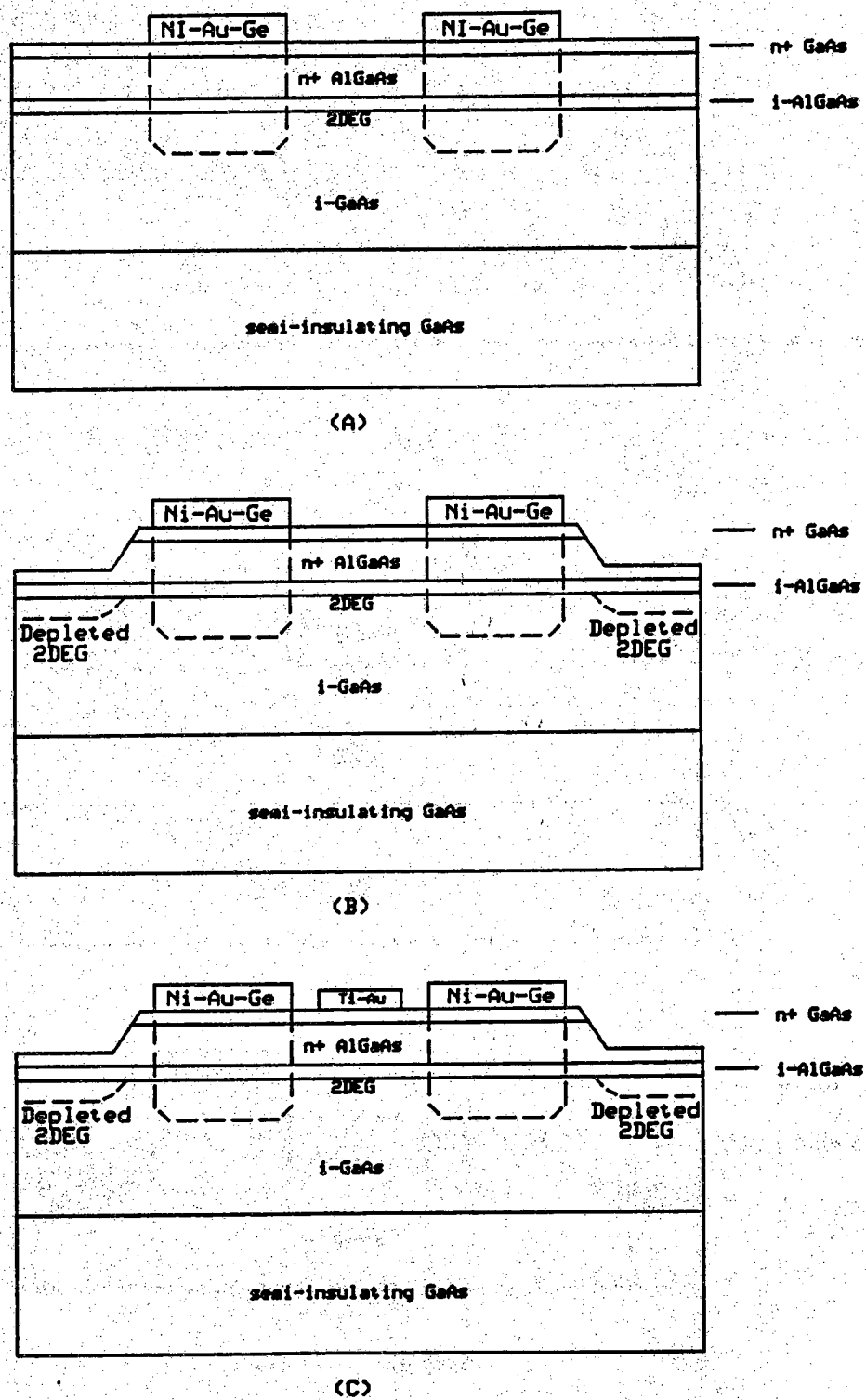

Figure 4.6. Cross sections: A) Level 1 B) Level 2 C) Level 3.

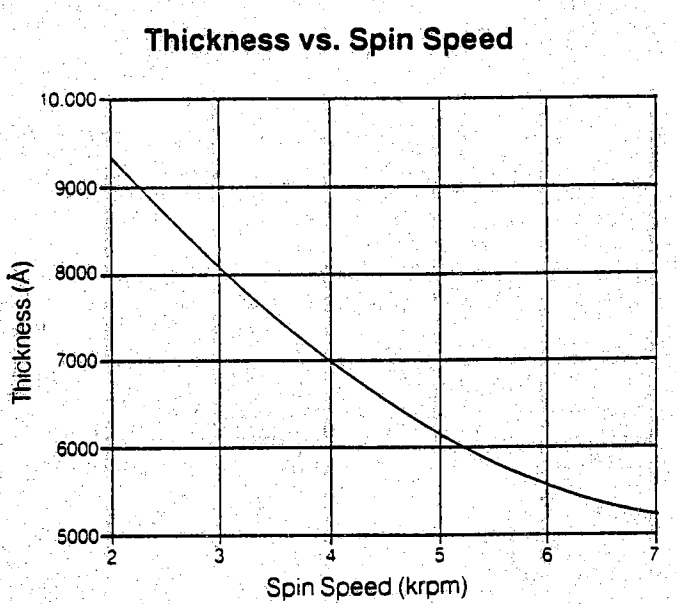

Figure 4.7. Spin speed curve for SAL 601-ER7 (after ref. 61)

The sample is then exposed in the Cambridge EBMF2. At an energy of 20 KeV, table 4.1 gives the appropriate doses for a given linewidth.

Table 4.1. Exposure doses at 20 KeV

Linewidth (μm)	0.5	0.3	0.2	Large Pads
Dose ($\mu C/cm^2$)	10	14	14	5

A 0.4 μm linewidth can be obtained by exposing a 0.3 μm line at 16 $\mu C/cm^2$. Similarly, 0.6 μm linewidths are obtained by overexposing 0.5 μm lines at 12 $\mu C/cm^2$. If one wishes to build a set of devices with a range of linewidths, one only need lay out a device for every other linewidth, say 0.1, 0.3, and 0.5 μm, and the intermediate sizes are obtained by changing the exposure dose. At 30 KeV, the backscattered electrons will be more spread out, having a lower concentration contributing less to the dose. Therefore, a higher calculated dose will be needed. The experimentally found dose to correctly expose a 0.3 μm line at 30 KeV is 20 $\mu C/cm^2$. Other linewidths have not been written at 30 KeV.

During a writing session, one needs to translate the dose figures into beam current and clockspeed. A small current is desired to minimize the spot size. For sub-micron work, the smallest aperture, number one, is used to obtain the smallest beam current for which registration is possible. This current is $\sim$ 0.1 nA. It is the current used for all of the submicron writing in this work. The intermediate sized lines, of several microns width, are also exposed at this current but at a higher clock speed. For the large pads, aperture 2 or 3 is used with a current of 10 - 20 nA.

Knowing the beam current, one can calculate the clockspeed for a given dose by the following equation,

$$f = \frac{I \times 2^{2n} \times 100}{S \times F^2}$$

where I is current in amps, n is the number of bits in the field (15 unless VRU is used), S is the dose in Coulombs/cm^2, F is the field size in millimeters, and f is the clockspeed in Hz.

4.7 Post Exposure Bake

A post exposure bake is critical for the success of the lithography. If it is omitted, all of the resist, both exposed and unexposed, will dissolve in the developer. It is suggested that a hot plate with a vacuum chuck controlled to within $\pm 1^{\circ}$ C be used [61]. Since that is not available, a convection oven is used. The temperature and time of bake are 105° C and 4.5 minutes. An inverted petri dish is placed in the oven and stabilized at 105° C well before the time of the bake. The sample is placed directly on the petri dish for the bake.

4.8 Development

Two developers are made by Shipley for SAL 601-ER7. They are Microposit SAL MF622 and SAL 660. SAL MF622 is metal ion free and gives the highest contrast of 3.75. SAL 660 is not metal ion free and has a lower contrast of 3.41 [61]. SAL 660 is used in this work and is adequate for the geometries needed. The developer is used undiluted, and developing time is 10 min. The developer is rinsed by leaving the sample in a beaker under running de-ionized water for at least 5 minutes. The developer is found to attack and expose oval defects. It is not known whether there is any effect on the GaAs. For this reason, development is never allowed to proceed longer than 10 minutes.

4.9 Isolation Etch

A wet etch is used. It is a ratio of 3 NH_4OH : 1 H_2O_2 : 1000 DI. The measured etch rate is 430 Å / 90 s. The initial etching is done in five second intervals. After five seconds of etching, the sample is rinsed, dried, and tested at the probe station for isolation between non-connected contacts and continuity of the devices. Isolation is tested between the widened section of the die perimeter and an adjacent contact (see figure 3.1). The contacts are probed through the resist. Probing is done at room temperature both in the light and in the dark. Isolation will first occur in the dark and then, after five to seven more seconds of etching, in the light. There is generally little change in resistance until after the third five second etch when the resistance increases dramatically. After one to two more five second etches, isolation will be almost complete in the light. At that point, the etch periods are reduced to two seconds, and after one to three two second etches, isolation is complete.

In the first run etching was stopped after isolation occurred in the dark. Good results were obtained at liquid He temperatures but the devices were tempermental. Current through the device had to be turned on at room temperature and kept on during the cooling and testing. If the current was at any time interrupted, the device would open circuit. For the second run, an LED was placed in the helium dewar. When the LED was flashed on, it was found that if isolation was only good in the dark, persistent photo-conductivity would cause all isolation to cease. For the third run, etching was continued until isolation occured in the light and good results were obtained when testing in the light. The total etch time for isolation in the light is 28 seconds. The total etch depth is not known. Dilute etchants generally do not have a constant etch rate.

4.10 Level 3: Schottky Gates

In level three, the pattern for the Schottky gates is defined in PMMA by electron beam direct write. After a dehydration bake, 4% 950K PMMA is spun on the wafer at 5000 rpm for 30 seconds. The measured thickness ranges from 2000 - 3000 Å. The wafer is then baked at 160° C for 4 hours to remove all traces of the solvent. The PMMA is exposed in the Cambridge EBMF2 at an energy of 30 KeV. A dose of 320 $\mu C/cm^2$ is used for features between 0.3 and 1.0 μm. A dose of 300 $\mu C/cm^2$ is used for larger features. These same doses also provide good results at 20 KeV. The proximity effect is not nearly as much of a problem with PMMA as with SAL 601-ER7. The developer system is 3 Cellosolve : 7 methanol. The exposed wafer is immersed in the developer for 5 - 10 seconds and then rinsed by immersion in methanol for 30 seconds. No surface treatment is needed since the resist profile is naturally undercut due to backscattering. The wafer is then dried with N_2 and inspected. An oxide etch is done prior to evaporation to improve adhesion. The metal layers are evaporated in the following order and thickness: 200 Å Ti and 800 Å Au. Liftoff is performed identically as before.

Gate widths of 0.5 and 0.3 μm have $\sim$ 100% yield. The smallest gate width attempted and successfully lifted off is 0.1 μm. An unsuccessful experiment was done to determine the minimum linewidth possible. A single pass line was coded and exposed at 30 KeV with calculated doses ranging from 300 $\mu C/cm^2$ to 1 mC/cm^2. After development, no trace of a line was found. It is felt that insufficient dose was used. With a single pass line, there is no contribution to the net dose from nearby exposed areas. For a single pass line a dose of up to 20 times that for a large feature may be necessary. The

minimum size feature reported by users of another Cambridge EBMF2 is 80 nm [64].

Level to level alignment is achieved by the QSYS software. See appendix four for details. The maximum error is $\sim$ 0.25 μm. Generally, approximately 70 - 80 % of the time, the error is $\leqq$ 0.1 μm.

4.11 Other Fabrication Methods of Submicron Conducting Channels

Most fabrication methods follow the procedure of masking and etching. The differences lie in particular masking and etching processes. The method that gives the highest resolution is to define the pattern in PMMA, electron beam evaporate an insulator or metal, and lift off [1,2,6,10,11]. Thus the metal or insulator provides the etch mask. The use of an insulator is preferable to a metal. When using a metal mask, the metal must eventually be removed or special precautions must be taken so that the metal does not short out the device.

In developing the fabrication process, this was the first method explored in this work. Two different mask materials and deposition processes were investigated. The first material was aluminum evaporated in the NRC thermal evaporator. It was desired to build a gated ring structure where the two arms of the ring could be placed at different potentials. The aluminum, being an equi-potential surface, needed to be either removed or changed into an insulator. From other work at Purdue, it was known that by boiling a thin film (1000Å) of Al in DI water, the film could be changed into a hydrate of Al_2O_3, an insulator. This procedure was successfully used to define an insulating ring mask on bulk GaAs (see fig. 4.8). It is not known whether the raggedness of the ring pattern is due to lift off or insufficient points defining the ring pattern in the graphics file. At that time, only $\sim$ 50 were used. Now $\sim$ 100 are used.

The second material was SiO_2 sputtered on in the ion mill. Ring masks of 0.3 μm linewidths and 1.0 μm inner diameter were successfully fabricated (see fig. 4.9). Here the lines are ragged from the lift off process. There are two problems with this process. The sputtered flux is not perpendicular to the sample. Thus, the resist sidewalls become coated and lift off is difficult. The use of the ultra-sonic cleaner is always necessary to finish the lift off. Secondly, the deposition process may cause surface damage as deep as the 2DEG and thus reduce the mobility. A preliminary experiment seemed to support this hypothesis.

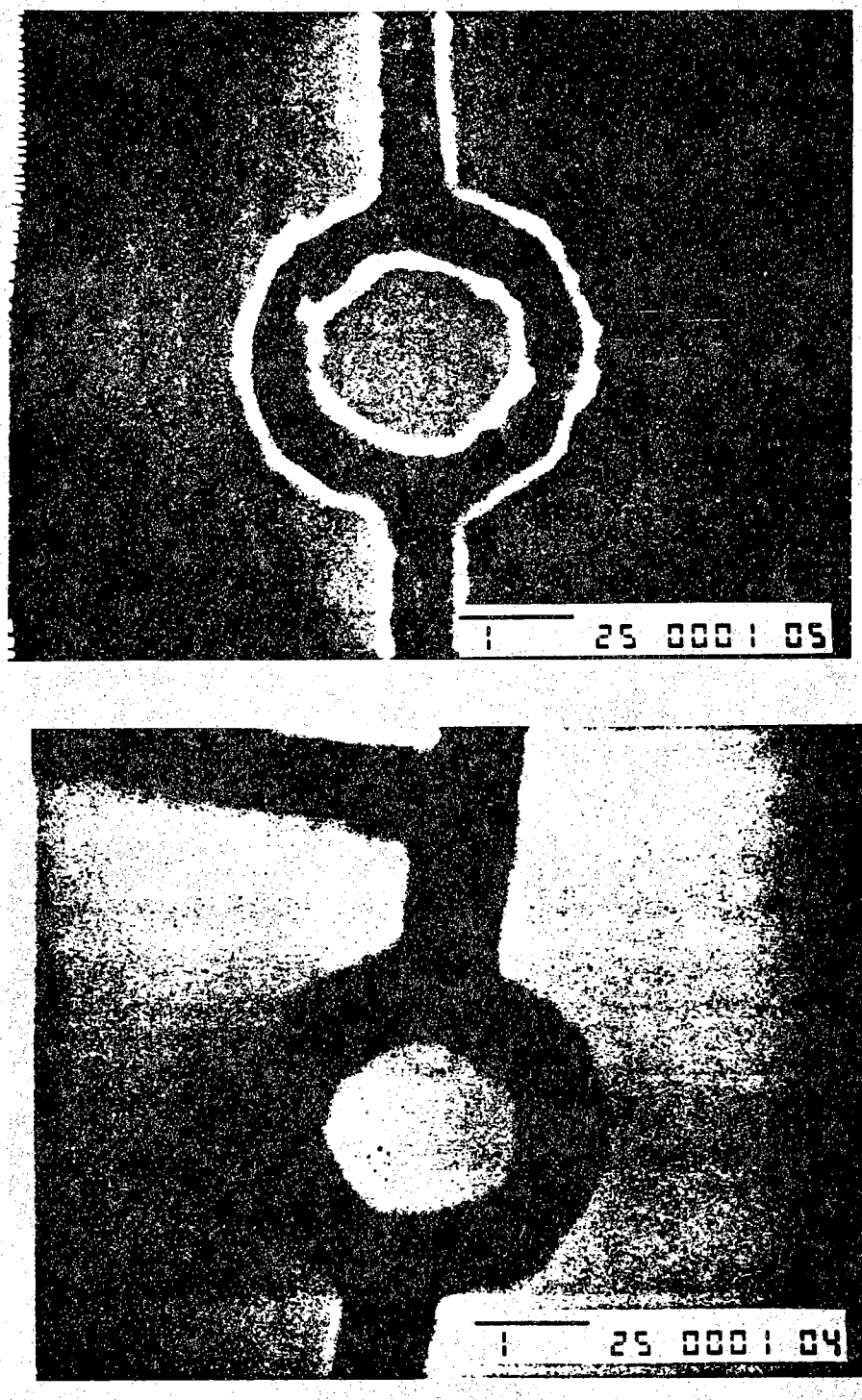

Figure 4.8. Al mask, A) Before boiling B) After boiling

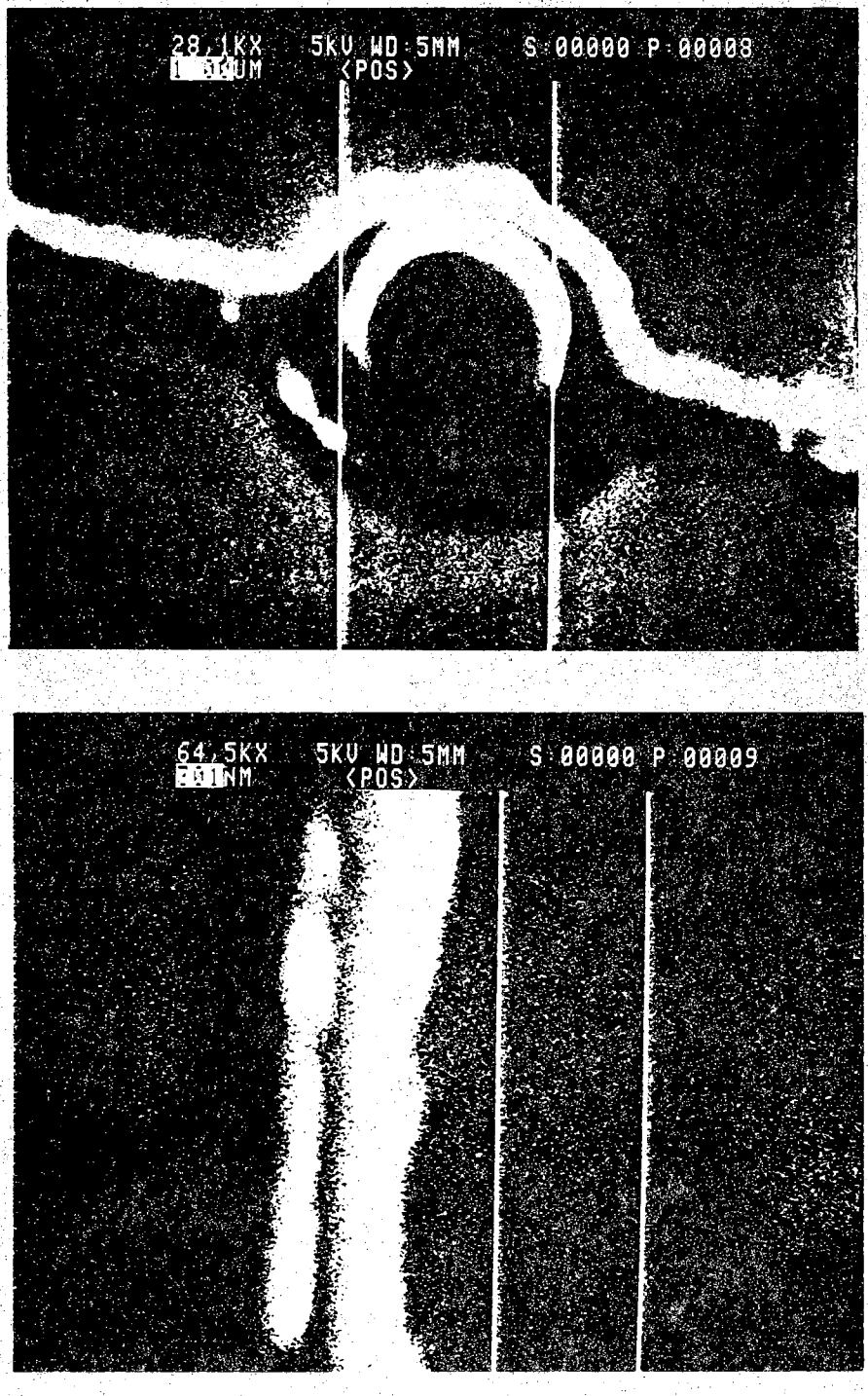

Figure 4.9. SiO_2 mask, 0.3 μm linewidth

Dry etching gives the most reliable and repeatable fabrication process. It has been used to achieve the most notable results in one dimensional transport in GaAs - AlGaAs heterostructures [1,2,11]. Timp, Chang et. al. use a low voltage (75 - 150 V) reactive ion etch (RIE) [1]. An etch stop layer built in the AlGaAs during film growth stops the etch at a pre-determined depth giving highly reproducible results. Electrical isolation is due to edge depletion not the physical mesa boundary. The minimum width conducting channel built by this method is 450 nm.

The smallest physical width conducting channels have been achieved by the use of ion beam assisted etching (IBAE) with Ar ions in the prescence of Cl_2 gas [4]. A 150 ev ion beam is directed at the sample with Cl_2 introduced near the surface. Only the n^+ cap layer is physically removed by the etch. Isolation is due to electrical damage caused by the ion milling. Mesas of physical width 75 nm conduct. Furthermore, the resistance roughly scales linearly with size among a set of Hall bridges ranging in linewidth from 75 nm to 1.1 μm [2]. It is believed that even smaller conducting channels can be fabricated by this method. For comparison, the smallest conducting channels fabricated by a wet etch in this work are 0.3 μm. Other workers have achieved $\sim$ 0.1μm [9].

A completely different approach is to use Schottky gates to build a device of variable linewidth. This has been used extensively to build a simple two terminal variable width resistor [23]. It has also been used to build a variable width ring structure [15].

CHAPTER V
CHARACTERIZATION OF DEVICE AND MATERIAL PARAMETERS

5.1 Introduction

The two dimensional mobility and sheet carrier concentration are determined from classical Hall measurements and Shubnikov-deHaas oscillations. A magneto-resistance anomaly observed in large Hall bridges is described. The electrical linewidth and phase breaking length for a conducting channel of physical width 0.3 μm is determined from Aharonov-Bohm oscillations.

5.2 Two Dimensional Mobility and Sheet Carrier Concentration

Both Hall bridges and a Van der Pauw pattern are tested for the classical Hall effect and Shubnikov-deHaas oscillations. The initial Hall bridge has dimensions as shown in figure 5.1. Subsequently, Hall bridges were fabricated with all dimensions scaled up by a factor of two and a factor of four. The values for the sheet resistance, sheet carrier concentration, and mobility derived from classical Hall measurements are shown in table 5.1.

Table 5.1. Mobility and carrier concentration from classical Hall measurements.

	Hall Bridge			Van der Pauw
T (K)	300	~100	4.2	4.2
R_s ($\Omega/\square$)	1745	524	28.9	25.2
n_s (cm^{-2})($1/r_H$) x 10^{11}	4.88	3.21	3.28	3.96
μ_H (m^2/Vs)	0.734	3.72	65.8	62.7

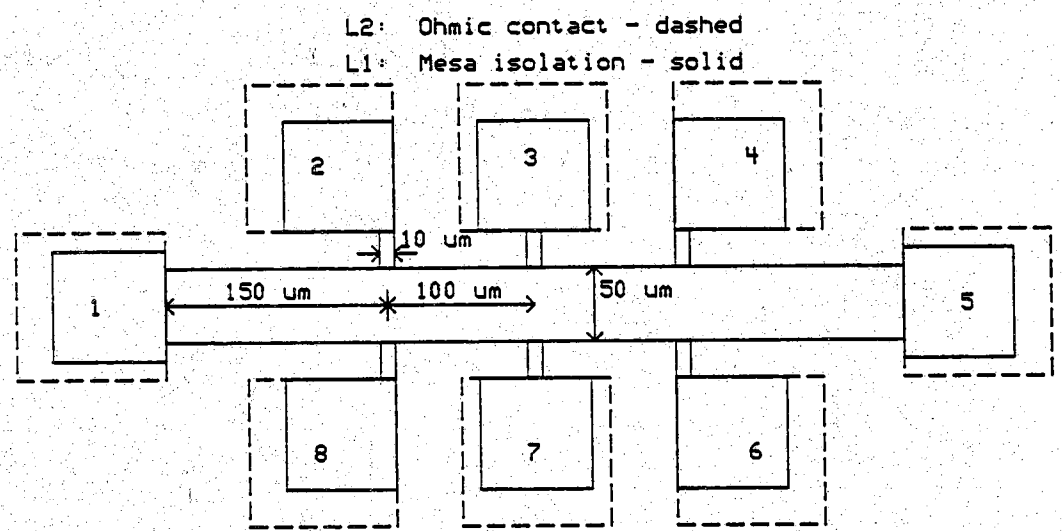

Figure 5.1. Hall bridge used for 2D measurements.

The Van der Pauw pattern is simply a square piece of film approximately three millimeters on an edge with contacts on the four corners. Since the film is unpatterned, some unquantified error is present in the measurements.

The high field value of the carrier concentration is found from the Shubnikov-deHaas oscillations in a plot of R_{xx} versus B (see figure 5.2). The peaks (or troughs) of the oscillations are given integer values starting at the right and ascending to the left. The integer values are then plotted versus 1/B. The plot should be linear since the oscillations are periodic in 1/B with period, $\Delta(1/B)$, given by the inverse slope (see figure 5.3). The sheet carrier concentration is found from equation 2.13,

$$n_s = \frac{2e}{h\Delta(1/B)}$$

The values of sheet carrier concentration and mobility calculated from Shubnikov-deHaas data are shown in table 5.2.

Table 5.2. Mobility and carrier concentration from Shubnikov-deHaas measurements

T (K)	4.2	1.3
R_s ($\Omega/\square$)	27.6	27.7
n_s (cm^{-2})(x10^{11})	3.04	3.02
μ (m^2/Vs)	74.4	74.6

The SdH data is from a different Hall bridge than the classical Hall data, however the bridge dimensions are identical. As an aside, assuming that there is not a large non-uniformity across the film, the data indicate that the Hall correction factor for the degenerate two dimensional case is slightly less than unity.

5.3 Magneto-Resistance Anomaly

An anomaly in magneto-resistance is seen in both plots of R_{xx} and R_{xy} versus magnetic field. A typical sweep is shown in figure 5.4. The sharp change in the characteristic, referred to as the "glitch", occurs at a different field depending on whether the voltage is probed on the right or left side of

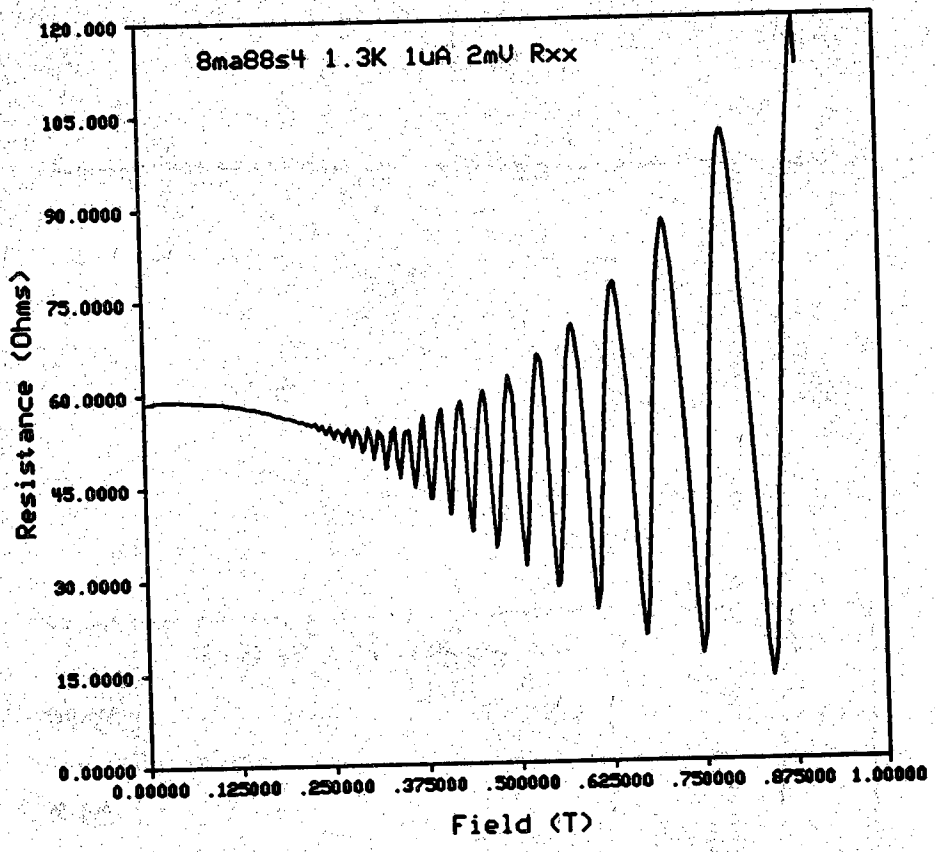

Figure 5.2. Shubnikov-deHaas oscillations from 2D Hall bridge

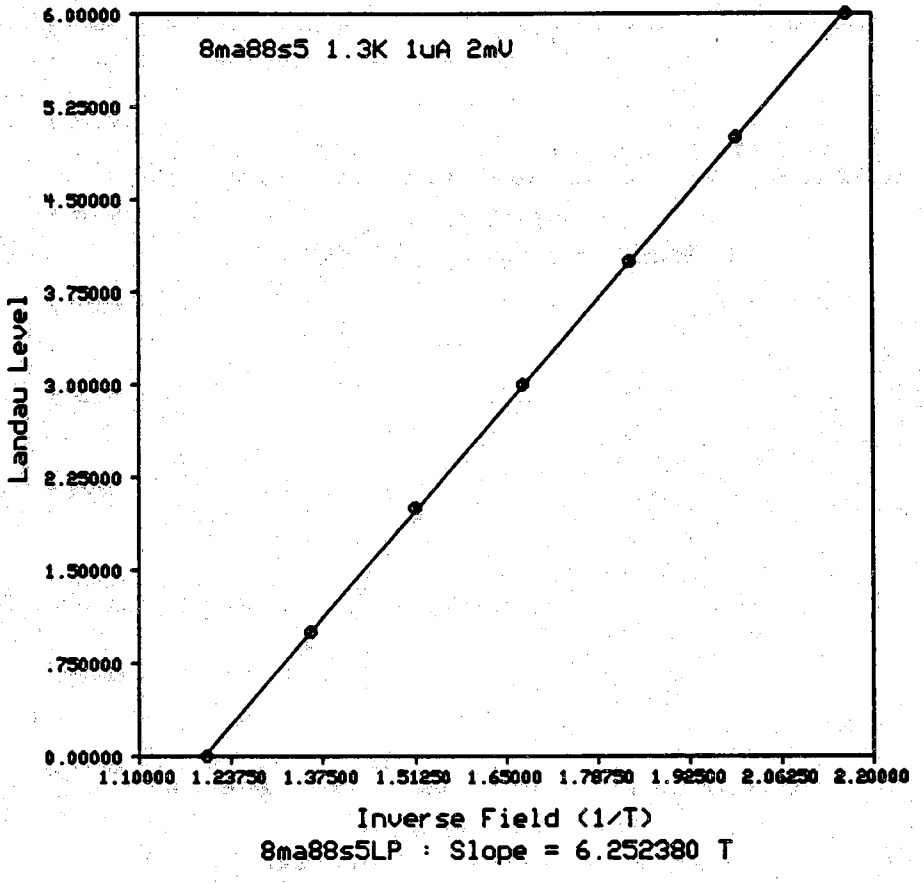

Figure 5.3. Landau plot from 2D Hall bridge

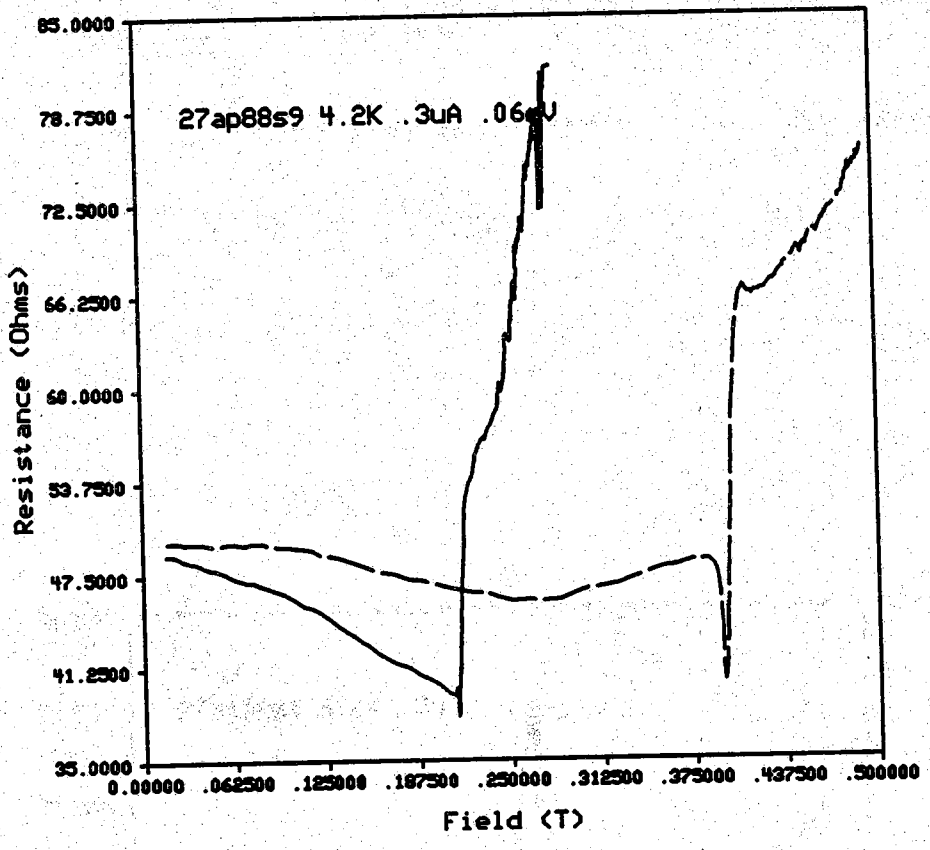

Figure 5.4. Magneto-resistance anomaly

the Hall bridge. If the field is reversed, the characteristic of the right and left sides are reversed.

In the large square Van der Pauw pattern, there is no sign of the glitch for fields up to 1.5 T. In the Hall bridges, the glitch can be postponed by forcing current through leads other than one and five (see figure 5.1 for lead numbers). In figure 5.2, current is forced through leads one and six and voltage is measured across probes two and three. The glitch occurs at $\sim$ 1 T. The most interesting results are obtained when the Hall bridge is tested as if it were a Van der Pauw pattern. Current is forced through leads eight and seven, and voltage is measured across leads two and three. If the fact that the test current is alternating at 17 Hz is neglected, then there is no glitch for fields up to 1.5 T when the curvature of the current path corresponds to the direction of the Lorentz force. When the field is reversed, the glitch occurs at $\sim$ 1 KG (see figure 5.5). Furthermore, two terminal measurements give the same results (see figure 5.6).

The two terminal measurements show a large positive magneto resistance. In figure 5.6, the resistance increases from 200 Ω to 3500 Ω during a sweep from 0 to 1.5 T. In the corresponding four terminal measurement (figure 5.5), the increase in resistance corresponding to a line drawn through the center of the SdH oscillations is $\sim$ 30 Ω. The positive magneto-resistance is not a result of geometry since a two terminal measurement along a straight line between leads one and five gives an increase in resistance of $\sim$ 2.6 KΩ over 1.5 T. One explanation is that there is a large positive magneto resistance assosciated with the alloyed Ni-Au-Ge contact system. The time-dependent noise seen after the occurrence of the glitch indicates a phase shift or time-dependent magnitude fluctuation. There is no good hypothesis for either phenomenon.

5.4 One Dimensional Structures

Ring structures of 0.3 μm physical linewidth are tested. Aharanov-Bohm oscillations are observed and the results are used to make estimates of the phase breaking length and the electrical linewidth. All Aharanov-Bohm data is taken at a temperature of 1.3K. Oscillations were not observable at 4.2K.

A typical sweep of R_{xx} versus magnetic field is shown in figure 5.7. Two differences between figure 5.7, from a narrow structure, and figure 5.2 from a wide structure are universal conductance fluctuations and the large negative magneto resistance. Aharanov- Bohm oscillations cannot be seen on the scale

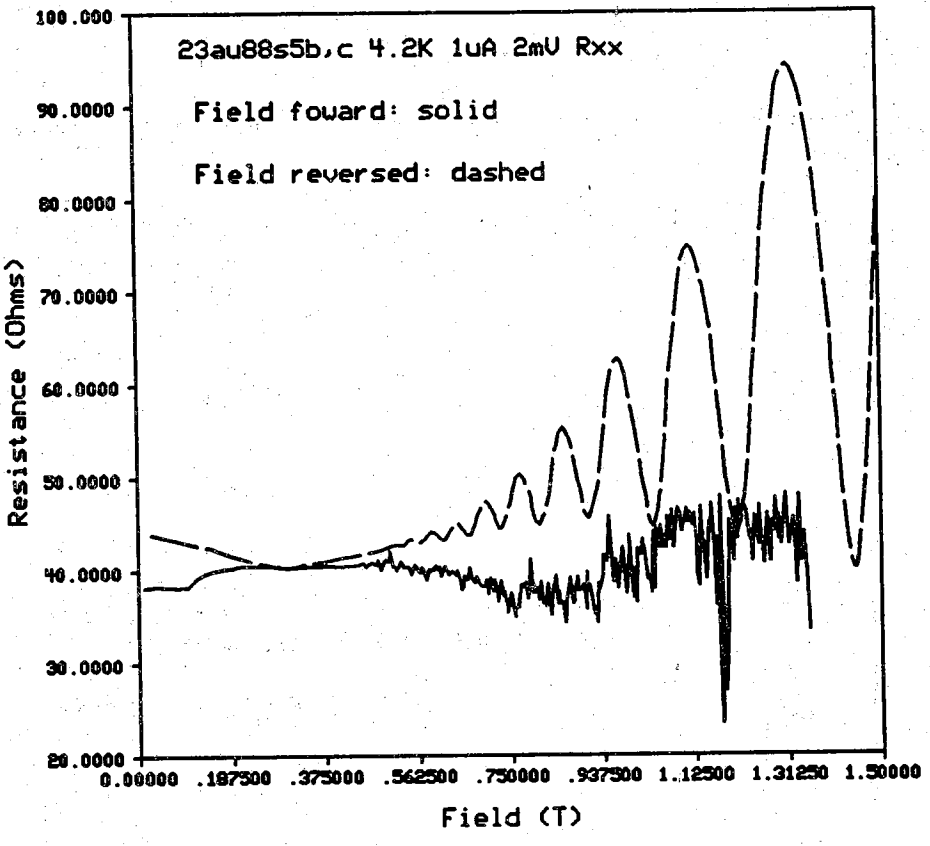

Figure 5.5. $R_{23,87}$: field reversed and field forward.

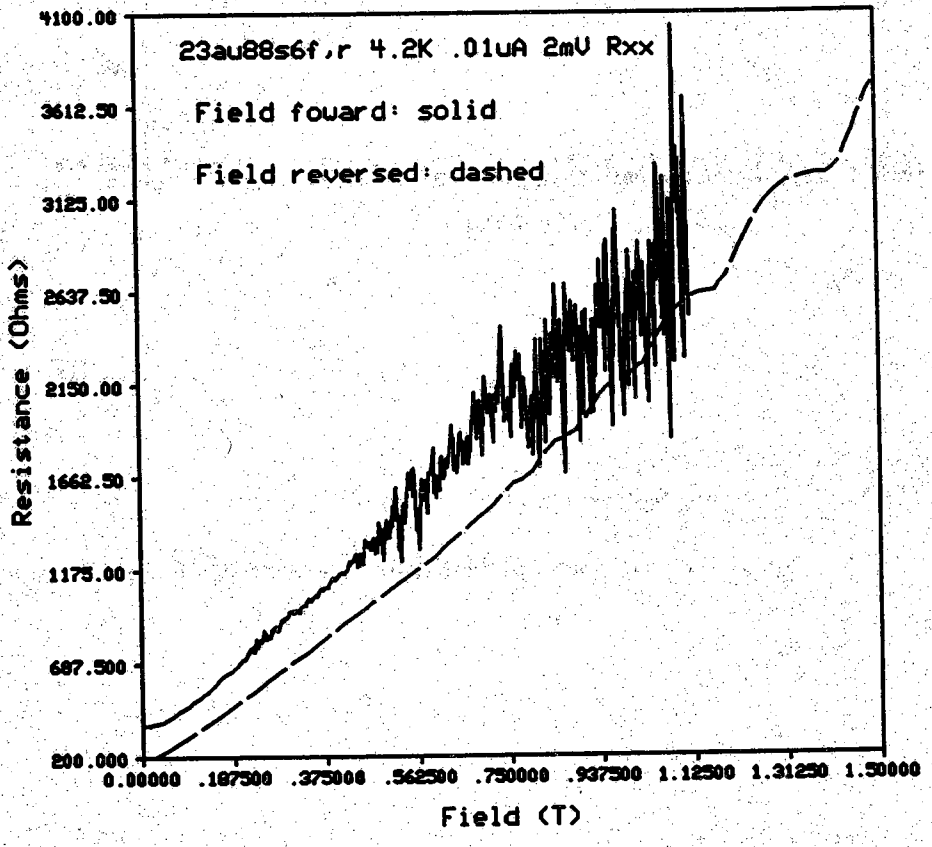

Figure 5.6. R_{23}: field reversed and field forward.

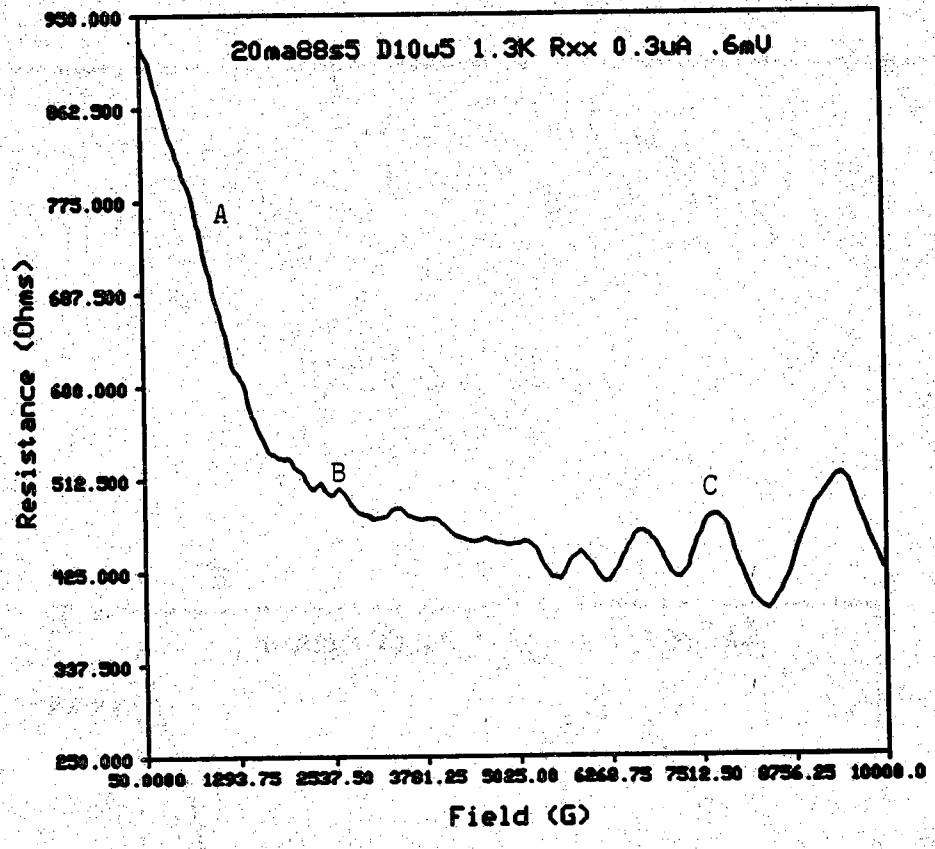

Figure 5.7. R_{xx} versus magnetic field. (A) Negative magneto resistance, (B) Universal conductance fluctuations, (C) SdH

of the graph.

Aharanov Bohm oscillations from a ring structure of nominal linewidth 0.3 μm and inner radius 0.5 μm are shown in figure 5.8. The actual data is inverted so that it is in terms of conductance and the fitted polynomial used to subtract off the background is shown. Figure 5.9 shows the fluctuations minus the background, and figure 5.10 shows a Fourier power transform of the fluctuations. The center of the fundamental frequency occurs at 328 (1/T) corresponding to a mean radius of 0.657 μm. The nominal mean radius is 0.65 μm. The actual mean radius is also $\sim$ 0.65 μm. An SEM micrograph of the ring is shown in figure 5.11. The dirt on the surface appeared during or after one of the several immersions in liquid He. Looking closely, one can see that the inner and outer diameters are $\sim$ 1.0 and 1.6 μm respectively. The nominal dimensions of the ring are shown in figure 5.12.

The electrical linewidth can be determined from the width of the fundamental frequency. Choosing the two nulls at the bottom of the fundamental frequency gives an inside radius of 0.622 μm, an outside radius of 0.740 μm, and an electrical linewidth of 0.118 μm. Hall measurements from a slightly wider structure, nominally 0.5 μm, give a carrier density of 2.6 x 10^{11} cm^{-2} at 500 G. A lower carrier density from the 2D value is expected (see section 2.9). A particle-in-the-box approximation of the boundary potential indicates 4 full subbands and a partially populated fifth subband for a width of 0.118 μm (see table 2.1).

It has been observed by others that suppression of the Aharanov-Bohm oscillations occur at $\sqrt{\hbar}/eB \sim W_e/2$ (see section 2.4). Here, the oscillations are suppressed at $\sim$ 500 G giving an alternate estimate for W_e of 0.23 μm.

5.5 Estimation of Phase Breaking Length, L_ϕ

Ring structures provide two estimates of the phase breaking length. Both estimates are based on equation 2.5. For the first estimate, the rms amplitude of the conductance fluctuations, ΔG, is used. For $L_\phi = \pi r$, one assumes $\Delta G = 0.4e^2/h$, and that for $L_\phi < \pi r$, $\Delta G = 0.4\frac{e^2}{h}\exp(-(\pi r - L_\phi)/L_\phi)$ where r is the mean radius of the ring. Therefore,

$$L_\phi = \pi r / \ln\left(\frac{1.09e^2}{h\Delta G}\right) \qquad (5.1)$$

For the data shown in figure 5.8, $\Delta G = 0.0035e^2/h$. Before this value is used, the effect of lead resistance must be considered.

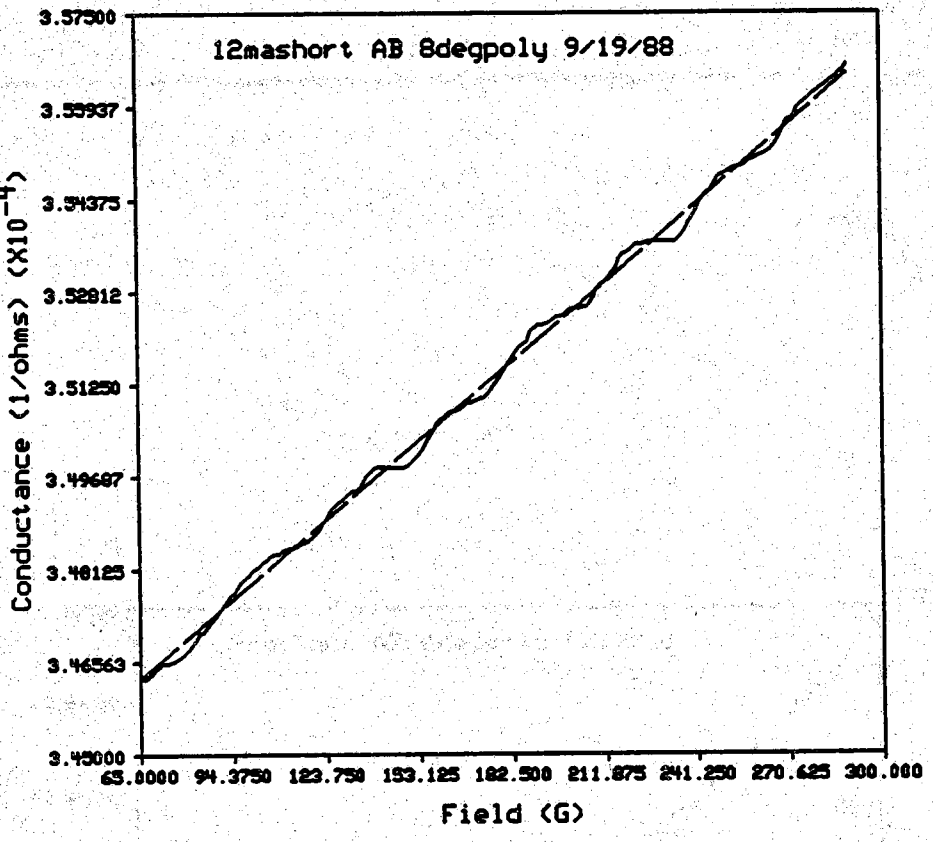

Figure 5.8. Aharanov Bohm oscillations with fitted polynomial.

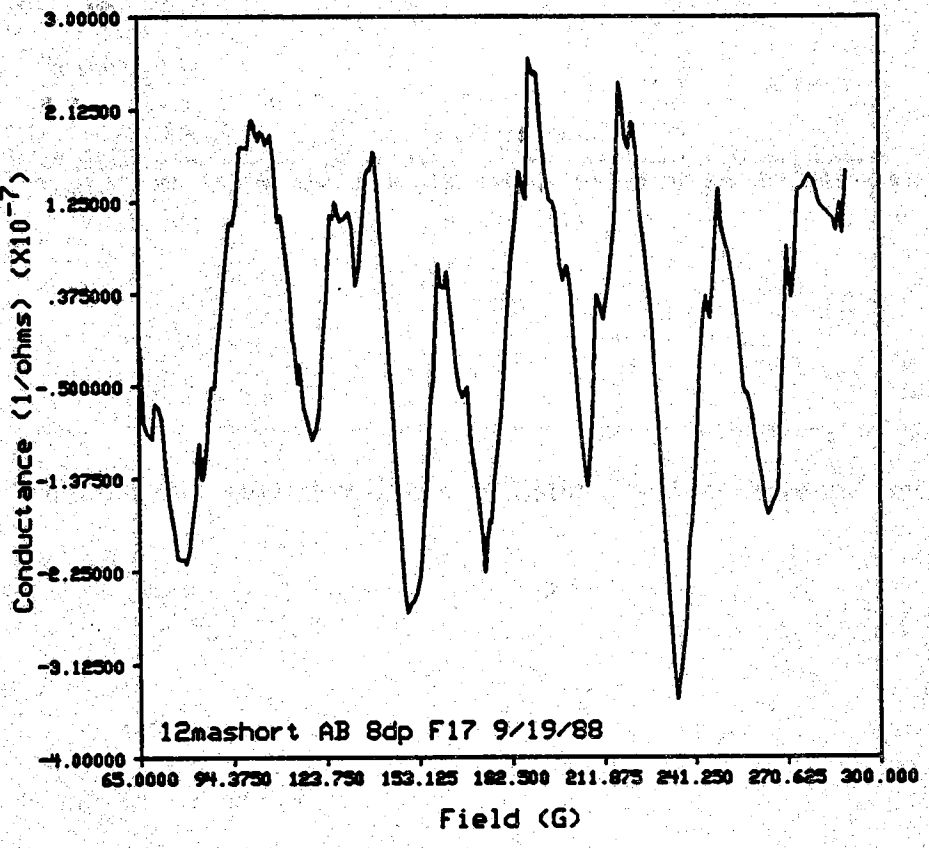

Figure 5.9. Aharanov Bohm oscillations with background removed.

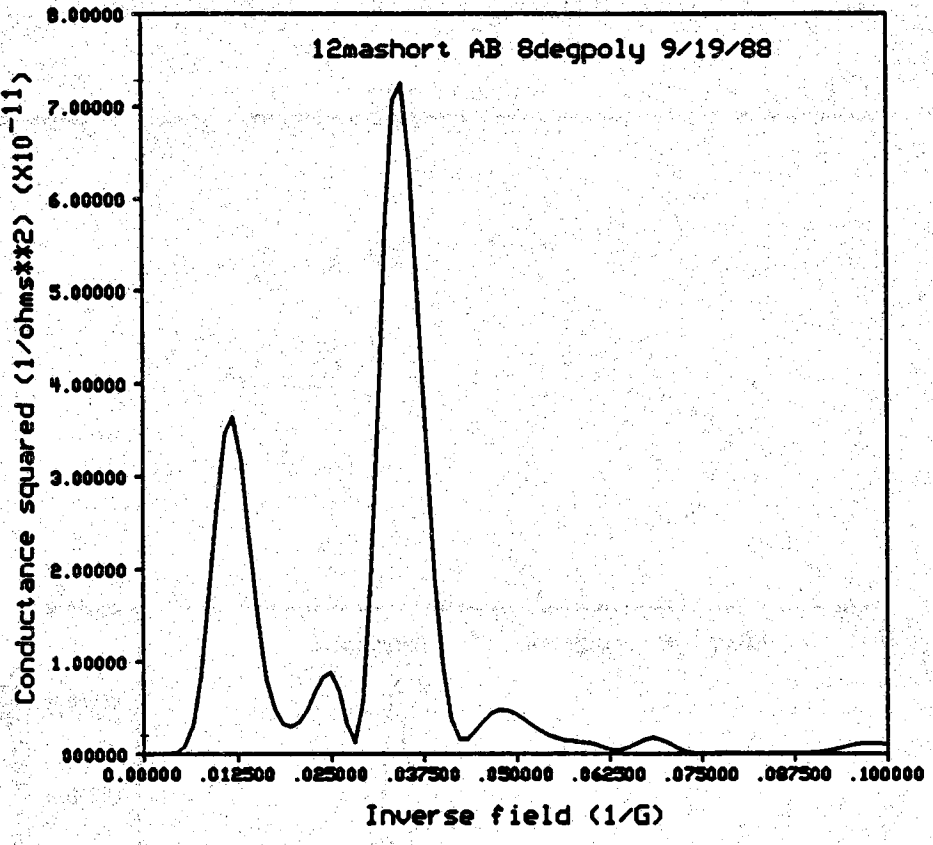

Figure 5.10. Fourier power transform of Aharanov Bohm oscillations

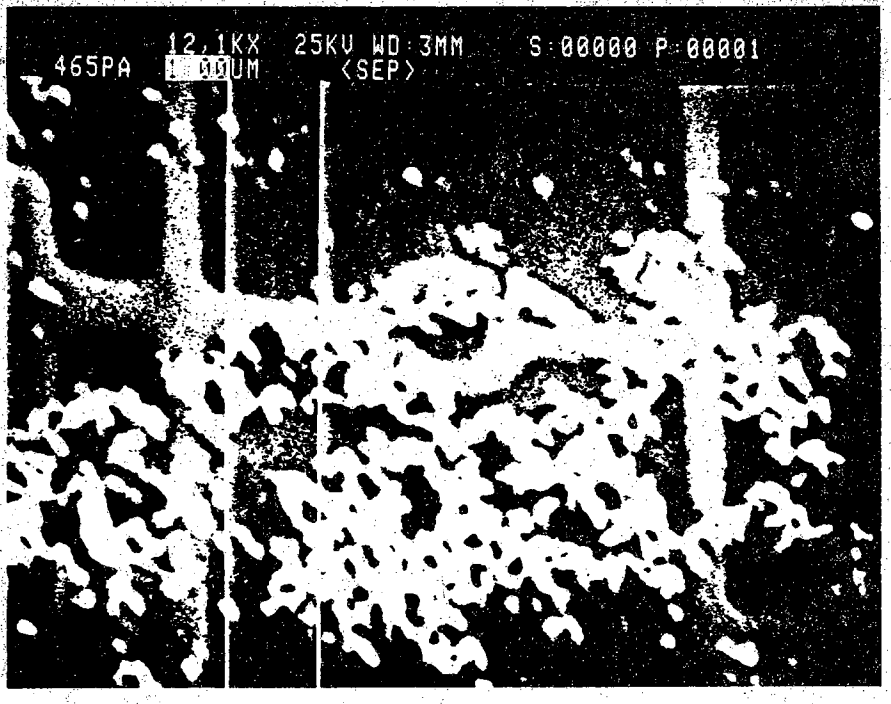

Figure 5.11. SEM micrograph of ring

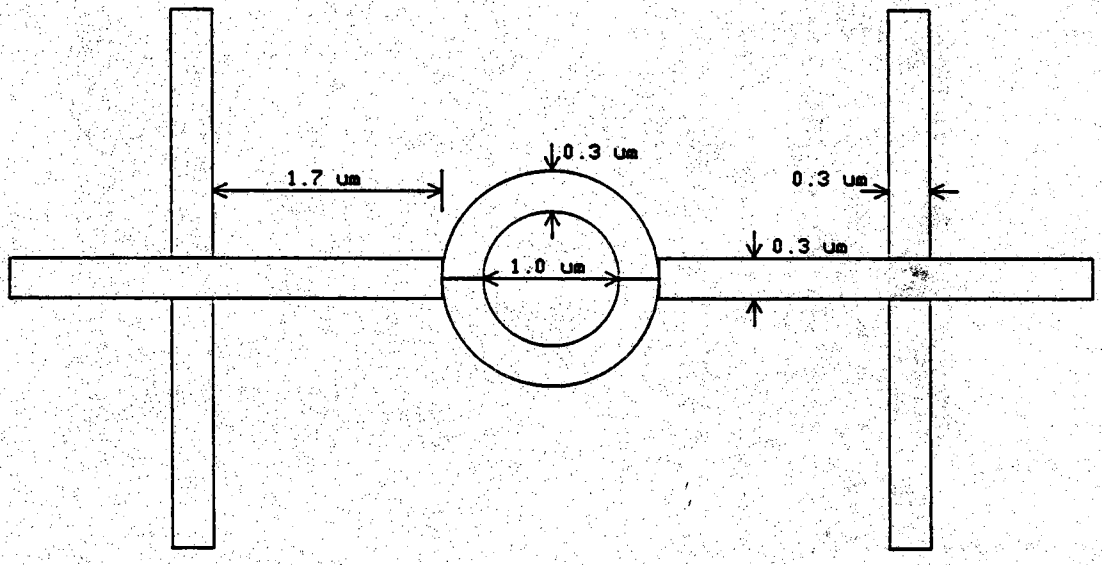

Figure 5.12. Nominal ring dimensions

The total resistance measured between two probes in figure 5.12 is the sum of the lead resistance, R_L, and the ring resistance, R_R. However, for Aharanov Bohm oscillations, the magnitude of the resistance fluctuations, ΔR, is due solely to ΔR_R. In formula form, $R = R_L + R_R$ and $\delta R = \delta R_R$. To get δG, write

$$G = \frac{1}{R_L + R_R}$$

and

$$\delta G = \frac{-1}{(R_L + R_R)^2}\, \delta R_R$$

Depending on the resistance of the leads, δG can be anything up to a maximum of $\delta R_R / R_R{}^2$. This is the quantity of interest and will be referred to as δG_R. The quantity calculated from the raw data is δG. The relationship between δG and δG_R is $\delta G_R = \delta G(R^2/R_R{}^2)$. Regarding figure 5.12,

$$R = \frac{R_s}{W}\left(4 + \frac{\pi r}{2}\right)$$

and

$$R_R = \frac{R_s}{W}\left(\frac{\pi r}{2}\right)$$

Therefore, $R/R_R = 4.918$, and $\delta G_R = 0.0846\ e^2/h$. Using this value in equation 5.1 gives $L_\phi = 0.80 \mu m$.

The second estimate is based on the relative magnitude of the fundamental frequency and harmonics of the Fourier power spectrum. Regarding figure 5.10, the frequency and magnitude of the fundamental are 328 (1/T) and 7.28×10^{11} $(1/\Omega^2)$ respectively. At the expected position of the first harmonic, 656 (1/T), there is a distinct feature with magnitude 1.96×10^{-12} $(1/\Omega^2)$. From section 2.4, L_ϕ is calculated as $L_\phi = 2\pi r/\ln(7.28/0.196)$. Thus L_ϕ is estimated to be 1.13 μm.

The two estimates of 0.80 μm and 1.13 μm are in fair agreement giving an average value for L_ϕ of 0.96 μm.

5.6 A Comment on the Low Frequency Component of the Fourier Power Spectrum

A large low frequency peak in the power spectrum has been observed repeatedly by others [65]. Their findings are as follows. In high mobility GaAs-AlGaAs heterostructures, the low frequency conductance fluctuations are correlated as opposed to the aperiodic fluctuations seen in Si and metals. The fluctuations are thought to be due to the Aharanov Bohm effect assosciated with the magnetic flux penetrating the area of the wire.

CHAPTER VI
NOVEL QUANTUM DEVICES

6.1 Gated Ring Structures

Two different types of devices are fabricated and tested, gated ring structures and quantum resonators. No positive results have been obtained from the gated ring structures. The gates seem to increase the channel depletion giving rise to enhancement mode rings. In this state, not even magnetic Aharanov- Bohm oscillations have been observed. Good results have recently been obtained by others [66]. A gate potential was shown to consistently shift the phases of the periodic magnetic Aharanov-Bohm oscillations. Ramping the gate voltage without a magnetic field, produced aperiodic fluctuations as expected for diffusive transport.

6.2 Quantum Resonators

Good results have been observed from a quantum resonator structure similar to figure 2.5. The nominal dimensions are shown in figure 6.1. Figure 6.2 shows a plot of conductance versus gate voltage at 4.2K. The dashed line is a fitted eight degree polynomial. Figure 6.3 shows the fluctuations after the background polynomial has been removed. Figure 6.4 shows a Fourier power transform of the fluctuations. Two modes of operation are discussed in section 2.2. In the first mode, the channel under the gate is not depleted and the gate voltage changes the wavevector of the electron wavefunction under the gate which is analogous to changing the impedance at the end of a transmission line. In the second mode, the channel under the gate is depleted and the gate voltage changes the electrical length of the channel. The pinch off voltage is measured in a large 2D structure to be 0.38 V and in a small 1D structure to be 0.15 V at 4.2K. This implies that all of the data shown corresponds to the second mode of operation in which the channel under the gate is depleted. No convincing results have been seen displaying the first mode of operation.

The decreasing conductance seen at the end of the voltage sweep is due to the depletion region approaching the vertical probe. By making two

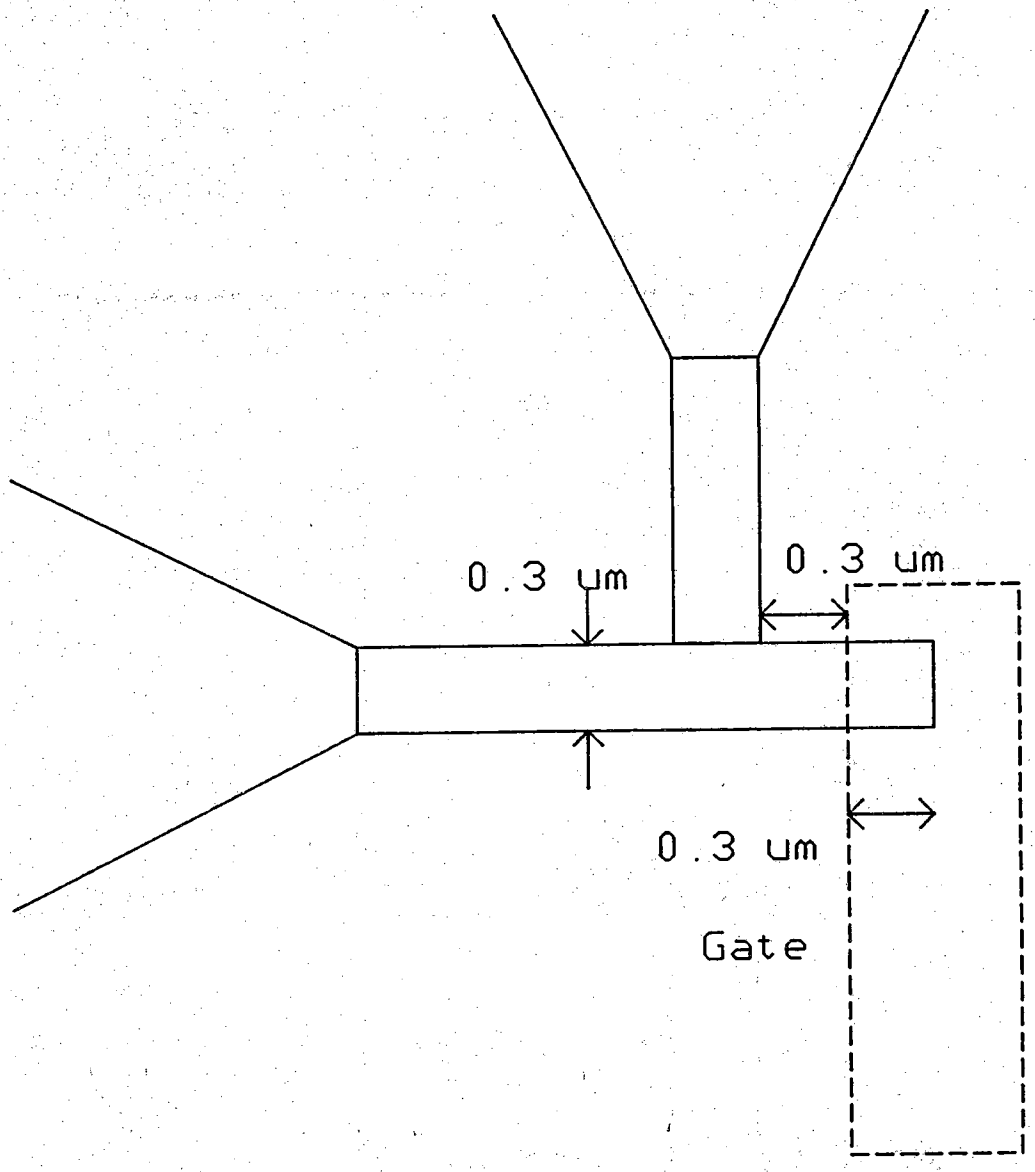

Figure 6.1. Quantum resonator device tested. Only submicron dimensions are drawn to scale.

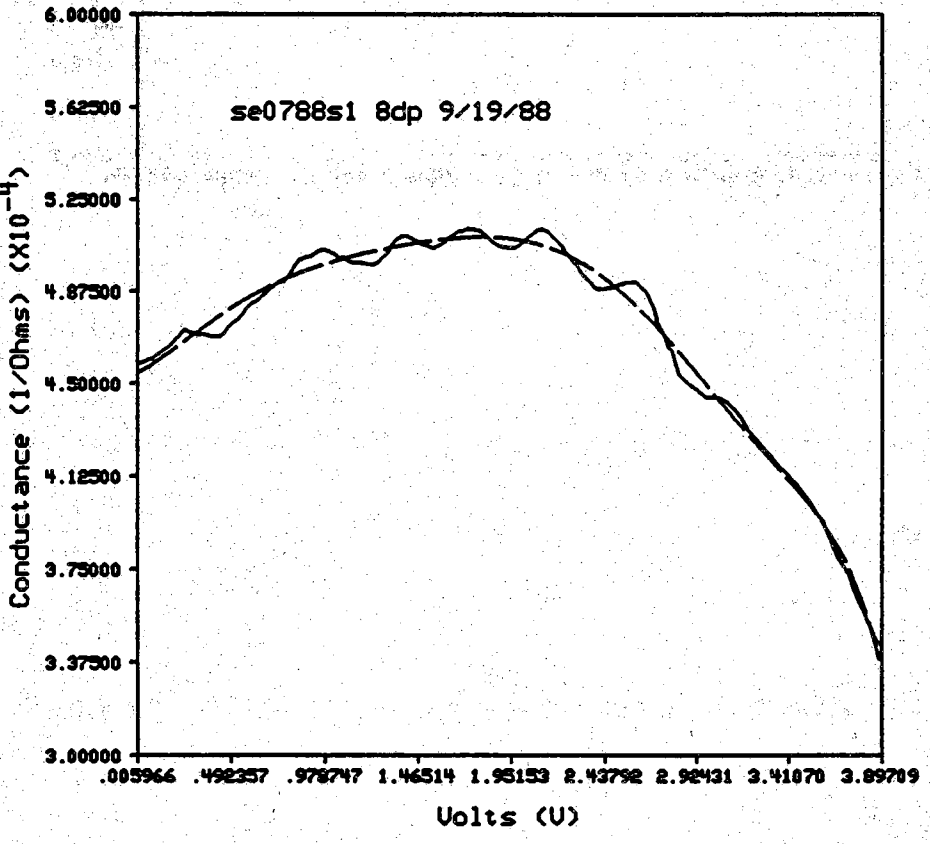

Figure 6.2. Conductance versus gate voltage. T = 4.2K.

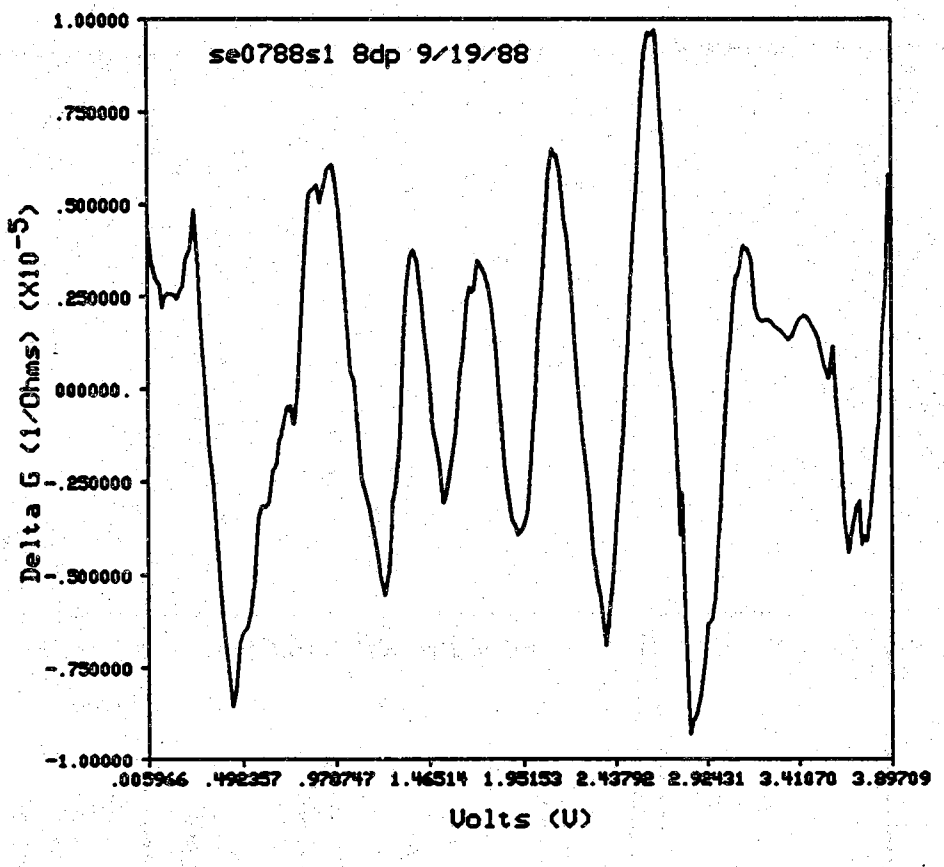

Figure 6.3. Conductance fluctuations with background removed

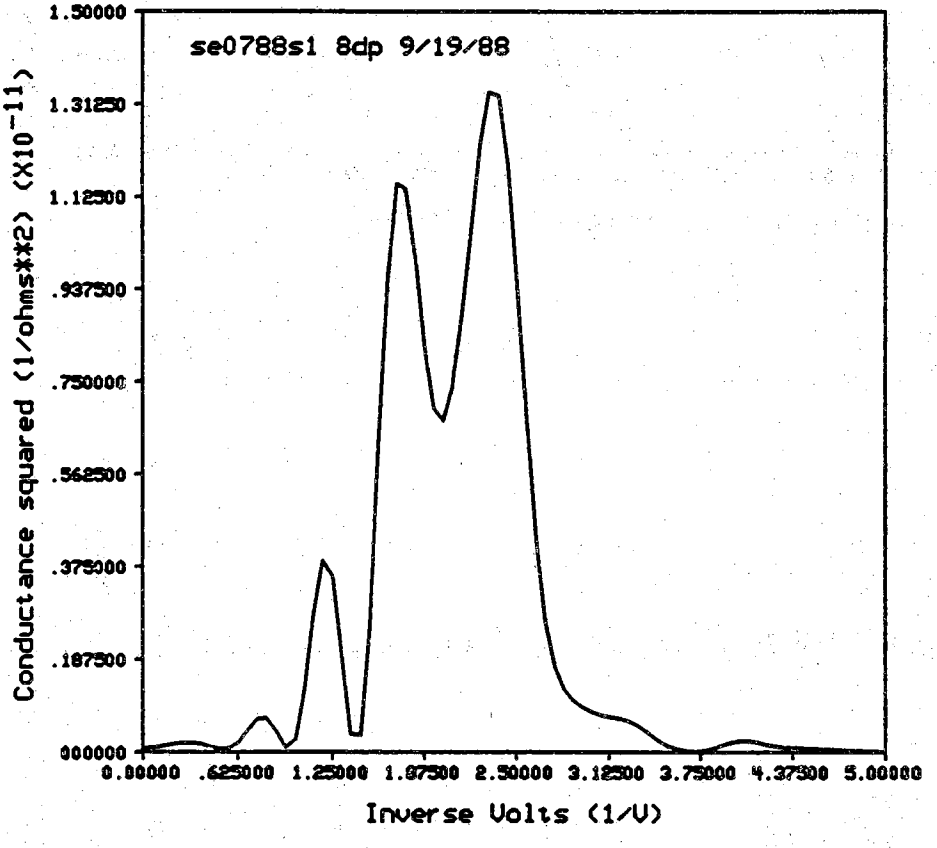

Figure 6.4. Fourier power spectrum of conductance fluctuations

assumptions, the gate voltage can be related to the channel length and the expected periodicity in voltage can be calculated. For details, see section 2.2.

For a single occupied transverse mode, the oscillations should be periodic (see figure 2.5) with the period, ΔV, given by $\Delta V = \lambda_f V_t/2d$. Here, V_t is $\sim$ 4 V, d is 0.3 μm, n_s is 2.6 x 10^{11} cm^{-2}, and, using the two dimensional density of states, λ_f is $\sim$ 50 nm. Using the ΔV from Fig. 6.5 and solving for λ_f gives the results shown in Table 6.1.

Table 6.1. Fermi wavelengths corresponding to Fourier spectrum

Peak	ΔV (V)	λ_f (nm)
1	.43	64
2	.59	88
3	.84	126

The values for λ_f are the correct order of magnitude (see Table 2.1). Since the cut-off voltage and the gate-probe spacing are not known precisely and the assumption of a linear relation between depletion width and voltage is questionable, the above analysis indicates only that the data is consistent with the theory described in section 2.2.

The dominant feature in the Fourier spectrum corresponds exactly to the average period of the five periodic looking fluctuations in the center of figure 6.3. The lower frequency structure is likely due to the non-periodic nature of the fluctuations near the beginning and end of the voltage sweep.

The rms magnitude of the oscillations is 0.10 e^2/h. At 4.2K, this value is large. In experiments investigating universal conductance fluctuations using a 1D Hall bridge with voltage probes spaced 0.7 μm apart, the magnitude of the fluctuation is almost imperceptible at 4.2K [11].

6.3 Summary

Results obtained from the quantum resonator are consistent with the theory based on the waveguide analogue presented in section 2.2. The conductance oscillations have a strong periodic component and their magnitude is relatively large.

CHAPTER VII
CONCLUSION AND FUTURE WORK

7.1 Summary

Two different types of devices are fabricated and tested, gated ring structures and quantum resonators. No positive results have been obtained from the gated ring structures. The gates seem to increase the channel depletion giving rise to enhancement mode rings. In this state, not even magnetic Aharanov- Bohm oscillations have been observed. Good results have recently been obtained In this thesis, the possibilities and problems of building electron analogues of microwave devices is discussed. Two novel quantum devices are descrbed and analyzed. A number of quantum mechanical magneto-resistance effects are described with an emphasis on using the phenomenon to characterize one dimensional wires, in particular to obtain the electrical linewidth and phase breaking length.

To fabricate quantum wires and devices the direct write capabilities of the Cambridge EBMF2 are developed. Lines of 0.1 μm are achieved in metal lift-off with PMMA and with the negative resist SAL 601-ER7. Electron beam direct write is described with an emphasis on the factors that effect resolution.

A full fabrication process for building quantum devices is developed. The conducting channels are defined by SAL 601-ER7 followed by a dilute wet etch. The gate level is defined by lift-off with PMMA. The entire mask layout and fabrication process is described in detail.

The intrinsic properties of carrier concentration and mobility for the two dimensional film are calculated from the classical Hall effect and Shubnikov-deHaas measurements on large Hall bridges. A magneto-resistance anomaly is noticed in the two dimensional film and discussed.

A ring structure is fabricated with an inner diameter of 1.0 μm and a linewidth of 0.3 μm. Magneto-resistance data are used to establish the electrical linewidth and phase breaking length at 1.3K. They are calculated to be 0.12 μm and 1.2 μm respectively.

Two different devices are fabricated and tested, a gated ring structure and a quantum resonator. No positive results are obtained here from the gated ring structure although positive results have recently been observed elsewhere. The results from the quantum resonator appear to be consistent with the theory. The conductance oscillations have a strong periodic component and their magnitude at 4.2K is large.

7.2 Directions for Future Work

The yield of the fabrication process can be improved. Presently, the yield is $\sim$ 50% for devices of simple geometry such as quantum resonators and considerably less for devices of more complex geometries such as Aharanov-Bohm rings. Resolution will probably be enhanced by diluting SAL 601-ER7 to give thinner resist. The thickness after spinning is now $\sim$ 1/2 μm. One tenth micron should be sufficient for a wet etch. Two to three tenths micron should be sufficient for a dry etch.

Dry etching should be explored in combination with an etch stop layer built into the film during MBE growth. Such a system would provide maximum uniformity of etch depth from wafer to wafer and across the wafer. The etch step is now the most difficult and uncontrolled part of the process.

Other methods for characterizing one dimensional wires should be considered. Recent split-gate experiments [68,69] indicate that it may be possible to directly observe the number of transverse modes in a wire by slowly pinching it off with a potential applied to a split gate on either side of the wire and counting the number of quantized conductance steps.

With the success of the gated ring experiment [66], work should proceed in fabricating a more elliptic ring structure thus increasing the ballistic nature of the transport thereby increasing the possibility of observing more periodic conductance oscillations due to the electrostatic Aharanov-Bohm effect.

Different geometries should be tested for the quantum resonator. The effect of different gate-probe spacings should be determined. The magnitude of the oscillations can be maximized by decreasing the number of transverse modes and decreasing the lead resistance.

REFERENCES

REFERENCES

1. G. Timp, A. M. Chang, J. E. Cunningham, T. Y. Chang, et. al. Phys. Rev. Lett., 58, 2814, (1987).

2. M. L. Roukes, A. Scherer, S. J. Allen, Jr., et. al. Phys. Rev. Lett., 59, 3011, (1987).

3. J. A. Simmons, D. C. Tsui, G. Weimann, Surface Science, 196, 70, (1988).

3. A. Scherer, M. L. Roukes, H. G. Craighead, et. al., Appl. Phys. Lett., 51, 2133, (1987).

4. 5. H. van Houten et. al., Appl. Phys. Lett., 49, 1781, (1986).

5. K. Ishibashi, Y. Takagaki, K. Gamo, S. Namba, Solid State Comm., 64, 573, (1987).

6. K. Ishibashi, K. Nagata, K. Gamo, et. al., Solid State Comm., 64, 573, (1987).

7. K. Ishibashi, K. Nagata, K. Gamo, et.al., Solid State Comm., 61, 385, (1987).

8. K. Owsu-Sekyere, A. M. Chang, T. Y. Chang, Appl. Phys. Lett., 52, 1246, (1988).

9. S. Thomas, I. McIntyre, S. P. Beaumont, et. al., J. Vac. Sci. Tech. B, 6, 127, (1988).

10. H. van Houten, B. J. van Wees, et. al., Appl. Phys. Lett., 49, 1781, (1986).

11. G. Timp, A. M. Chang, et. al., Phys. Rev. Lett., 59, 732, (1987).

12. S. Datta, M. R. Melloch, S. Bandyopadhyay, et. al., Phys. Rev. Lett., 55, 2344, (1985).

13. Y. Aharanov, D. Bohm, The Physical Review, 115, 485, (1959).

14. S. Washburn, R. Webb, Advances in Physics, 35, 375, (1986).

15. C. Ford, H. Ahmed, Microelectronic Engineering, 6, 169, (1987).

16. P. Mankiewich, R. Behringer, R. Howard, A. Chang, et. al., J. Vac. Sci. Tech. B, 6, 131, (1988).

17. S. Datta in *Physics of Quantum Electron Devices,* preprint.

18. S. Datta, M. Cahay, M. McLennan, Physical Review B, preprint.

19. S. Datta, SSDM, Tokyo, 1988, preprint.

20. S. Datta, Fourth International Conference on Superlattices Microstructures and Microdevices, 1988.

21. R. Webb, S. Washburn, C. Umbach, R. Laibowitz, Phys. Rev. Lett. 54, 2696, (1985).

22. *The Physics and Fabrication of Microstructures and Microdevices,* M. Kelly and C Weisbuch, eds., Springer Verlag, New York, 1986.

23. T. Thornton, M. Pepper, D. Andrews, G. Davies, Phys. Rev. Lett., 56, 1198, (1986).

24. H. van Houten, C. Beenakker, B. van Wees, j. Mooij, Surface Science, 196, 144, (1988).

25. P. Lee, T. Ramakrishnan, Reviews of Modern Physics, 57, 287, (1985).

26. K. K. Choi, D. C. Tsui, S. C. Palmateer, Phys. Rev. B, 33, 8216, (1986).

27. B. L. Al'tshuler, A. G. Aranov, JETP Lett., 33, 499, (1981).

28. K. K. Choi, D. C. Tsui, K. Alavi, Appl. Phys. Lett., 50, 110, (1987).

29. B. J. Lin, M. A. Paalanen, A. C. Gossard, D. C. Tsui, Phys. Rev. B, 29, 927, (1983).

30. K. K. Choi, D. C. Tsui, S. C. Palmateer, Phys. Rev. B, 32, 5540, (1985).

31. K. F. Berggren, T. J. Thornton, D. J. Newson, M. Pepper, Phys. Rev. Lett., 57, 1769, (1986).

32. P. A. Lee, A. D. Stone, H. Fukuyama, Phys. Rev. B, 35, 1039, (1987).

33. T. J. Thornton, M. Pepper, H. Ahmed, G. J. Davies, D. Andrews, Phys. Rev. B, 36, 4514, (1987).

34. W. J. Skocpol, P. M. Mankiewich, R. E. Howard, et. al., Phys. Rev. Lett., 56, 2865, (1986).

35. S. B. Kaplan, A. C. Warren, Phys. Rev. B, 34, 1346, (1986).

36. H. Z. Aheng, K. K. Choi, D. C. Tsui, G. Wiemann, Phys. Rev. Lett., 55, 1144, (1985).

37. K. F. Berggren, G. Roos, H. van Houten, Phys. Rev. B, 37, 10118, (1988).

38. *Electron Beam Technology in Microelectronic Fabrication,* G. R. Brewer, ed., Academic Press, N.Y., 1980.

39. *Microcircuit Engineering,* H. Ahmed, W. C. Nixon, eds., Cambridge University Press, N.Y., 1980.

40. M. P. Lepselter and W. T. Lynch in *VLSI Electronics and Microstructure Science,* V. 1, Norman Einspruch, ed., Academic Press, N.Y., 1981, p. 98.

41. *VLSI Microstructure Science,* V. 5, Norman Einspruch, ed., N.Y., 1982.

42. J. Vac. Sci. Tech. B, 1, Oct/Dec 1983.

43. J. Vac. Sci. Tech. B, 3, Jan/Feb 1985.

44. J. Vac. Sci. Tech. B, 4, Jan/Feb 1986.

45. J. Vac. Sci. Tech. B, 5, Jan/Feb 1987.

46. J. Vac. Sci. Tech. B, 6, Jan/Feb 1988.

47. Electron Beam Microfabricator Technical Manual, Cambridge Instruments, Ltd., 1982.

48. Operating Instructions for the EBMF-6 Microfabricator, Cambridge Instruments, Ltd., 1983.

49. S. Mackie and S. P. Beaumont, Solid State Technology, 35, 117, (1985).

50. L. D. Jackel, R. E. Howard, E. L. Hu, D. M. Tenant, P. Grabbe, Appl. Phys. Lett., 39, 268, (1981).

51. R. E. Howard, E. L. Hu, L. D. Jackel, P. Grabbe, D. M. Tenant, Appl. Phys. Lett., 36, 592, (1980).

52. J. I. Goldstein in *Introduction to Analytical Electron Microscopy,* Plenum Press, New york, 1979, p. 83.

53. D. F. Kyser, J. Vac. Sci. Tech. B, 1, 1391, (1983).

54. H. Seiler in *Electron Beam Interactions with Solids for Microscopy, Microanalysis, and Microlithography,* Scanning Electron Microscopy, Inc., Illinois, 1984, p. 33.

55. L. D. Jackel, R. E. Mankiewich, H. G. Craighead, R. W. Epworth, Appl. Phys. Lett., 45, 698, (1984).

56. T. O. Sedgwick, A. N. Broers, B. J. Agule, J. Electrochem. Soc.: Solid State Sci. and Tech., 119, 1769, (1972).

57. A. N. Broers, J. Electrochem. Soc.: Solid State Sci. and Tech., 128, 166, (1981).

58. R. E. Howard, H. G. Craighead, L. D. Jackel, P. M. Mankiewich, J. Vac. Sci. Tech. B, 1, 1378, (1983).

59. I. Haller, M. Hatzakis, R. Srinivasan, IBM J. Res. Dev., 12, 251, (1968).

60. H. Lui, M. deGrandpre, W. E. Freely, J. Vac. Sci. Tech. B, 6, 379, (1988).

61. *Microposit SAL 600 E-Beam Process,* Shipley information brochure, p. 4.

62. Private Communication, G. Bernstein.

63. J. N. Randall, M. A. Reed, T. M. Moore, R. J. Matyi, J. W. Lee, J. Vac. Sci. Tech. B, 6, 1383, (1988).

64. Private Communication, M. Young.

65. G. Timp, A. M. Chang, P. de Vegvar, R. E. Howard, R. Behringer, J. E. Cunningham, P. Mankiewich, Surface Science, 196, 68, (1988).

66. P. de Vegvar, G. Timp, P. M. Mankiewich, R. Behringer, J. Cunningham, Preprint.

67. W. Zawadzki, Semiconductor Sci. Tech., 2, 553, (1987).

68. D. A. Wharam, T. J. Thornton, R. Newbury, M. Pepper, et. al., J. Phys. C: Solid State Phys., 21, L209, (1988).

69. D. A. Wharam, M. Pepper, H. Ahmed, et. al., J. Phys. C: Solid State Phys., 21, L887, (1988).

70. A. M. Chang, G. Timp, T. Y. Chang, J. E. Cunningham, et. al., Surface Science, 196, 46, (1988).

71. *DIP User Specification,* Cambridge Instruments, Ltd., England, (1982).

72. S. W. Kirchoeffer, H. S. Newman, J. Comas, Appl. Phys. Lett., 46, 855, (1985).

73. *QSYS User Specification,* Cambridge Instruments, Ltd., Cambridge, England, (1982).

APPENDICES

Appendix A

Gated Microstructure Runsheet

Film Cross Section

50 Å n+ GaAs
600 Å n+ $Al_{.3}GA_{.7}As$
200 Å undoped $Al_{.3}Ga_{.7}As$
1.0 um undoped GaAs
$\sim$ 625 μm semi-insulating GaAs substrate

_____Solder film to back side of (100) Si wafer.
_____Clean
_____Ace
_____TCE
_____Meth
_____DI
_____N_2 dry

LEVEL 1: OHMIC CONTACTS AND ALIGNMENT MARKS

_____Hardbake @ 120° C for 15 min.
Time _____ Temp _____
_____Deposit AZ 1350J-SF positive resist
Spin @ 4400 rpm for 40 seconds
rpm _____ time _____
_____Inspect resist for coverage and holes.
_____Softbake resist for 10 min. @ 70° C
_____Align and expose Mask #1 (Ohmic Contacts)
Mask aligner: (Kasper 1:1)
Exposure time: 2 min. 14 sec.

Actual exposure time_____

_____Aid liftoff with Xylenes soak (3 minutes)

_____Develop resist

Develop in AZ Developer diluted 1:1 with DI (30 seconds)

Rinse in DI (40 seconds)

_____Inspect wafer

OHMIC CONTACT EVAPORATION

_____Remove native oxide in (1 NH_4OH : 40 DI) solution for 30 seconds

DI rinse.

N_2 dry.

_____Evaporate NiAuGe in Varian e-beam evaporator

50 Å Ni : 1500 Å Ge : 3000 Å Au : 850 Å Ni

Pressure: (4 X 10^{-7} torr)

Lift-off

_____Ace soak: 30 minutes; use squirt bottle to finish

_____Rinse in TCA to remove MUNG.

Methanol rinse

DI rinse

N_2 dry

_____Inspect wafer

_____Alloy contacts in Marshal oven

5 minute anneal @ 450° C

_____Inspect wafer

LEVEL 2: DIRECT WRITE MESA

_____Hardbake @ 120° C for 20 min.

Temp _____ Time _____

_____Deposit SAL 601-ER7

Spin @ 6000 rpm for 40 seconds

rpm _____ Time _____

_____Inspect resist for coverage and holes.

_____Bake resist for 30 min. @ 85° C

Time _____ Temp _____

_____Direct write level 2

_____Post exposure bake 4 min. 30 sec. at 105° C

Place directly on thermally stabilised petri dish

_____Develop resist

Develop in Microposit SAL 660 or SAL 661
Develop time: (10 min.)
Rinse in DI
Rinse time: (5 min.)
N_2 dry

_____Inspect wafer

MESA ETCH

_____Etch with a solution of 1 H_2O_2 : 3 NH_4OH : 1000 H_2O
(etch rate of ~ 430 Å/90 s)
Probe for isolation after each 5 second etch interval
Etch time _____
DI rinse
N_2 dry

_____Inspect wafer

LEVEL 3: DIRECT WRITE SCHOTTKY GATES

_____Hardbake @ 120° C for 20 min.
Temp _____ Time _____

_____Deposit 4% 950K PMMA
Spin @ 5000 rpm for 30 seconds
rpm _____ Time _____

_____Inspect resist for coverage and holes.

_____Hardbake resist for 4 hours @ 160° C
Time _____ Temp _____

_____Direct write level 3

_____Develop resist
Develop in Cellosolve:Methanol 3:7
Develop time: (5-10 seconds)
Rinse in Methanol
Rinse time: (30 seconds)

_____Inspect wafer

_____Remove native oxide in (1 NH_4OH : 40 DI) solution for 30 seconds
DI rinse.
N_2 dry.

_____Evaporate 200 Å Ti ; 800 Å Au

_____Soak in acetone 30 min. Use squirt bottle to finish lift-off.

_____Inspect wafer

_____Dice for testing

Mount in black wax on 2 inch Si wafer
Spin AZ1350 at ~3500 rpm fo 40s
Bake at 70° C for 10 min.
Saw to a depth of 1/2 wafer thickness
Remove AZ1350 in acetone
Remove from Si
Clean off wax in TCA
Cleave along cuts

_____Mount on circuit board with Abelbond

_____Bond

_____Test

Appendix B

Preparing a Graphics File For the Cambridge EBMF

After creating a graphics file, the file must be patterned using the pattern command on ECN. The syntax is

pattern -B -s2.8 -l3 filename > filenamel3.spd

The B switch will always be set. The number after -l is the level number on the graphics file. Filename is the name of the graphics file. The ASCII output will be placed in the file filenamel3.spd. The output file must end in .spd. The number after -s is the scalefactor and must be calculated. It is the ratio of pixels to microns.

One way to choose the scalefactor is the following algorithm.

1) $x = \dfrac{2^{15}}{\text{largest die dimension} \leqq 3 \text{ mm in } \mu\text{m}}$
2) Round down x to the nearest integer.
3) The scalefactor equals x.

For future reference, the field size will be needed for QSYS. If the above algorithm is used, the field size is 2^{15} / scalefactor. By changing the field size and the scale factor with respect to each other magnification or miniaturization of the pattern in the graphics file can be achieved. This is especially useful when building sub-micron devices since the smallest grid provided in the graphics packages is one micron. This method of miniaturization is used in the present work. All patterns are drawn ten times larger than desired. The die size is 1100 μm. The scalefactor is 2.8 and the field size is $2^{15}/28$ or 1170 μm. Notice that the die size is less than the field size, thus there will be field-to-field overlap, but it is irrelevant since nothing is written in the overlapping section of the field.

The file that will be created from the pattern command is referred to as the spd file. The spd file is a readable ASCII file containing the coordinates in pixels of points defining the geometric patterns. The file must be edited by adding a device line as the first line. The device line consists of the word DEVICE in capital letters, left justified, followed by a space, and at least one character.

The coordinates representing rectangles are easy to recognize and easy to check. A rectangle is represented by four numbers separated by spaces on a single line. The first two numbers are the (x,y) coordinates of the upper left hand corner and the second two numbers are the coordinates of the bottom right hand corner. For more information, see the Cambridge Instruments documentation [71]. For quick test runs, rectangular features can be written directly into an spd file. This is an easy way to generate single pass lines (a line defined by one scan of the beam) to test the limits of resolution of the equipment. A single pass line is a rectangle of zero width or zero height.

For sub-one-half-micron work, the INVERT command can improve thin vertical features. During exposure, the beam scans horizontally by default, so a thin vertical line would be written by many short horizontal scans. The scan direction can be inverted with the INVERT command, but the coordinates of the vertical line must first be found in the spd file. Since ultra-small features must be on a separate level due to the higher dose required because of the intra-feature proximity effect, often the vertical lines can be easily found and moved to the end of the file with an INVERT statement placed before them.

The spd file must now be transferred down to the PDP-11 that drives the Cambridge EBMF2. The easiest method is to log on to one of the terminals connected directly to the PDP-11. The operating system is RSX-11M. For a good introduction to RSX-11M that provides clear simple descriptions and examples of the basic commands needed to use the system, see reference 50. After logging on, set the default for the disc and directory where the files are to be stored. Then use Kermit to transfer the spd files from the ECN account to the PDP-11.

The use of Kermit is somewhat tricky. It is easy to freeze up the terminal. The syntax for using Kermit is as follows. The RSX-11 prompt is ">" and the UNIX prompt is "$". These prompts will precede the commands to remind the reader where the commands are taking place.

> K11

One is now connected to the eg machine on ECN. The usual prompts of

Login:

Password:

will appear. Login and move to the directory where the spd file is stored. Type

$ kermit -s filenamel3.spd

where filenamel3.spd is the name of the spd file. After the carriage return

there will be no prompt. Type
^gc
where "^g" means to hold the control key down while typing "g" (but not for the "c"). The following prompt will appear.
kermit -11>
Respond with "receive". The file transfer begins. A message will appear when the transfer is complete. After the transfer, return to ECN. Log off the ECN account. Return to the PDP-11 and stop kermit. The command sequence is as follows.

```
kermit -11> con          ;return to ECN
$ ^d                     ;log off
Login: ^gc               ;return to PDP
kermit -11> ^z           ;stop kermit
>                        ;back in RSX-11
```

The spd file now exists in the PDP-11 directory under the same name as on ECN. Next, the spd file must be compiled into the binary file used by QSYS. The command is
> dip filename13=filename13/SY:10/ER
The binary output file is automatically named filename13.bpd. The SY:10 is explained in reference 51. It need not be changed. The ER erodes 1/2 pixel from the border of each pattern. It should be left off if the spd file has been coded by hand. For example, without ER, a zero height rectangle on the spd file will become a single pass line with a height of one pixel. With ER, it will be nothing. The data is now ready to be used by QSYS.

Appendix C

Coordinate Systems

Three different coordinate systems are used: one for the graphics file (BRUTUS or CMASK), one for the spd file and one for the QSYS job file. They are related as follows.

The graphics coordinate system is a right hand system with the origin in the bottom left hand corner and all lengths in units of microns. The spd file coordinate system is a left hand coordinate system with the origin in the upper left hand corner and lengths in units of pixels. The coordinate system used in the QSYS job file is the same as that of the spd file except units of length are in millimeters. An example is in order illustrated in figure C.1.

Start with a square die of 1100 μm x 1100 μm with an alignment mark centered at (x,y) = (100, 100). On the graphics file it would appear as in figure C.1(a). Assume that the scalefactor in the pattern command is 28 (28 pixels/μm). Then the coordinates in the spd file will become as in figure C.1(b). Finally, in the QSYS job file, when the position of the alignment mark must be specified, the coordinate system is as in figure C.1(c).

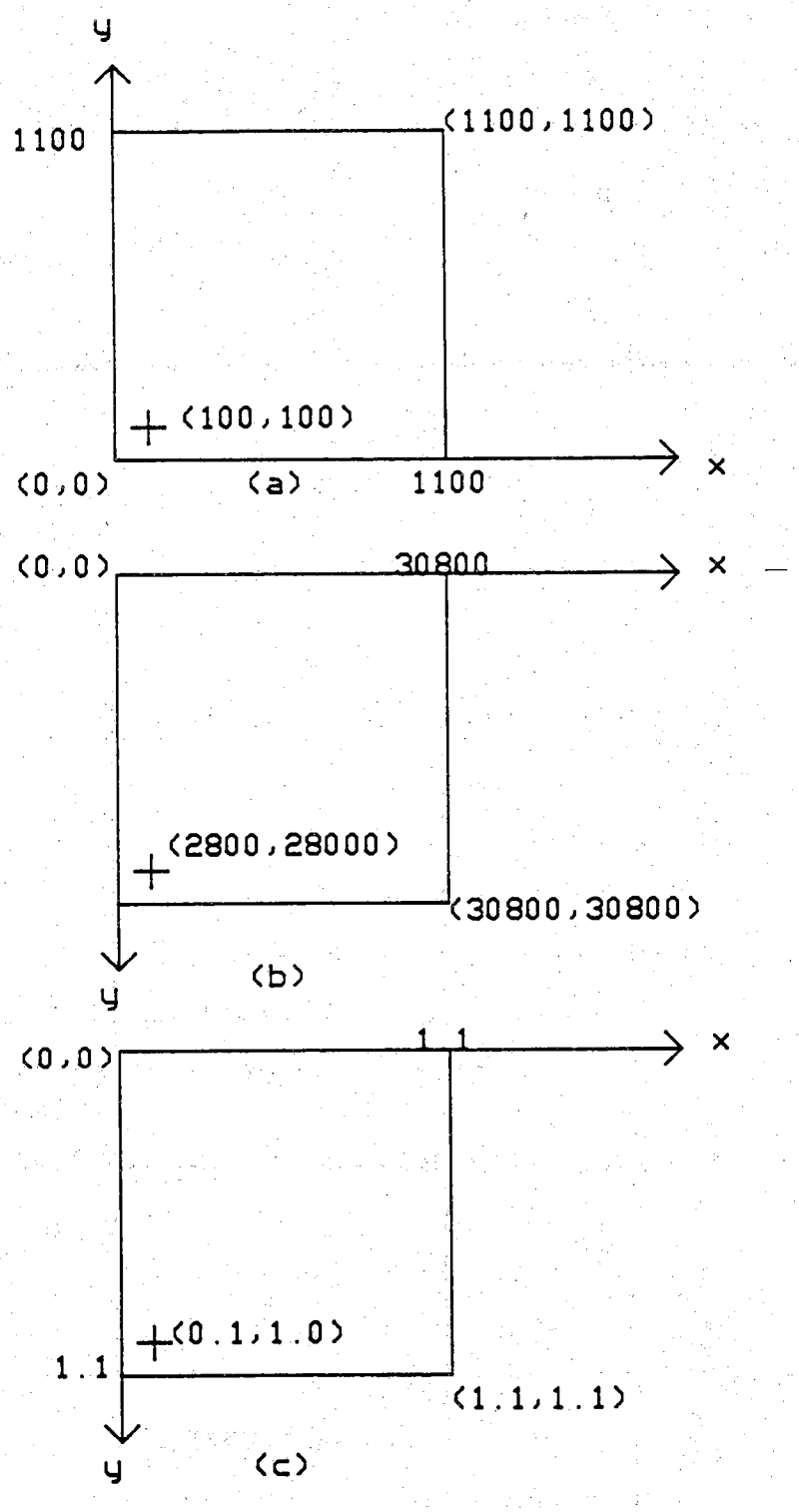

Figure C1. Coordinate systems: (a) Graphics (b) SPD (c) QSYS

Appendix D

The Cambridge EBMF Job Control Language

QSYS is the job control language of the Cambridge EBMF. For complete documentation, see [73]. QSYS commands may be entered from the keyboard or downloaded from RSX-11M. Most aspects of the writing session, such as mark detection, alignment, and clockspeed are controlled by QSYS commands. The following program, developed by M. Young, is used for all direct writing where level-to-level alignment is needed. In its present form, the program writes a matrix of 4 x 4 square die 1.1 mm on an edge. The program is easily modified for different die and array sizes.

```
;M. YOUNG  7MAR88
;
;
; INITIAL SETUP...
;
ABS
FLD 1.1702857
;
; SET FOR 100X MAG...
;
KEY 1
FOF
MOV 40 40
JOY
;
; FIND UPPER LEFT CORNER OF CHIP, AND
; MARK FOR INITIAL FSZ...
;
KEY 1
; SET LEVELS FOR FSZ...
;
KEY 1
SPO FM
FSZ 2 FM
@JB:16DECMRK
@DL:CALPIT
MOV FM
LOC 4 P1 O1
; FIRST OF THREE POINTS FOR
; MAP WAF
;
; NOW DRIVE OVER TO THE NEXT
; WAF MARK, TO THE RIGHT...
JOY
KEY 1
SPO P2
LOC 4 E2 O2
; NOW, DRIVE DOWN TO THE LAST
```

```
; WAF MARK...
JOY
KEY 1
LOC 4 E3 O3
SPO E1 .1 .1
SPO E2 4.5 .1
SPO E3 4.5 3.4
; LAST CHANCE TO CHANGE E1,E2,E3...
; ALSO TURN OFF AUTO LEVEL
KEY 5
;
SPO WO O1
FLD 1.1702857
MAP WAF WO
FLD 1.1702857
MOV WO
FSZ 2 WO
FSZ 4 WO
; NOW COMES THE REPETITIVE STUFF...
MOV 0 0
@JB:7MARROW
MVR 3.3 0 0 1.1
@JB:7MARROW
MVR 3.3 0 0 1.1
@JB:7MARROW
;MVR 3.3 0 0 1.1
;@JB:7MARROW


; 7MARROW.JOB M. YOUNG
;
; ON ENTRY, POSITIONED ON FIRST MARK
; OF FIRST DIE IN THE ROW.
;
@JB:7MARCHI2
@JB:7MAREXP2
; STILL IN CHI MODE...
MOV 0 0
```

```
WAF
MVR 0 0 1.1 0
@JB:7MARCHI2
@JB:7MAREXP2
; STILL IN CHI MODE...
MOV 0 0
WAF
MVR 0 0 1.1 0
@JB:7MARCHI2
@JB:7MAREXP2
MOV 0 0
WAF
MVR 0 0 1.1 0
@JB:7MARCHI2
@JB:7MAREXP2
MOV 0 0
WAF
;END OF ROW.....


;7marchi.job  7-march-88 MPY
;7marchi.job  7-march-88 RKL
;
LOC 4 E1 O1
SPO CO O1
MAP CHI CO
MEX -.08 -.1
LOR 4 E1 O1 .08 .1
; NOW WE COMPLETE THE MEASUREMENTS
; USING ;LOR 2'S, THEN AGAIN USING
; ;LOR 4'S...
;LOR 2 E2 P2 1.0 .1
;LOR 2 E2 O2 1.0 .1
;LOR 2 E3 O3 1 1
;LOR 2 E4 O4 .1 1
;FSZ 1 CO
; NOW FIELD ROTATION IS NEARLY
; RIGHT... TRY LOR 4'S...
```

```
;
LOR 4 E1 O1 .08 .1
LOR 4 E2 O2 .98 .1
LOR 4 E3 O3 .98 1.005
LOR 4 E4 O4 .1 1
FSZ 1 CO
;
SPO P1
;MOV FC
;JOY
;KEY 1
;MOV P1
LOR 4 E1 O1 .08 .1
MSH E1 O1
; END OF JOB, READY TO EXPOSE


;7MAREXP.JOB
;SET CLOCK SPEED L2
KEY 1
CLK 3 13.1E5
;
;CHOOSE YOUR HALL BRIDGE OR RING
;TYPE
;%PD:-----#L2
KEY 1
;%PD:-----#L3
KEY 1
```